THESIS FOR THE DEGREE OF DOCTOR OF PHILOSOPHY

Controlling Flow with Light:

Bubble Induced Particle Transport Around Plasmonic and Dielectric Nanostructures

Pantea Dara

Department of Physics

CHALMERS UNIVERSITY OF TECHNOLOGY

Gothenburg, Sweden 2025

Controlling Flow with Light: Bubble Induced Particle Transport Around Plasmonic and Dielectric Nanostructure

Pantea Dara

ISBN 978-91-8103-180-5

Doktorsavhandlingar vid Chalmers tekniska högskola.

Ny serie 5638

ISSN 0346-718X

Division of Nano- and Biophysics

Department of Physics

Chalmers University of Technology

SE-412 96 Gothenburg

Sweden

Cover:

Finite Element (FEM) simulation of the flow and temperature fields around a pair of asymmetric a-Si nanodisk arrays with edge-to-edge distance of 400 nm while heated by a 532 nm wavelength Gaussian incident beam with beam waist radius of $13\ \mu m$*. The left and right arrays consist of 37, and 19 nanodisks respectively, and a bubble with a radius of* $0.85\ \mu m$ *is considered on top of the larger array.*

Printed in Sweden by

Chalmers digital printing

Chalmers Tekniska Högskola

Gothenburg, Sweden, 2025

CHALMERS UNIVERSITY OF TECHNOLOGY
Department of Physics

Controlling Flow with Light:

Bubble Induced Particle Transport Around Plasmonic and Dielectric Nanostructures

Pantea Dara

Abstract

When cooking, we observe how suspended herbs move with convection streams from the heated bottom to the cooler surface of boiling water. Similarly, flows develop around vapor bubbles generated by optical heating of plasmonic or dielectric nanostructures. These nanostructures strongly absorb light at wavelengths near their surface plasmon or Mie resonance, making them effective nanoscale heat sources that locally increase the temperature of the surrounding fluid. Localized heating induces vapor bubbles that drive Marangoni flow, a fluid motion caused by surface tension gradients. The spatial temperature variation along the bubble's interface initiates convective bulk flows, as fluid is driven from warmer (lower-tension) regions to cooler (higher-tension) regions, with compensatory flow in the surrounding fluid. Since the induced surface stress depends on the spatial temperature gradient and not on the value of the temperature, this effect can be very strong even for small changes in temperature if the length scale is small enough, making it a favorable mechanism in micro and nanoscale. We demonstrate that the Marangoni flow direction can be controlled by adjusting temperature gradients across the bubble surface. This control is achieved by altering the position of the laser focus, by breaking photothermal symmetry with asymmetric nanoparticle arrays, or by tuning the light the polarization. These Marangoni flows enable rapid microparticle transport over significant distances, particularly near boundaries where traditional flow methods struggle with mass transport due to the no-slip condition. Our findings are supported by vectorial flow measurements based on optical force microscopy and video velocimetry, along with flow profile simulations using finite element methods and Stokeslet approximations. Additionally, the bubble lifetime and dynamics were studied with darkfield microscopy. The results underscore the potential of precision light-driven particle manipulation in microscale fluidic applications.

List of publications

I. Directional control of transient flows generated by thermoplasmonic bubble nucleation.

Pantea Dara, Mohammad Mahdi Shanei, Steven Jones, and Mikael Käll

Journal of Physical Chemistry C 127.35 (2023): 17454-17459.

My contribution: Performed all experiments and data analysis, designed, and simulated ellipsoidal plasmonic structure, modeled and simulated the flow profiles, and wrote the first draft of the manuscript.

II. Bubble Dynamics and Directional Marangoni Flow Induced by Laser Heating of Amorphous Silicon Nanodisk Arrays.

Pantea Dara, and Mikael Käll

Journal of Physical Chemistry C (2025), in review

My contribution: Performed all experiments and data analysis, designed and simulated amorphous silicon structures, simulated the flow profiles, and wrote the first draft of the manuscript.

Acknowledgments

To my beloved parents and my incredible brother, whom I miss terribly, you are my best friends, my guides, my shoulder to lean on, and simply the best. My gratitude to you is beyond words. Thank you for your unwavering support.

Mikael, I sincerely appreciate your patience with me. I have learned so much from you, not only as a researcher but also in many other aspects of life. Without a doubt, listening to your talks and learning new concepts and methods from you were some of my favourite parts of my PhD. Thank you for giving me the opportunity to grow and improve, both personally and scientifically.

Steve, I truly could not have done this without you. You were an incredible teacher and mentor. Even after four years, I still find myself learning from your thesis. I feel incredibly lucky to have met you and Dasha, you are two of the kindest people I have ever known.

Angela, thank you for listening to me and supporting me during one of the most challenging times of my PhD. You were more than a mentor to me, and I am truly grateful to have had you by my side. Thank you for all your support.

Adri, Emelie, Laura, and Betül, thank you for creating a safe space where I could share my frustrations and stories. Your friendship is one of the most precious things I have gained during my PhD. You are incredibly smart, tremendously supportive, and above all, exceptionally kind. Also, thank you for all the sweets, candies, and energy drinks that got me through writing my thesis!

Julie, Hana, and Caroline, I am grateful for your time, advice, and for sharing your experiences with me. It was always a pleasure to sit and talk with you.

Timur, I have learned so much just by observing your approach to research. Your passion for science has always been a great source of motivation for me.

Charlotte, thank you for all the support you have given me in every possible way. You are an extraordinary person, and the third-floor lab simply wouldn't function without you!

Kajsa, Julia, Mirna, Ariadna, Hana, and Rebeka, thank you for all the gossip, conversations, and support during our lunch breaks. You are amazing!

Michaela, Daniel, Oliver, Abhay, Khosro, Erik, Tom, Mindaugas, Santosh, Gosha, Oleg, Tomasz, Sasha, Vasilii, Mahdi, and Ximin, thank you for your positive energy and the fun discussions during lunch and fika. Each of you has made our corridor a better place in your own unique way!

Fredrik and Jan, I sincerely appreciate your time, advice, and support in my ISP meetings.

I would also like to thank the past and present members of the Chalmers Physics PhD council and FFF. Thank you for the engaging discussions, fun activities, and memorable meetings. I will truly miss the time I spent with you!

To my amazing and supportive friends, Roujin, Amir, Nima, Shahrzad, both Tinas, and Sarvin, life here would not have been the same without you. Your friendship means so much to me, and I hope you know how deeply I appreciate you. Thank you for all your help and for the unforgettable nights we spent together.

A heartfelt thank you to everyone in the Nano and Biophysics division, or rather, the entire physics department. I feel incredibly privileged to have had the chance to meet so many amazing people.

And finally, Mathias, thank you for listening to me talk about the same things over and over again until I felt better. It always feel better when I'm with you.

Pantea Dara

Göteborg, 19/02/2025

Table of Contents

Chapter I: Introduction

The ability to control fluid flow at the micro- and nanoscale is a fundamental challenge with profound implications for scientific and technological applications, including biomedical diagnostics, chemical sensing, and materials science. Among the diverse strategies explored for this purpose, light-induced manipulation of fluid flow around nanostructures offers remarkable precision and versatility. This emerging field, known as optofluidics, has seen significant advancements over recent decades [1-5]. This thesis investigates the mechanisms and applications of light-induced flow, focusing on bubble-mediated particle transport around plasmonic and dielectric nanostructures.

Thermoplasmonics and its applications

Thermoplasmonics involves the use of plasmonic nanostructures to convert light into heat, generating localized temperature gradients that drive various thermal processes, such as enhanced Brownian motion, thermoviscous effects, thermoosmosis, thermophoresis, convection, and phase changes [6-11]. Plasmonic materials like gold exhibit strong optical absorption at specific wavelengths due to localized surface plasmon resonances, making them highly efficient nanoscale heat sources. These sources can achieve significant temperature increases in their immediate vicinity through the Joule effect, enabling applications across diverse fields, including photothermal therapy [12-14], trapping, manipulation and deposition of flow and nanoobjects [15-21], biology [22-25], photochemistry [26, 27], and solar energy harvesting [28, 29].

Gold, the primary plasmonic material employed in this thesis for heat generation is, valued for its chemical stability and biocompatibility. The polarization and wavelength-dependent absorption cross-sections of gold nanostructures further enhance its versatility, enabling precise control over temperature gradients [30-32]. Moreover, the plasmon-enhanced enhanced light-matter interaction allows for rapid superheating and vaporization of surrounding water, leading to the formation of microscopic bubbles [33-35]. Since 2012, continuous-wave (CW) illumination studies of plasmonic microbubbles have attracted significant attention [36-38].

In 2014, Baffou et al. demonstrated that achieving temperatures exceeding 100°C is necessary for liquid vaporization and bubble nucleation on gold nanoparticle arrays under CW illumination [39]. The presence of vapor bubbles significantly reduces the thermal conductivity of the surrounding medium [40, 41], further intensifying the localized temperature rise. However, these high temperatures pose challenges, as prolonged exposure can cause gold nanostructures to deform or melt [42, 43], limiting their utility in the photothermal generation of vapor bubbles. To address these limitations, thermal management strategies, such as protective capping layers, can be employed to mitigate reshaping [44, 45]. However, these strategies add fabrication complexity, making alternative materials with higher thermal stability favorable for certain applications.

Dielectric nanostructures: an alternative approach

Dielectric materials, such as silicon, offer a robust alternative for optical heating. Their stability at elevated temperatures makes them suitable for photothermal vapor bubble generation and boiling studies. In 1991, Zapka et al. demonstrated explosive boiling on silicon substrates using short-pulsed lasers, resulting in the movement of submicron particles [46]. This work introduced the “steam laser cleaning” technique, highlighting its potential for nanoparticle manipulation [47]. Subsequent studies by Ohta et al. employed hydrogenated amorphous silicon (a-Si) layers for heat generation [48]. More recently, Zograf et al. demonstrated the efficacy of high-refractive-index dielectric nanoparticles as optical heaters, showcasing their higher melting thresholds and suitability for Raman Stokes thermometry due to their inherent Raman phonon scattering properties [49]. Raman thermometry based on measuring shifts in phonon frequency provides accurate temperature distributions around nanostructures [50-55]. Ongoing studies on thermophotonics in the past years [56-59] have led to numerous applications, including sensing and thermometry of protein molecules [60], controllable drug release in living cells [61], thermally reconfigurable metalens [62], trapping nanoparticles [63], solar energy harvesting [64], and optofluidic transport [65]. In this thesis, a-Si nanodisks were employed for heat generation, bubble nucleation, and particle manipulation in water. Both crystalline and amorphous silicon were used to investigate vaporization and bubble nucleation through Raman Stokes thermometry.

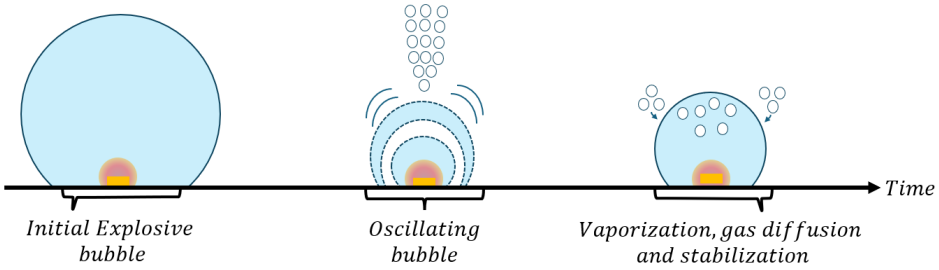

Figure 1.1 Typical phases of bubble growth in air-equilibrated water under CW illumination: explosive boiling, oscillation boiling, and vaporization-dominated and diffusion-driven growth.

Dynamics of vaporization and bubble nucleation

Vaporization and bubble nucleation at the nanoscale exhibit unique characteristics due to the confined temperature and pressure gradients. The dynamics of optically induced bubbles have been extensively studied, encompassing factors such as the size and shape of heating elements, substrate wettability, laser configurations (pulsed versus CW), water gas content, and the temporal evolution of bubbles. Early investigations, such as Eyring and coworkers' work in 1984, utilized pulsed lasers to generate microscopic bubbles at liquid-dielectric interfaces, enabling particle removal [66]. Inspired by Zapka's findings, Yavas et al. later explored the nucleation and growth dynamics of bubbles on chromium films, quantifying nucleation thresholds and growth velocities [67].

Since 2012, CW illumination studies on plasmonic microbubbles have gained prominence. In 2015, Liu et al. demonstrated that degassing water reduces bubble size, while hydrophilic nanoparticles promote larger, faster-growing bubbles [68]. Li et al. subsequently described the "oscillatory boiling" regime, characterized by a single oscillating bubble following the collapse of an initial explosive bubble [69]. Lohse et al. further identified distinct phases of bubble growth in air-equilibrated water: explosive boiling, oscillatory boiling, and diffusion-driven growth (Figure 1.1) [70-73]. The explosive boiling phase involves rapid vapor bubble expansion after a delay. This phase has been observed during the nucleation of vapor bubbles with sizes ranging from tens of nanometers to tens of micrometers [71, 74, 75]. The second phase, oscillation boiling, sees a self-oscillating bubble exhaling tiny air bubbles [69, 75-77]. The final phase involves bubble growth by direct vaporization and air diffusion [39, 70]. It has been shown that the main limiting factor in the rapid bubble shrinkage after the heat source is turned off is the air diffusion from the bubble to the bulk liquid [39, 73].

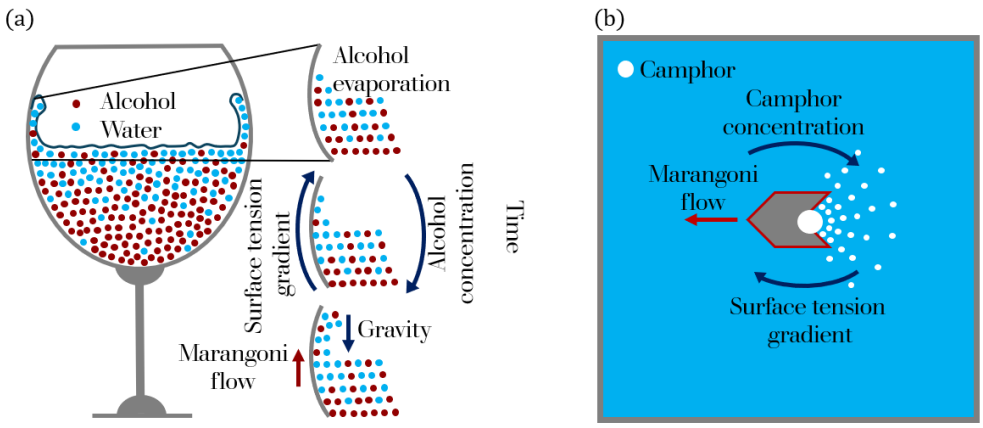

Figure 1.2 Classical examples of solutal Marangoni effect (a) Tears of wine form on a wine glass: Over time the alcohol in the wine evaporates from the surface at a rate higher than water, decreasing the concentration of alcohol in the meniscus. This creates a surface tension gradient that moves the meniscus up the walls of the glass, leading to the formation of a film on the glass surface that is even more depleted of alcohol, resulting in more wine getting pulled up. Finally, droplets will be formed, and the tears of wine will run down due to gravity. (b) Self-propelled camphor disk boat: This vintage toy boat is propelled by a difference in surface tension. As the camphor mixes with water at the stern of the boat, a gradient of surface tension is created, pushing the boat forward.

More recently, Jones et al. showed that using isolated nanostructures as heating elements can limit the diffusion-driven growth phase, resulting in ultra-fast bubble dynamics [44].

In this thesis, the life cycle of vapor microbubbles around isolated nanostructures was studied using darkfield scattering imaging. By focusing on isolated nanostructures, the influence of diffusion-driven growth was minimized, providing insights into rapid bubble dynamics and life cycle behavior.

Marangoni flow: a key mechanism in induced fluid motion

During growth, bubbles traverse layers with varying temperatures, generating surface tension gradients that induce Marangoni flow [78]. First described by Carlo Giuseppe Matteo Marangoni in 1865 [79], this phenomenon involves fluid motion along an interface caused by surface tension gradients [79, 80]. Classical examples include the "tears of wine" phenomenon, which was described by J. Thompson in 1855 [81], and self-propelled camphor disk boats [82], a vintage Japanese toy. In both cases, the spatial variation of a solute concentration (alcohol or camphor) will create a surface tension gradient at the liquid interface, resulting in a flow from the alcohol/camphor-rich area to the water-rich area (Figure 1.2) [83]. In addition to solute concentration gradients, temperature differences also drive Marangoni flow through the thermocapillary effect. Spatial temperature variations at liquid interfaces create unbalanced

surface stresses, resulting in fluid motion from regions of low surface tension (hot) to high surface tension (cold). To conserve volume, this interfacial flow induces bulk fluid motion, creating convective flow patterns [84]. An interesting example of this phenomenon is the snow globe effect, which is the movement of ice particles on a freezing soap bubble [85].

Since the induced surface stress depends on the spatial temperature gradient and not on the value of the temperature, this effect can be very strong even for small changes in temperature if the scale is small enough, making it a favorable mechanism to create flow at micro and nanoscales [84].

Although Marangoni effects were initially overlooked in boiling heat transfer due to the dominance of buoyancy-driven flows, McGrew et al.'s work in 1966 and subsequent experiments by Beer emphasized their importance in heat transfer and bubble dynamics [86, 87]. Ever since, light induced Marangoni flow has been the subject of many studies [69, 75, 77, 88-98].

Equally important from an application perspective is the ability to control the direction of the Marangoni flow. For the case of a single bubble nucleated on a heat source, as shown in Figure 1.3a, the flow along the bubble surface (indicated by green arrows) moves from the bottom (hot region) to the top (cold region). This surface flow is accompanied by two symmetrical vortices in the bulk liquid (gray arrows) and a substrate-induced flow directed toward the heat source (red arrows). The substrate flow at the water/glass interface is particularly significant because, due to the no-slip boundary condition, the velocity near the surface is typically very low.

One straightforward method to control the flow near the substrate is by manipulating the temperature gradient on the bubble surface. This can be achieved by introducing an additional heat source on one side of the primary heat source, thereby breaking the symmetry of the temperature profile. This modification creates an in-plane temperature gradient in addition to the out-of-plane gradient. The resulting flow shifts from the warmer side of the bubble toward the cooler side (e.g., from right to left, as illustrated in Figure 1.3b).

If the secondary heat source generates sufficient heat to vaporize the surrounding water, a second bubble will form. This introduces a more intricate flow pattern influenced by factors such as the size of the bubbles, the temperatures of the heat sources, and the relative positions

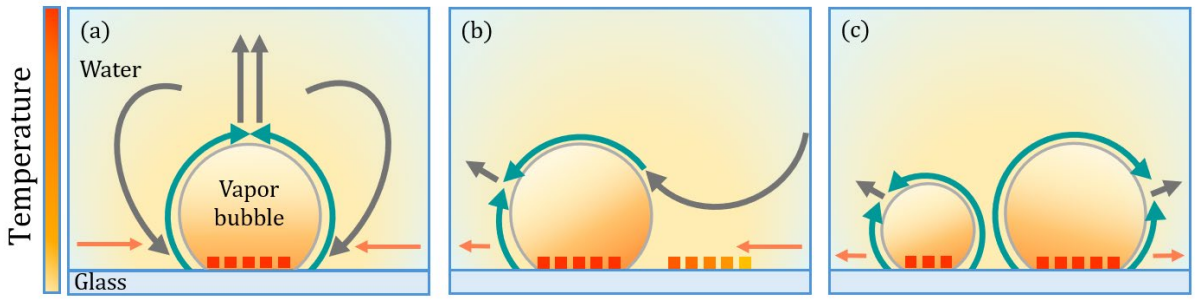

Figure 1.3 Expected Marangoni flow induced by: a) a single bubble with a temperature gradient normal to the interface, b) a single bubble with temperature gradients both perpendicular and parallel to the surface, and c) by two unequal nearby bubbles with an additional temperature gradient parallel to the surface.

of the bubbles. An example of such a configuration is depicted in Figure 1.3c, demonstrating the complex and dynamic flow behaviors that can emerge under these conditions.

Recent studies have demonstrated light-induced Marangoni flows with controllable flow direction achieved through temperature gradients. For instance, Ohta et al. reported directional control of flow via gradients on air bubble surfaces [48, 99]. Similarly, the Namura group demonstrated Marangoni flows around photothermal microbubbles, achieving directional control through in-plane temperature gradients [100, 101].

Another interesting subject to study is the correlation between the flow and bubble dynamics. Recently, Jones et al. showed that strong transient flows are induced near plasmonic nanodisk array as microbubbles form, and that this transient is followed by a weaker but sustained Marangoni flow [45].

In this thesis, we investigated the potential to control induced flows around microbubbles using light. Spatial control of flow was achieved by adjusting laser polarization or position. Additionally, the correlation between bubble life cycles and flow dynamics was examined, providing new insights into the interplay between optical heating, bubble behavior, and induced fluid motion.

Research objectives and methods

This thesis aims to investigate the mechanisms of light-induced fluid flow around plasmonic and dielectric nanostructures and to develop methods for controlling these flows for practical applications. The research involves a combination of experimental measurements and numerical simulations to understand the dynamics of vapor bubble generation, Marangoni

flows, and particle transport. Techniques such as optical force microscopy, video velocimetry, and Raman Stokes thermometry are employed to characterize the flow and temperature fields.

Structure of the thesis

The thesis is organized as follows:

Chapter II: **Optothermal Heating**

The scattering and absorption of light by nanostructures, and the consequent temperature increase, are highly dependent on the shape and composition of the structures and the polarization and the wavelength of the incident light. To understand these dependencies and how structures can generate heat by absorption of light, we must first understand how light interacts with matter. This chapter discusses the principles of scattering and absorption of light by nanostructures, focusing on both metallic and dielectric materials, and the mechanisms of heat generation. The discussion provides the foundation for understanding thermal effects in subsequent chapters.

Chapter III: **Optically Induced Bubbles**

Vapor bubble nucleation, a phenomenon often observed in macroscopic boiling, exhibits unique and complex dynamics at the microscale. This chapter investigates the mechanisms of boiling and bubble nucleation under optical heating, emphasizing explosive, oscillatory, and Leidenfrost boiling regimes. It further examines the behavior of vapor bubbles, including their growth, collapse, and motion.

Chapter IV: **Optofluidics**

As the central mechanism for fluid motion and mass transport in this thesis, the Marangoni effect is examined in detail. This chapter examines the principles of Marangoni flow, including surface tension, and the Navier-Stokes equation.

Chapter V: **Methods**

This chapter describes the research methods used for vapor bubble generation and detection, flow characterization, and thermometry including a brief review on optical tweezers and Raman thermometry, as well as the simulation methods.

Chapter VI:

Chapter VI provides a summary of the appended papers.

Chapter VII:

The final chapter concludes the thesis with a summary of findings and an outlook on future research directions.

Chapter II: Optothermal Heating

"Known phenomena seemed to indicate that a mere variation in the size of gold particles gave rise to a variety of resultant colours. I have not confirmed that result yet, still those I have obtained seem to me to present a useful experimental entrance into certain physical investigations respecting the nature and action of a ray of light. I do not pretend that they are of great value in their present state, but they are very suggestive, and they may save much trouble to any experimentalists inclined to pursue and extend this line of investigation"

- Michael Faraday

In his celebrated 1857 Bakerian Lecture, Michael Faraday shared his fascination with the interplay between light and gold particles suspended in water. Unlike bulk gold, which appears yellow and reflective, these nanoscale particles exhibited brilliant hues tha t varied with size. [102]. Faraday's experiments hinted at the interplay between light and nanopaerticles—a relationship far richer and more intricate than understood at the time. This interplay is also behind the stunning colours of stained-glass windows in medieval cathedrals. Artisans of the Middle Ages, unaware of the nanoscale interaction at work, manipulated the colours of glass by incorporating small amounts of metal nanoparticles, such as gold or silver (Figure 2.1). The physical phenomenon Faraday hesitated to fully interpret in 1857 has since blossomed into what is now recognized as the field of plasmonics [103].

This field explores how metallic nanoparticles interact with light through the excitation of collective electron oscillations, or surface plasmons, on their surfaces. The interplay of light with these small particles gives rise to phenomena like enhanced scattering, and absorption which Faraday had unknowingly stumbled upon during his experiments.

The understanding of light-matter interactions was significantly advanced in the early 20th century with Gustav Mie's seminal work. Mie's 1908 paper provided the first theoretical framework for describing the scattering and absorption of light by spherical particles [104].

Figure 2.1 The stained glass in Strasbourg Cathedral (photographed by Pantea Dara).

His theory, now known as Mie theory, extended beyond simple approximations and accurately described the optical properties of both metallic and dielectric particles.

In this chapter we will discuss the interaction of light with nanostructures and how this interaction can result in heat generation. First, we will discuss the light-matter interaction, then we will study the special case of subwavelength structures, and finally we discuss how heat can be induced by light.

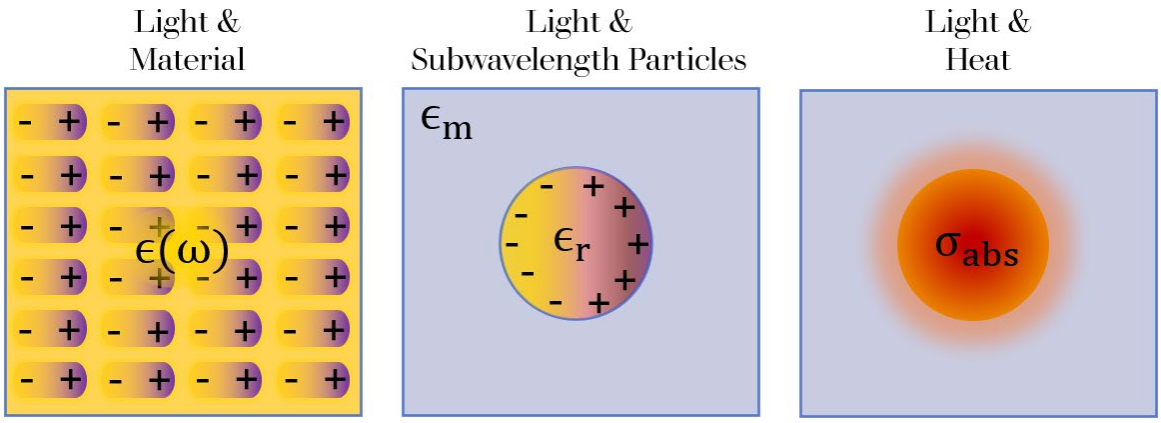

Figure 2.2 Outline of chapter II.

2.1. Light-matter interaction

The interaction of light with particles results in two key phenomena: scattering and absorption. Scattering occurs when matter redirects the incident light into different directions, and absorption occurs when the energy of the incident light is retained within the particle. Both phenomena are quantified through cross-sections: the scattering cross section (σ_{sca}) and absorption cross section (σ_{abs}). These cross-sections are a measure of the probability of light being scattered or absorbed. The total extinction of light is the sum of scattering and absorption, and the dominance of either process depends on the material properties and size of the particle [105]. To understand these dependencies and how micro and nano structures can generate heat by absorption of light, we must first understand how light interacts with matter. In this chapter, we will discuss the simple case of elastic scattering[1] (such as Rayleigh scattering or Mie scattering) and absorption of light, where nonlinear optical effects are not considered. So, we will consider a nonmagnetic[2], linear[3], isotropic[4], and homogenous[5] medium in all cases.

2.1.1 Optical properties of materials

Light is an electromagnetic wave, described by two oscillating vector fields as function of position and time: the electric field $\mathbf{E}(\mathbf{r}, t)$ and magnetic field $\mathbf{H}(\mathbf{r}, t)$. In the applications discussed in this thesis, the light-matter interaction is primarily governed by the electric field. We thus consider a plane electric wave propagating through space, given by:

$$\mathbf{E}(\mathbf{r}, t) = \mathbf{E_0} e^{i(\mathbf{k}\cdot\mathbf{r}-\omega t)}, \qquad 2\text{-}1$$

where $\mathbf{r}$ is the position vector, ω is the angular frequency ($\omega = 2\pi f$), f is the frequency of light, and $\mathbf{k}$ is the wavevector with magnitude, wavenumber, $k = |\mathbf{k}| = 2\pi/\lambda$, with λ being the wavelength of light. The phase velocity of light in a medium is denoted by c, and in a vacuum, it is given by $c_0 \approx 3 \times 10^8$ m/s. The wavelength and the frequency of light in vacuum are related to one another by the dispersion relation [106]:

$$\lambda_0 = c_0/f. \qquad 2\text{-}2$$

[1] In elastic scattering the energy or equivalently, the frequency of the scattered light remains the same as that of the incident light.
[2] A medium is considered nonmagnetic if its magnetic permeability (μ_r) is approximately equal to the permeability of free space (μ_0), meaning it does not significantly respond to magnetic fields.
[3] A material is linear if its interaction with light is not affected by the intensity of the incident light.
[4] An isotropic materials exhibit the same optical properties in all directions.
[5] A medium is homogeneous if its material properties are uniform throughout space.

Light, in the conventional sense, refers to the portion of the electromagnetic spectrum visible to the human eye, typically ranging from λ_0 between 400 nm to 700 nm, also known as optical wavelengths. The phase velocity and wavelength of light in a medium relate to their vacuum counterparts by the dimensionless scaling factor n', which is commonly referred to as the refractive index [106, 107]:

$$c = c_0/n', \quad 2\text{-}3$$

$$\lambda_m = \lambda_0/n'. \quad 2\text{-}4$$

Therefore, the dispersion relation in a material will change to $\lambda_m = c/f$. However, in absorbing materials the refractive index is complex, and consists of a real part, which is the scaling factor we have already mentioned, and an imaginary part which is known as the attenuation coefficient and describes absorptive losses within the medium. Throughout this thesis, we denote the complex refractive index of the medium as N, the real part as n', and the imaginary part as n'' ($N = n' + n''i$). Before discussing how scattering and absorption cross-sections relate to n' and n'', we introduce the concept of permittivity.

When an incident electric field $\mathbf{E}$ interacts with matter, it displaces the charged particles in the material, effectively distorting both the material and the electric field. This response is described by the displacement field [106]:

$$\mathbf{D} = \epsilon_0\mathbf{E} + \mathbf{P}, \quad 2\text{-}5$$

where ϵ_0 is the permittivity of free space, and $\mathbf{P}$ is the macroscopic polarization density. $\mathbf{P}$ is the total induced polarization in the material, accounting for the contribution of all the charged particles (e.g. bound and free electrons), and it is related to $\mathbf{E}$ by [106]:

$$\mathbf{P} = \epsilon_0\chi\mathbf{E}, \quad 2\text{-}6$$

where χ is called the electric susceptibility. Substituting 2-6 in 2-5 yields:

$$\mathbf{D} = \epsilon_0\mathbf{E} + \epsilon_0\chi\mathbf{E} = \epsilon_0(1+\chi)\mathbf{E} = \epsilon_0\epsilon_r\mathbf{E} = \epsilon\mathbf{E}, \quad 2\text{-}7$$

where $\epsilon_r = 1 + \chi$ is the relative permittivity, and $\epsilon = \epsilon_0\epsilon_r$, is the absolute permittivity of the material. In simple words one can say that **permittivity** quantifies how much a material **permits** the formation of electric fields within it (that's where the word permittivity originated from). A higher ϵ indicates a stronger light-mater interaction.

The simplest and yet physically accurate model for describing permittivity is the Lorentz model, which characterizes the optical response of bound charges in dielectrics [108]. Based on this model, each bound electron behaves as a classical harmonic oscillator, with a natural frequency ω_0, around a fixed positively charged ion. The equation of motion for each of these electrons under the influence of an external electric field **E** is [109]:

$$\ddot{\boldsymbol{x}}(t) + \Gamma\dot{\boldsymbol{x}}(t) + \omega_0^2\,\boldsymbol{x}(t) = -\frac{e}{m_e}\mathbf{E}(t)\,, \tag{2-8}$$

where $\boldsymbol{x}$ is the displacement, m_e is the electron mass, $-e$ is its charge, and Γ is the damping frequency. Taking the Fourier transform in terms of angular frequency ω, and solving the Eq. 2-8 for $\boldsymbol{x}(\omega)$, we obtain:

$$\boldsymbol{x}(\omega) = \frac{-\frac{e}{m_e}}{\omega_0^2 - \omega^2 - \mathrm{i}\Gamma\omega}\,\mathbf{E}(\omega). \tag{2-9}$$

Each displaced electron contributes an induced dipole moment $\mathrm{p} = -ex$ to the total macroscopic polarization of the matter. Therefore, for a material with a density of electrons (ρ) macroscopic polarization can be described as:

$$\mathbf{P} = -\rho e\boldsymbol{x}(\omega) = \frac{\rho\frac{e^2}{m_e}}{\omega_0^2 - \omega^2 - \mathrm{i}\Gamma\omega}\mathbf{E}(\omega)\,. \tag{2-10}$$

Comparing Eq. 2-10 to 2-6, the electric susceptibility becomes:

$$\chi(\omega) = \frac{\frac{\rho e^2}{\epsilon_0 m_e}}{\omega_0^2 - \omega^2 - \mathrm{i}\Gamma\omega}\,. \tag{2-11}$$

Finally, the Lorentz relative permittivity can be defined as:

$$\epsilon_{\mathrm{Lorentz}}(\omega) = 1 + \chi(\omega) = 1 + \frac{\omega_\mathrm{p}^2}{\omega_0^2 - \omega^2 - \mathrm{i}\Gamma\omega}, \tag{2-12}$$

where $\omega_\mathrm{p} = \sqrt{\rho e^2/\epsilon_0 m_e}$ is the plasma frequency. The Lorentz model derived so far assumes a single resonance frequency. However, real materials exhibit multiple electronic resonances

due to different atomic energy levels of bound electrons. To account for this, we introduce the oscillator strength f_j for each resonance, leading to the generalized Lorentz permittivity. The oscillator strength ensures that the sum of all contributions correctly represents the total response of the material, and it is often determined experimentally by fitting to measured permittivity data. Even at high frequencies, where explicit resonances are absent, the material exhibits a residual response due to core electrons and other effects. This is accounted for by introducing the background permittivity ϵ_∞, which shifts the entire permittivity function upwards. Physically, this term represents the contribution of tightly bound electrons that respond at frequencies far beyond the electromagnetic spectrum region we are interested in.

Considering the contribution of multiple electronic resonances and the background permittivity, the total Lorentz relative permittivity is expressed as [109]:

$$\epsilon_{\text{Lorentz}} = \epsilon_\infty + \sum_{j=1} \frac{f_j \omega_{pj}^2}{\omega_{0j}^2 - \omega^2 - i\Gamma_j \omega}, \qquad 2\text{-}13$$

where ω_{pj} is the plasma frequency, ω_{0j} is the resonance frequency, and Γ_j is the damping factor associated with the jth resonance.

In metals and conductive materials, free electrons contribute significantly to the relative permittivity. Unlike bound electrons, these electrons do not experience a restoring force ($\omega_0 = 0$), leading to the Drude model. In the Drude model, the conduction band electrons are considered as an ideal gas of independent particles that move freely between scattering events,

$$\epsilon_{\text{Drude}} = \epsilon_\infty - \frac{\omega_p^2}{\omega^2 + i\Gamma\omega}. \qquad 2\text{-}14$$

In this case ω_p is the plasma frequency of free electrons, and $\Gamma = 1/\tau$ where τ is the relaxation time of the free electron gas.

The final expression for the permittivity in a material that has both bound and free electrons is:

$$\epsilon_{\text{Drude-Lorentz}} = \epsilon_\infty + \sum_{j=1} \frac{f_j \omega_{pj}^2}{\omega_{0j}^2 - \omega^2 - i\Gamma_j \omega} - \frac{\omega_p^2}{\omega^2 + i\Gamma\omega}, \qquad 2\text{-}15$$

which is known as the Drude-Lorentz model. In many cases when the Drude-Lorentz model is used for describing the relative permittivity of metals, instead of calculating the plasma frequency of different contributing electrons separately, only the plasma frequency of free

electrons is calculated. In this case the effect of different density of charges is accounted in the oscillator strength f_j, and the Drude-Lorentz model will be written in the form of:

$$\epsilon_{\text{Drude-Lorentz}} = \epsilon_\infty + \sum_{j=0} \frac{f_j \omega_p^2}{\omega_{0j}^2 - \omega^2 - i\Gamma_j \omega} \quad , \qquad 2\text{-}16$$

where j=0 represents the Drude model and free electrons with $\omega_{00} = 0$. In simulations done in this thesis, the Drude-Lorentz model was used in the form of Eq. 2-16. The relative permittivity is a complex number and varies with the frequency of light, ω, meaning that it is dispersive.

The complex refractive index we mentioned earlier is related to the relative permittivity of the material as [109]:

$$\sqrt{\epsilon_r} = N = n' + in''. \qquad 2\text{-}17$$

Now, if we denote the real and imaginary parts of the relative permittivity as $\epsilon_r{}'$ and $\epsilon_r{}''$, then n and k can be written as the function of $\epsilon_r{}'$ and $\epsilon_r{}''$, and vice versa:

$$n' = \sqrt{\frac{\sqrt{\epsilon_r{}'^2 + \epsilon_r{}''^2} + \epsilon_r{}'}{2}}, \quad \epsilon_r{}' = n'^2 - n''^2, \qquad 2\text{-}18$$

$$n'' = \sqrt{\frac{\sqrt{\epsilon_r{}'^2 + \epsilon_r{}''^2} - \epsilon_r{}'}{2}}, \quad \epsilon_r'' = 2n'n''. \qquad 2\text{-}19$$

At optical frequencies, and in some dielectrics, the imaginary part of the relative permittivity is negligible ($\epsilon_r{}'' \approx 0$) resulting in a negligible absorption. Moreover, the real part of the relative permittivity is constant. On the other hand, metals have a strongly frequency-dependent permittivity with negative real and non-zero imaginary parts. Figure 2.3 shows the real and imaginary parts of the relative permittivity for gold from the Drude-Lorentz model (model parameters are obtained from ref. [110]) compared to the one experimentally measured by Johnsson and Christy [111].

Now that we have realized how relative permittivity defines the optical response of materials, we have the tools to define the scattering and absorption cross section of subwavelength particles.

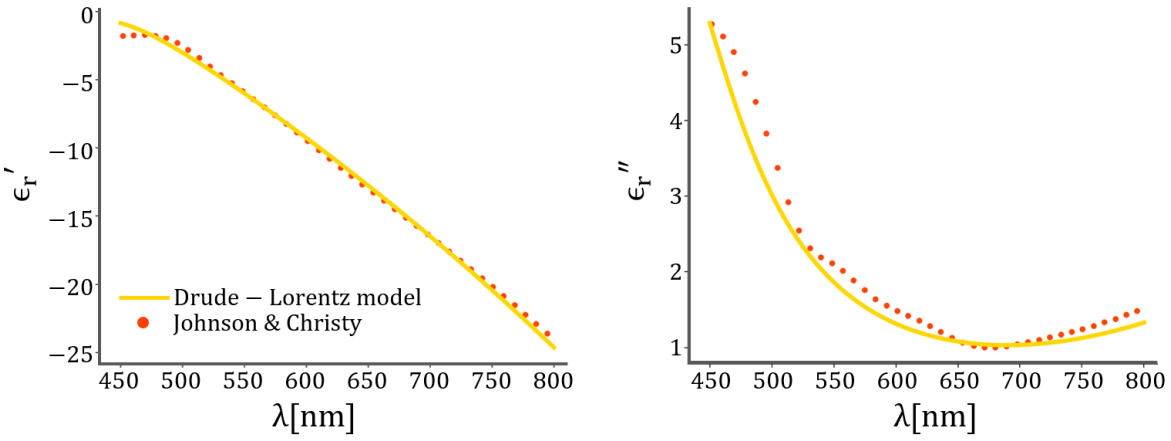

Figure 2.3 Real (left) and imaginary (right) parts of the relative permittivity of gold. The solid lines show the Drude-Lorentz model and dashed lines are obtained from the experimental data by Johnsson and Christy.

2.1.2 Optical properties of subwavelength particles

We begin by considering the simple case of a spherical particle illuminated by light[6]. As the incident electric field **E** interacts with the sphere, it induces charge displacement within the particle. These displaced charges can cause an electric, vibrational, or virtual transition within the sphere. If as a result of this interaction a secondary electromagnetic wave re-radiate, then light is scattered. Otherwise, light is absorbed by the particle. For a homogenous spherical particle, an analytical solution to the scattering problem exists. By solving Maxwell's equations in spherical coordinates, one obtains an infinite series of vector spherical harmonics describing the electromagnetic field at any point. This approach, developed by Gustav Mie in 1908, is now known as Mie theory.

While Mie theory is a powerful analytical tool, its infinite multipole sums often obscure intuitive physical insights into the optical properties of the sphere. Therefore, to simplify our analysis, we take an additional step.

Quasi-static (Rayleigh) Approximation

If the sphere radius (a) is much smaller than the wavelength of incident light in the surrounding medium (λ_m), the spatial variation of the field within the particle can be neglected. Under this condition, the charge displacement and the scattered field behave as that of a simple electric

[6] Although the nanostructures used in our experiments are not spherical, yet this simplification helps us to provide a useful model for further discussions.

dipole. This approximation is known as the quasi-static approximation or Rayleigh approximation [112, 113].

As a matter of fact, we made the same assumption when calculating the permittivity of dielectrics, where bound electrons—treated as small oscillating dipoles—respond to an applied electric field. Thus, although we have reduced our study from a bulk material to a subwavelength particle, the scale of displacement has increased from atomic dimensions to tens or hundreds of nanometers.

To develop our model, we consider that the particle has a complex relative permittivity $\epsilon_p = N^2$, and the surrounding medium has a real relative permittivity $\epsilon_m = n'^2$.

The induced dipole moment due to the incident electric field $\mathbf{E}$ is given by:

$$\boldsymbol{\mathcal{P}} = \epsilon_0 \epsilon_m \alpha(\omega) \mathbf{E}\,, \tag{2-20}$$

where $\alpha(\omega)$ is the polarizability of the sphere. By solving the Laplace equation for the electrostatic case and applying appropriate boundary conditions (details outlined in [114]) the polarizability is found to be given by:

$$\alpha(\omega) = 4\pi a^3 \frac{\epsilon_p - \epsilon_m}{\epsilon_p + 2\epsilon_m}\,, \tag{2-21}$$

This equation is known as the Clausius-Mossotti relation. The time averaged radiated (scattered) power by an oscillating electric dipole is given by:

$$P_{sca} = \frac{c^3 |\mathbf{k}|^4}{12\pi} |\boldsymbol{\mathcal{P}}|^2 = \frac{c^3 |\mathbf{k}|^4}{12\pi} \epsilon_0{}^2 \epsilon_m{}^2 |\alpha(\omega)|^2 |E_0|^2\,, \tag{2-22}$$

The scattering cross section is defined as the ratio of the scattered light power from the particle and the incident light intensity, $I_{inc} = \frac{1}{2}\sqrt{\epsilon_m \epsilon_0}|E_0|^2$:

$$\sigma_{sca} = \frac{P_{sca}}{I_{inc}} = \frac{\frac{c^3 |\mathbf{k}|^4}{12\pi} \epsilon_0{}^2 \epsilon_m{}^2 |\alpha(\omega)|^2 |E_0|^2}{\frac{1}{2}\sqrt{\epsilon_m \epsilon_0}|E_0|^2} = \frac{|\mathbf{k}|^4}{6\pi} |\alpha(\omega)|^2. \tag{2-23}$$

Similarly, the absorption cross section is defined as the ratio of the power dissipated by a dipole P_{abs} due to absorption and the incident light intensity:

$$P_{\text{abs}} = \frac{\omega}{2}\text{Im}\{\boldsymbol{\mathcal{P}} \cdot \mathbf{E}^*\} = \frac{\omega}{2}\text{Im}\{\epsilon_0\epsilon_m\alpha(\omega)\mathbf{E} \cdot \mathbf{E}^*\} = \frac{\omega}{2}\epsilon_0\epsilon_m|E_0|^2\text{Im}\{\alpha(\omega)\}. \quad 2\text{-}24$$

Therefore σ_{abs} can be calculated as:

$$\sigma_{\text{abs}} = \frac{P_{\text{abs}}}{I_{\text{inc}}} = \frac{\frac{\omega}{2}\epsilon_0\epsilon_m|E_0|^2\text{Im}\{\alpha(\omega)\}}{\frac{1}{2}\sqrt{\epsilon_m\epsilon_0}|E_0|^2} = |\mathbf{k}|\text{Im}\{\alpha(\omega)\}. \quad 2\text{-}25$$

Now, if we replace both $\mathbf{k}$ with $\frac{2\pi}{\lambda_m}$ and $\alpha(\omega)$ from 2-21, in 2-23 and 2-25, we will have:

$$\sigma_{\text{sca}} = \frac{2}{3\pi}\frac{(2\pi a)^6}{\lambda_m^4}\left|\frac{\epsilon_p - \epsilon_m}{\epsilon_p + 2\epsilon_m}\right|^2, \quad 2\text{-}26$$

$$\sigma_{\text{abs}} = \frac{(2\pi a)^3}{\pi\lambda_m}\text{Im}\left(\frac{\epsilon_p - \epsilon_m}{\epsilon_p + 2\epsilon_m}\right). \quad 2\text{-}27$$

Thus, we have derived the scattering and absorption cross-sections for subwavelength spherical particles based on their relative permittivities.

Metallic Structures: Plasmonic Resonances

Despite the simplifications, the derived expressions for σ_{sca} and σ_{abs} reveal crucial insights. In particular, if the condition $\epsilon_p = -2\epsilon_m$ is satisfied, an optical resonance known as the Localized Surface Plasmon Resonance (LSPR) occurs.

This condition is only met when the real part of the particle's permittivity is negative, a property unique to metals due to the behaviour of free electrons in the conduction band. Essentially, LSPR results from the collective oscillation of these free electrons in response to an external electric field.

Figure 2.4 illustrates the σ_{sca} and σ_{sca} of a gold sphere in water as its radius varies from 20 to 80 nm. The relative permittivity of gold was taken from the Johnson & Christy experimental data.

In geometrically anisotropic particles, such as spheroids and ellipsoids, the polarizability varies along each principal axis ($i = 1, 2, 3$), resulting in different absorption cross-sections that depend on the polarization angle of the incident light relative to each axis. Consequently, the amount of absorbed light varies with the polarization of the incident light.

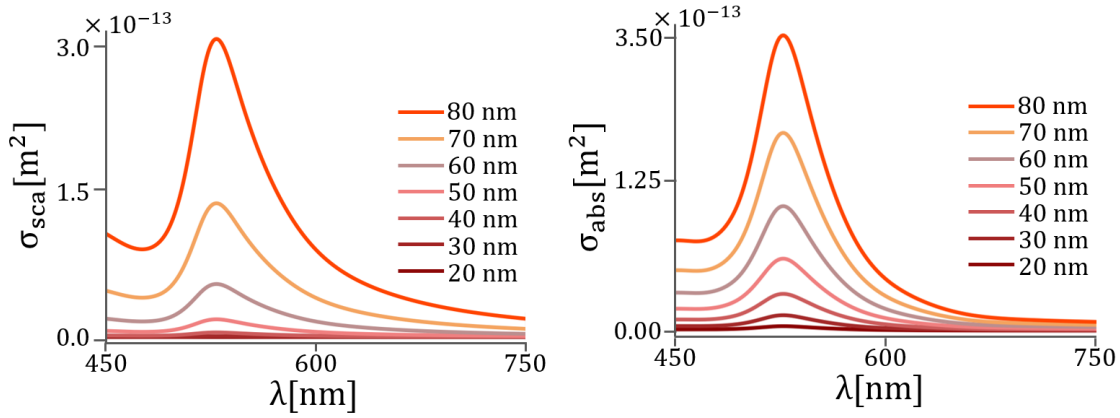

Figure 2.4 Absorption spectra of gold nanospheres in water calculated by dipole approximation as their radius increases from 20 nm to 80 nm. (The relative permittivity of gold was adopted from Johnson & Christy experimental data [111]).

For a homogeneous spheroid or ellipsoid with permittivity ϵ_p embedded in a medium with permittivity ϵ_m, the polarizability $\alpha_i(\omega)$ along a principal axis i is given by [9]:

$$\alpha_i(\omega) = \frac{V(\epsilon_p - \epsilon_m)}{\epsilon_m + L_i(\epsilon_p - \epsilon_m)}, \qquad 2\text{-}28$$

where V is the volume of the particle and L_i is the geometrical depolarization factor along the $i-th$ axis. For any ellipsoid, the sum of this factor for the three axes must be 1 ($L_1 + L_2 + L_3 = 1$). In general, when a particle is elongated along one axis, the LSPR along that axis shifts to longer wavelengths. This shape-dependent effect can be simply described using an anisotropic dynamical polarizability tensor. If the axes of the ellipsoid are aligned with the Cartesian coordinate system, the polarizability tensor takes a diagonal form [31]:

$$\alpha(\omega) = \begin{Bmatrix} \alpha_1(\omega) & 0 & 0 \\ 0 & \alpha_2(\omega) & 0 \\ 0 & 0 & \alpha_3(\omega) \end{Bmatrix}. \qquad 2\text{-}29$$

For ellipsoidal particles, analytical expressions exist for the depolarization factors, and their optical cross-sections can be determined using the Mie-Gans formalism in the quasi-static limit [9]:

$$L_i = \frac{a_1 a_2 a_3}{2} \int_0^\infty \frac{du}{(u+a_i^2)\sqrt{(u+a_1^2)(u+a_2^2)(u+a_3^2)}}. \qquad 2\text{-}30$$

A key limitation of the quasi-static approximation is that the resonance condition $\epsilon_p = -2\epsilon_m$ suggests that the resonance wavelength λ_{LSPR} depends only on the material's permittivity and the surrounding medium, but not on the particle size. However, in reality, the LSPR shifts as the particle size increases. This occurs due to dynamic depolarization (retardation effect) and radiative damping effects [9, 115-117].

The dynamic depolarization effect comes from the fact that the particle can no longer be considered as a point-like oscillating dipole. When the particle size increases, the incident electric field may be different in phase from one location to another, leading to a phase lag between the driving field and the induced dipole moment. This phase lag reduces the effective polarizability, shifting the resonance to lower frequencies (longer wavelengths).

Radiative damping refers to energy loss due to the emission of electromagnetic radiation from the oscillating electron cloud. In plasmonic nanoparticles, such as gold spheres, radiative damping increases with particle size, broadening the resonance and shifting it to longer wavelength.

Moreover, as we mentioned, the dipole approximation is valid only for very small particles ($a \ll \lambda_m$). As the size increases, quadrupole and higher-order modes contribute to the optical response. These modes resonate at shorter wavelengths and correspond to higher-order charge distributions.

Another limitation of the dipole approximation is its inability to account for variations in the refractive index of the surrounding medium, such as when a nanostructure is placed on a glass substrate in water.

Due to these limitations, numerical methods are required to accurately estimate the optical response of nanostructures. In this thesis, we use the commercial Finite Element Method (FEM) solver, COMSOL Multiphysics, to numerically compute the absorption and scattering spectra of our structures.

Finally, we can clearly understand and describe the phenomenon observed by Michael Faraday in 1857. As we have seen, the intensity and wavelength of light scattered by metallic nanoparticles depend on their radius, and shape. Consequently, by varying the size or shape of gold particles suspended in water, the solution exhibits different colours.

Figure 2.5 illustrates how the absorption cross section of gold nanospheres changes as their radii increases from 20 nm to 80 nm. The relative permittivity of gold was adopted from Johnson & Christy experimental data.

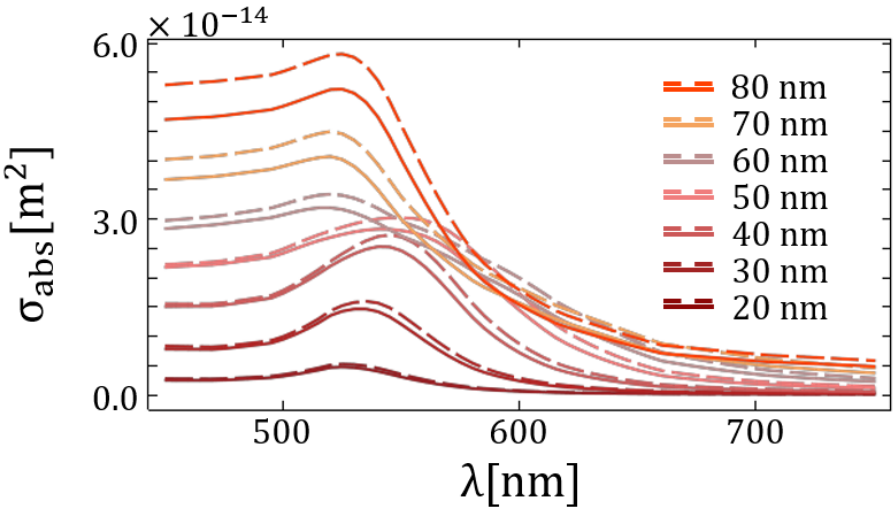

Figure 2.5 Absorption spectra of gold nanospheres in water calculated by FEM simulations as their radius increases from 20 nm to 80 nm. Dashed lines show the absorption cross section when the nanospheres are located on glass (the relative permittivity of gold was taken from the Johnson & Christy experimental data [111]).

At smaller radii (20–40 nm), the shape and intensity of the absorption cross section closely resemble those predicted by the dipole approximation. However, as the radius increases, the influence of higher-order modes becomes evident at shorter wavelengths. Additionally, λ_{LSPR} shifts toward longer wavelengths due to dynamic depolarization (retardation) and radiative damping effects. Once the radius exceeds 50 nm, higher-order multipolar modes (such as quadrupole and octupole) start contributing significantly. At the same time, the dipole mode weakens and broadens relative to these higher-order modes due to radiative damping, effectively shifting the spectral weight of the peak towards shorter wavelengths.

Figure 2.6 compares the absorption cross sections of gold nanodisks with different geometries: an ellipsoidal nanodisk with a long-axis diameter of 100 nm, a short-axis diameter of 50 nm, and a height of 60 nm, and a circular nanodisk with a radius of 50 nm and a height of 60 nm. As observed, compared to the circular disk, λ_{LSPR} for the ellipsoid is red-shifted along the long axis and blue-shifted along the short axis. These are the plasmonic structures we used in Paper I for optical heating.

Dielectric structures: geometrical (Mie) resonances

Dielectric materials, such as silicon, lack the free electrons that drive plasmonic resonances. Instead, their optical response is governed by Mie resonances. These resonances arise from constructive interference of electromagnetic waves inside or around the particle, leading to

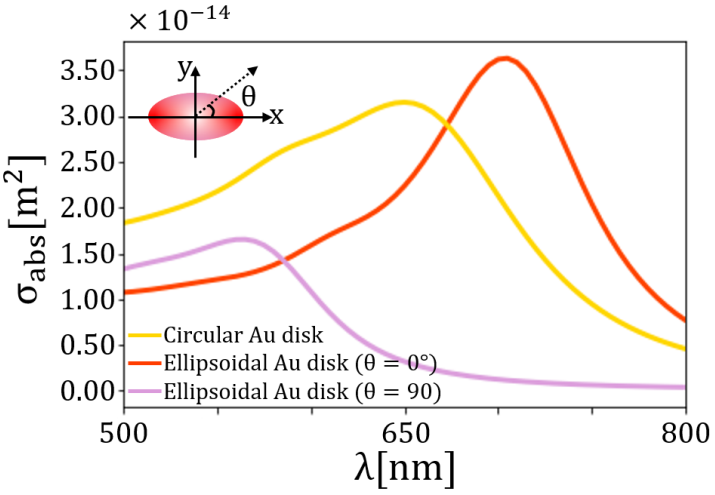

Figure 2.6 Absorption spectra of gold nanodisks (yellow, diameter 100 nm, height 60 nm) and nano ellipsoids (long axis diameter 100 nm, short axis diameter 50 nm, height 60 nm), on glass and in water, for incident polarization parallel (red) and perpendicular (purple) to the long axis (the relative permittivity of gold was taken from the Johnson & Christy experimental data [111]).

enhanced scattering and absorption. Unlike plasmonic resonances, which are material-dependent, Mie resonances are primarily governed by particle geometry. This is similar to how whispering gallery modes or Fabry-Pérot cavities trap light in confined spaces [104, 105].

Dielectric particles support both electric and magnetic multipole modes. In particular, the lowest-order **magnetic dipole mode** arises from the displacement current circulating within the high-refractive-index particle [118-120].

Although the intrinsic absorption (i.e., $\mathrm{Im}\{\epsilon_r(\omega)\}$) in dielectrics is low, the strong field confinement enabled by Mie resonances enhances absorption. The confined light inside the nanoparticle undergoes multiple interactions with the material due to internal reflections and interactions, effectively increasing the optical path length. As a result, even weakly absorbing materials can absorb more energy due to prolonged light confinement, leading to enhanced absorption [59].

Even though the position of the electric and magnetic multipoles responses in dielectric spherical particles can be precisely calculated by Mie theory, same as for metallic structures, several factors, such as radiative losses, geometrical anisotropy, and inhomogeneities in the surrounding medium, can shift and modify the resonance wavelengths. Consequently, Finite Element Method (FEM) simulations remain a more reliable approach for accurately estimating the optical cross-sections of dielectric nanostructures.

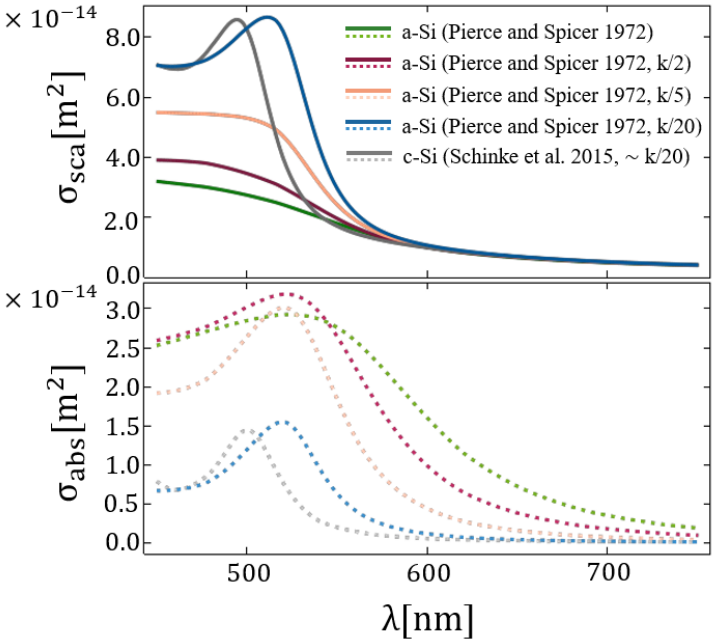

Figure 2.7 Scattering and absorption spectra of c-Si and a-Si nanodisks (diameter 100 nm, height 100 nm) calculated by FEM simulations. (The relative permittivity of c-Si was taken from the Schinke et al. 2015 [121], and the relative permittivity of a-Si was taken from the Pierce and Spicer (1972) [122] where its imaginary part was divided by 2, 5 and 20 in the corresponding curves).

Figure 2.7 shows the absorption and scattering cross-section of crystalline silicon (c-Si) and amorphous silicon (a-Si) circular nanodisks with a radius of 50 nm and a height of 100 nm calculated by FEM simulations. The a-Si disks were used in Paper II for optical heating, and currently we are using the c-Si disks for optical heating and Raman thermometry. As can be observed, despite the low intrinsic absorption of these materials, both of the show enhanced absorption due to dipole magnetic Mie resonances. To make sure that the enhanced absorption is due to this Mie resonances, the imaginary part of the refractive index (k) for amorphous silicon (a-Si) was systematically reduced, while keeping the real part (n) constant, using data from Pierce and Spicer (1972) [122]. Specifically, we considered cases where k_{a-Si} was divided by 2, 5 and 20. It is clear that, as k_{a-Si} decreases, the scattering and absorption cross-section spectra of the a-Si nanodisks increasingly resemble the c-Si nanodisk spectra, which is dominated by the MD resonance. This similarity thus confirms that the broad absorption peak for a-Si in Figure 2.7 is indeed due to the MD resonance, though it is broadened by the larger k_{a-Si} compared to k_{c-Si}.

2.2 Heat generation by subwavelength particles

So far, we realized that subwavelength nanostructures are able to enhance the scattering and absorption of light at specific wavelengths in the visible and near-infrared regions due to their optical resonances. When metallic nanostructures are excited by light, the energy of incident photons will excite the collective oscillation of electrons which drives a current within the metal. Owing to the lossy nature of the metallic structures in optical frequencies, resistive heat will be generated in them. In dielectric structures, the field confinement achieved through Mie resonances enhances the absorption. This mechanism leads to localized heating despite the absence of significant Ohmic losses. To better understand why both materials with high ohmic losses, metals, and materials with low ohmic losses, dielectrics, are able to generate heat one should start the consideration from the classical general expression for the absorbed electromagnetic power P_{abs} [9, 59]:

$$P_{\mathrm{abs}} = \frac{1}{2}\mathrm{Re}\int_{\mathrm{V}} \mathbf{J}^{*}(\mathbf{r})\mathbf{E_{in}}(\mathbf{r})\mathrm{dV}, \qquad 2\text{-}31$$

where $\mathbf{J}(\mathbf{r})$ is the current density, and $\mathbf{E_{in}}(\mathbf{r})$ is the electric field inside the particle, and the integration is performed over the volume of the considered nanoparticle V. Eq. 2-31 yields that the absorbed power can either be increased by increasing the current density, or by enhancing the field inside the nanoparticle, or the combination of both mechanisms. An enhanced absorption is observed in metallic particles due to both large ohmic loss, and field enhancement. In the dielectrics in the other hand, it is dominantly due to the field enhancement inside the nanoparticle. We have used the expression in Eq. 2-31 to calculate and absorbed electromagnetic power in our FEM simulations. Another way to estimate the delivered power by the nanostructure, is by the absorption cross section by [7, 9]:

$$\mathrm{q(r)} = \sigma_{\mathrm{abs}}\mathrm{I(r)/V}, \qquad 2\text{-}32$$

where $\mathrm{I(r)}$ is the irradiance of the incident light, and V. This expression is quite useful for simple estimation of nanostructures heating, as well as for temperature distribution analysis.

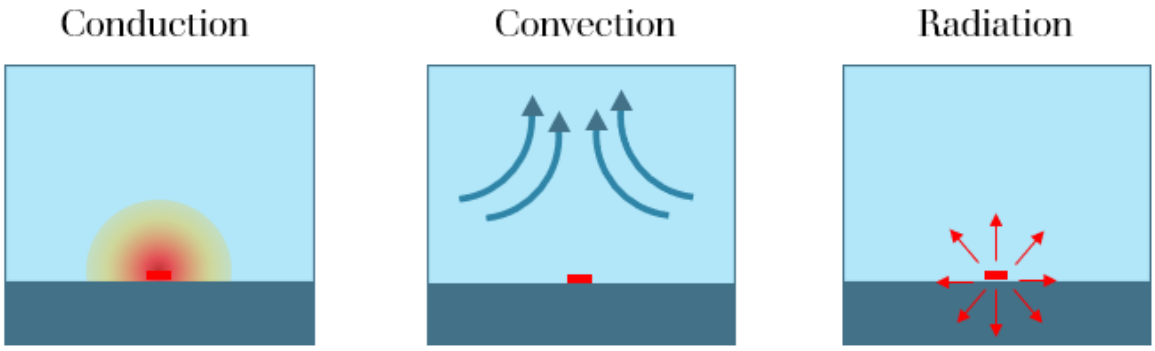

Figure 2.8 Overview of heat transfer mechanism discussed: conduction, convection and radiation.

After the generated heat (absorbed power) is calculated, it is possible to calculate the heat dissipation within the nanoparticle and the surrounding medium. To do so, we can consider two main heat transfer mechanisms: conduction and convection (shown in Figure 2.8). Due to the conservation of energy [123-126]:

$$\left(\rho C_p \frac{\partial T}{\partial t} - \kappa \nabla^2 T\right) + \rho C_p \mathbf{u} \cdot \nabla T = q, \qquad 2\text{-}33$$

where ρ, C_p, κ are the material density, heat capacity at constant pressure, and thermal conductivity, and q is the calculated heat source density [123-126]. C_p determines how much energy is required to increase the temperature of the material, normalized by the mass, and κ describes the relation between the heat flux and the local temperature gradient, in other words, it describes the ability of the material to conduct heat.

The first term in Eq. 2-33 models the conductive heat transfer. Conduction is the process of thermal energy transport via collisions between neighbouring atoms/molecules.

The second term in Eq. 2-32 models the convective heat transfer. In this mechanism, thermal energy transport is due to the flow of the hot fluid molecules, and it is governed by the fluid velocity field, $\mathbf{u}$. We will talk more about the heat induced fluid flows in Chapter IV.

It should be mentioned that, in addition to convection and conduction, radiation is the third fundamental heat transfer mechanism. However, this mechanism is generally inefficient in our systems. As a result, it has been neglected in all of the simulations done in this thesis [126].

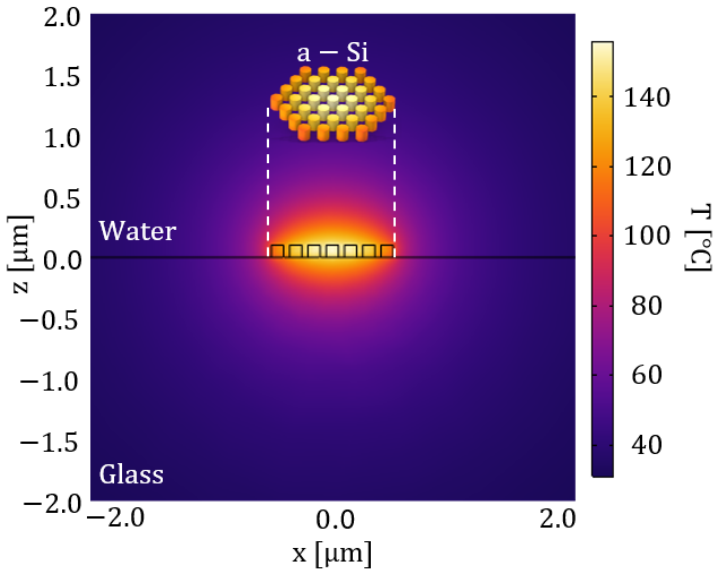

Figure 2.9 FEM simulation of the temperature field around an isolated array of 37 a-Si nanodisks, each with diameter and radius 100 nm heated by a 532 nm wavelength laser with irradiance I = 0.2 mW/mm^2.

If we consider the steady state condition, Eq. 2-33 can be simplified to:

$$-\kappa\nabla^2 T + \rho C_p \mathbf{u} \cdot \nabla T = q. \qquad 2\text{-}34$$

This is the governing equation in our heat transfer simulations.

Figure 2.9 shows the temperature field around one of the arrays that we have used in our experiments. In general, in all our experiments we have used isolated array of nanostructures for optical heating. In the previous sections, we have shown the absorption cross-sections of nanostructures used in these arrays. The array shown in Figure 2.9 consists of circular a-Si nanodisks with height and diameter of 100 nm, which has been heated by a 532 nm wavelength laser. We will refer to the laser that is used for hearing as the heating laser from this point onward.

As it can be observed, despite their small sizes, these arrays are capable of heating their surroundings significantly. Therefore, if put in water, they are able to vaporize the surrounding water and generate micro vapor bubbles. However, this mechanism might not be as simple as it sounds. In the next chapter we will get familiar with the basics of boiling and micro bubble nucleation.

Chapter III: Optically Induced Bubbles

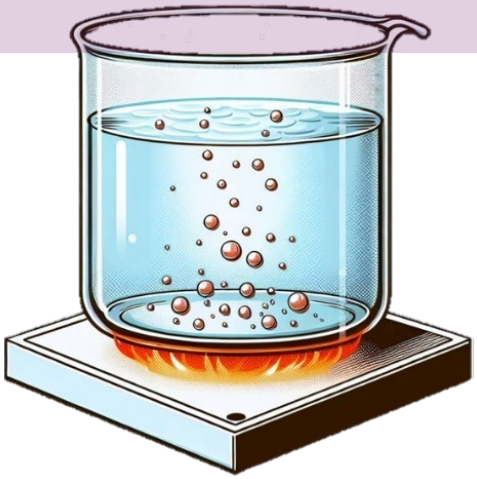

"Boiling is an extremely complex and illusive process, which continues to baffle and challenge inquisitive minds."

- Vijay K. Dhir

Boiling, a distinct branch of thermophysics, is a common phenomenon in everyday life, whether we are heating water for cooking or preparing a cup of coffee. Despite its familiarity, the term "boiling" is often used imprecisely. Scientifically, it refers to a rapid vaporization process characterized by a high rate of liquid-to-vapor phase change. This process involves the nucleation and growth of individual vapor bubbles, which typically form at a solid-liquid or liquid-liquid interface [127].

The behavior of these vapor bubbles, individually and as part of dynamically evolving bubble systems, plays a critical role in determining the characteristics of heat transfer and flow dynamics. Understanding these behaviors is essential for explaining and predicting boiling phenomena across various scales [128].

Figure 3.1 shows the phase diagram of water, which consists of three main regions: solid region (ice), liquid region (water), and gas region (steam or vapour). The boundaries that separate the different phases of water, and where adjacent phases coexist, are called saturation lines or equilibrium lines. At the triple point, water exists simultaneously in the solid, liquid, and gas phases. Phase transitions can take place at different temperatures and pressures between adjacent regions in the diagram. The purple arrows show different kinds of phase transitions and their directions at a constant pressure. In the boiling process, saturation temperature (T_s) is defined as the temperature at which water starts boiling (condensing, in the reverse direction)

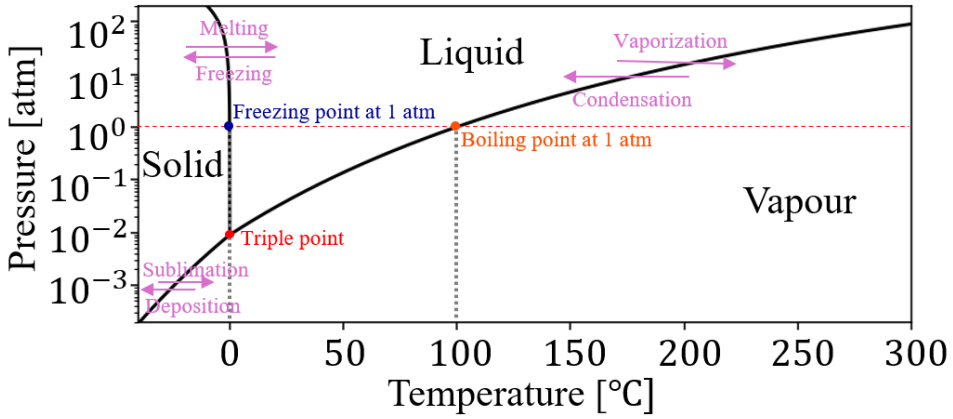

Figure 3.1 Phase diagram for water. Dotted vertical lines indicate important temperatures at atmospheric pressure: freezing point, and boiling point.

at a given pressure. For example, at 1 atm (101.3 kPa), the saturation temperature is 100°C. One can also define the saturation pressure as the pressure at which water starts boiling (or condensing) at a given temperature. For example, at 100°C, the saturation pressure is 1 atm (101.3 kPa). The liquid is said to be superheated when the ambient temperature (T_∞) is larger than T_s ($T_\infty > T_s$) and subcooled when T_∞ is smaller than T_s ($T_\infty < T_s$). We will later see how the saturation line and the saturation temperature for boiling is affected by the heat source size and the water content [129, 130].

In this chapter, we explore the fundamental aspects of boiling. We begin with the "pool boiling" around macro-scale heaters and then examine how boiling dynamics change as the heater size decreases to the micro- and nanoscale. Finally, at sufficiently small heater sizes, where the boiling process becomes dominated by the dynamics of a single microbubble, we focus on the nucleation, growth, and collapse of this bubble, as well as the forces it experiences.

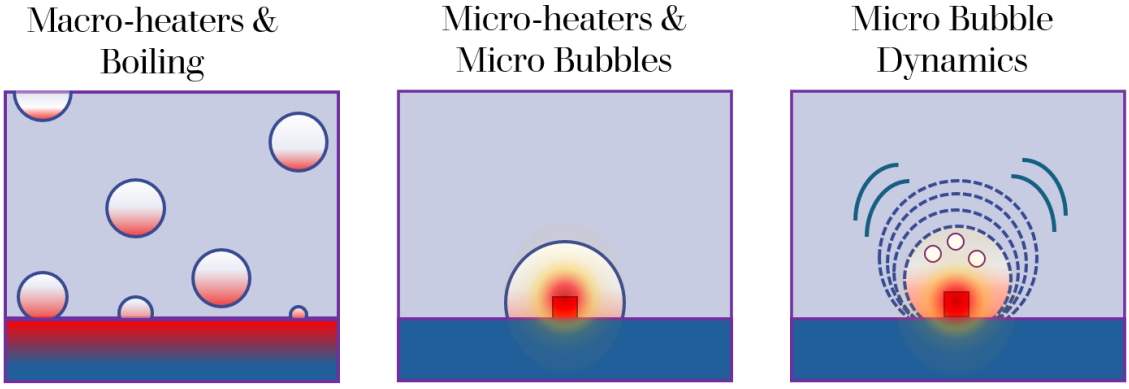

Figure 3.2 Outline of Chapter III.

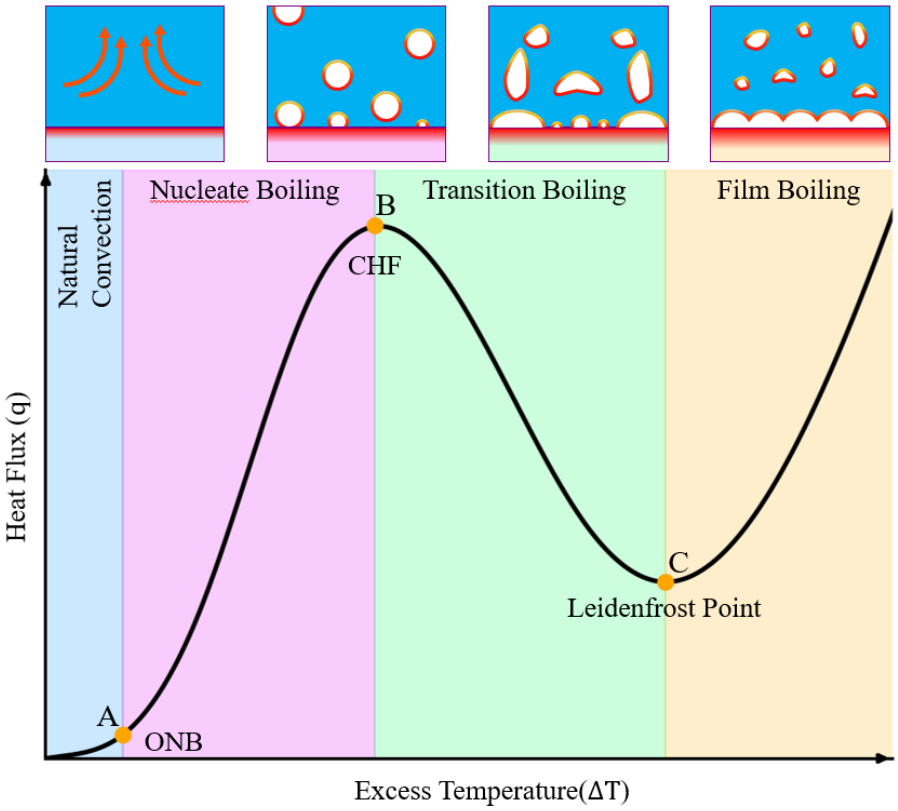

Figure 3.3 Typical boiling curve for an unspecified heater.

3.1. Basics of Boiling

Boiling is a rapid phase transition from liquid to vapor, during which **vapor bubbles** nucleate either on a heated surface or within a superheated liquid layer adjacent to it. This phenomenon can be categorized into two main types based on the flow conditions of the surrounding fluid: **pool boiling** and **flow boiling** (also known as forced convective boiling) [131-133].

- **Pool boiling** occurs on a heated surface submerged in a pool of initially stationary liquid. In this scenario, fluid motion arises naturally due to temperature gradients.
- **Flow boiling**, on the other hand, takes place in a forced stream of fluid, typically driven by an external pump. Here, the heating surface is often the channel wall confining the flow.

This chapter focuses on **pool boiling**, as it closely aligns with the conditions of our experiments.

In pool boiling, the fluid near the heating surface starts off stationary, with fluid motion developing later due to free convection and the circulation driven by bubble growth and detachment. The two key parameters in these problems are the wall superheating, or excess temperature, $\Delta T = T_w - T_s$, which is the temperature difference between the heated surface, T_w, and the liquid's saturation temperature, T_s, at the local pressure, and the heat flux q. A typical pool boiling curve for an unspecified heater, which is a plot of heat flux versus excess temperature (ΔT), is shown in Figure 3.3. As ΔT increases, the curve traverses four different regions of pool boiling: (I) free convection, (II) nucleate boiling, (III) transition boiling, and (IV) film boiling [132, 134, 135].

The first region of the boiling curve, extending up to point A, corresponds to natural convection. In this phase, the slightly superheated single-phase liquid rises from the heating surface, and heat is dissipated primarily through free convection to the liquid's free surface.

Nucleate boiling occurs between points A and B and can be further divided into two distinct sub-regions: Isolated Nucleate Boiling and Slug Nucleate Boiling. At lower heat fluxes, beginning at point A, isolated vapor bubbles start to form on the heating surface. This marks the onset of nucleate boiling (ONB). In this stage, heat transfer primarily occurs from the heated surface to the liquid. As ΔT increases, more nucleation sites become active, leading to the formation of bubbles that merge, interact, and rise as slugs, jets, or columns of vapor [132, 134, 135].

At point B, the heat flux reaches its maximum, known as the critical heat flux (CHF) or burnout heat flux. Beyond this point, the heat flux decreases with increasing wall superheat, marking the Transition Boiling or unstable film boiling region (between points B and C). In this phase, an unstable and partial vapor film begins to form on the heating surface, causing oscillations between nucleate boiling and film boiling. This intermittent vapor formation hinders direct liquid contact with the surface, which reduces heat transfer efficiency as the liquid's high thermal conductivity is blocked by the vapor layer, and as a result the boiling curve turns down [132, 134, 135].

Finally, if the temperature is high enough to overcome the thermally insulating effect of the thin vapor film, Film Boiling occurs beyond point C and the heat flux again increases with increasing wall superheat. In this regime, the heating surface becomes fully covered by a stable vapor film. Heat transfer now occurs through a combination of conduction, convection, and

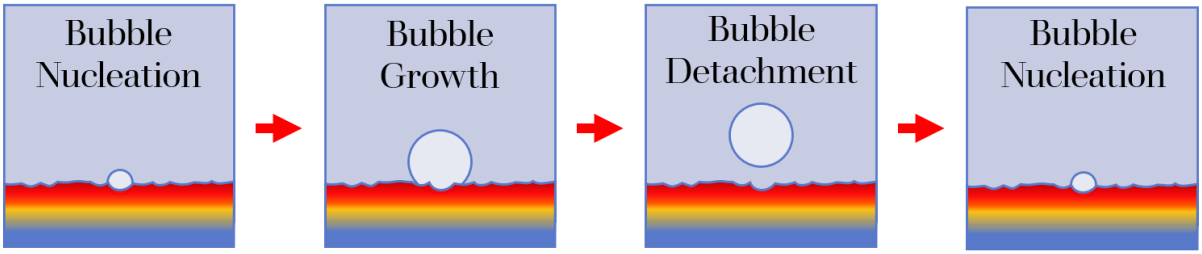

Figure 3.4 Various bubble stages in Nucleation boiling on an unspecified heated wall.

radiation. At excess temperature levels characteristic of this phase, radiation becomes a significant mode of heat transfer. The point of minimum heat flux, referred to as point C, is known as the Leidenfrost point, while the transition to film boiling is called the Leidenfrost effect, both named after Johann Gottlob Leidenfrost [132, 134-136].

It must be noted that as insightful and applicable as the typical boiling curve is, it can differ significantly with heater size and arrangement. For example, it has been observed that as the heater size decreases, the boiling curve moves towards higher heat fluxes with corresponding higher superheats, and the unique heat transfer processes associated with boiling on a microheater are considerably different from those typically observed during boiling on macroscale heater [137-139].

During the initial stages of nucleate pool boiling on a heated surface, individual bubbles are repeatedly formed on a cyclic process of nucleation, growth, detachment, and subsequent nucleation, as illustrated in Figure 3.4 [131, 140].

Bubble nucleation typically occurs at concave pits, cracks, or other surface imperfections where gas nuclei are trapped, serving as nucleation sites. The surface roughness and the availability of these pre-existing sites play a pivotal role in determining the bubble nucleation temperature. Generally, the rougher the surface and the greater the number of nucleation sites, the more easily the boiling process initiates [131, 140].

The growth of bubbles on a heated surface is governed by several heat transfer mechanisms, including the evaporation from the superheated Thermal Boundary Layer (TBL) around the bubble, micro-convection induced by the liquid motion resulting from the bubble growth, the evaporation of the liquid microlayer trapped beneath the bubble and, debatably, the

thermocapillary (Marangoni) convection (We will discuss the Marangoni convection in Chapter IV) [131].

These mechanisms collectively dictate the bubble's growth rate and behaviour throughout its lifecycle. Throughout the stages of nucleation and growth, bubbles are subject to various forces that depend on their state and the surrounding conditions. For a bubble attached to a heated surface during nucleate boiling, the dominant forces include surface tension, liquid static pressure, and excess vapor pressure, with the gravitational force often being negligible. Surface tension stabilizes the bubble by maintaining its interface, while liquid static pressure acts as a compressive force from the surrounding fluid. Excess vapor pressure drives bubble growth by overcoming the liquid pressure and surface tension. These forces primarily determine the bubble's stability and growth at the nucleation site. Eventually, if the bubble detachment forces overcome the force dragging the bubble, the bubble detach from the heating source [140].

Once a bubble detaches from the surface, additional forces come into play due to its dynamic motion through the liquid. These include buoyancy, which drives the bubble upward due to density differences, and quasi-steady drag, which resists its motion. Inertia-related effects are captured by the added-mass force, which accounts for the displaced liquid's acceleration. Surface tension gradients can induce the Marangoni force, influencing the bubble's movement in the presence of temperature or concentration gradients. We will discuss the forces driving the motion of micro bubbles in more details in section 3.3 [75, 140].

During detachment, heat transfer mechanisms include forced convection, transient heat conduction, and the reformation of the thermal boundary layer. Forced convection arises from the agitation of the liquid caused by the bubble's departure, which disrupts the thermal boundary layer and induces the flow of cooler liquid toward the heated surface. This replenishing liquid absorbs heat, enhancing the overall heat transfer process. Transient heat conduction occurs during the rewetting of the surface immediately after bubble departure, as the temperature field adjusts to the thermal disturbance created by the departing bubble. Simultaneously, the thermal boundary layer, disrupted by the bubble motion and detachment, begins to reform, re-establishing the gradient necessary for heat transfer from the surface to the liquid. Figure 3.5 shows the heat transfer mechanisms that a bubble experience (a) at the nucleation site and (b) after the departure [140].

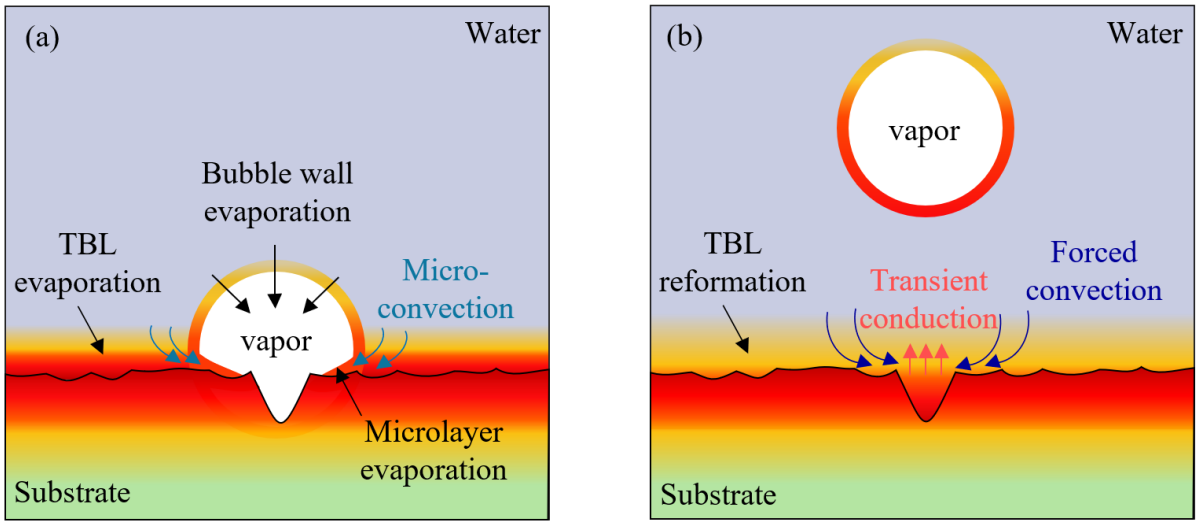

Figure 3.5 Heat transfer mechanisms in pool boiling (a) during the bubble nucleation and growth on the site (b) after the bubble departure.

As previously mentioned, variations in the size of the heater or the heated area significantly influence the heat transfer mechanisms and bubble dynamics. The processes of bubble nucleation, growth, the forces involved, and their behaviour at the micro- and nanoscale, representative of our experiments, will be discussed in greater detail in Section 3.2.

The formation of bubbles in the boiling process is categorized into two types: homogenous nucleation and heterogeneous nucleation. As the name suggests homogenous nucleation occurs uniformly throughout the liquid without any preferential sites for bubble formation. This form of nucleation occurs on smooth surfaces where specific sites for bubble nucleation does not exist. As a consequence of the absence of nucleation cites, it is possible to attain remarkably large degrees of superheat before the beginning of homogeneous nucleation leading to a spontaneous vapor explosion known as Boiling Liquid Expanding Vapor Explosion (BLEVE). On the other hand, heterogenous nucleation occurs on rough surfaces with preexisting nucleation sites. The superheating around the bubbles nucleated on these sites is not uniform because of the thermal boundary layer and micro-liquid layer, making the growth of bubbles in heterogenous boiling more complex than in homogenous boiling. This complex phenomenon is affected by many factors such as surface microstructure, wettability, local thermal conditions, system pressure, and fluid thermophysical properties [131].

As previously discussed, the size of the heater plays a critical role in determining the heat transfer characteristics and boiling mechanisms. When the dimensions of the heater are

reduced, the heated surface area and the number of active nucleation sites decrease correspondingly. Ultimately, at sufficiently small heater sizes, the boiling process transitions to being dominated by the dynamics of a single bubble. Furthermore, as we will explain in the subsequent sections micro- and nano-scale heaters impose physical constraints on bubble growth, preventing bubbles from reaching larger sizes.

At these scales, forces such as surface tension and the Marangoni force become dominant, while gravitational forces become negligible. This shift in force dominance causes bubbles to remain pinned to the heating surface. The pinning of bubbles significantly alters the heat transfer mechanisms in the surrounding region, leading to distinct thermal and fluid dynamics compared to larger-scale boiling systems. Interestingly, this transition can also give rise to novel boiling regimes, such as explosive boiling and oscillatory boiling [131].

However, an important question arises: if the size of the heater becomes smaller than the single nucleated bubble, would a single bubble effectively act as a vapor film covering the entire heating surface? Consequently, could any boiling regime at this scale be considered reminiscent of film boiling? This intriguing possibility highlights the need to distinguish between boiling regimes based on the mechanisms of heat transfer and bubble dynamics.

In the following section, we focus on the phenomenon of boiling at the nano and microscale.

3.2. Boiling at Nano or Microscales

Microscale boiling and transient bubble nucleation phenomena have been extensively investigated over the past few decades. Initially, advances in MEMS (microelectromechanical systems) technology enabled the fabrication of heaters with dimensions down to the micrometer or even submicrometer scale. These heaters are capable of achieving much higher heat fluxes from their surfaces compared to conventional heaters. More recently, as discussed in the previous chapter, the emergence of thermoplasmonics has enabled the development of photothermal nanoscale heaters [131].

The unique characteristics of micro and nanoscale heaters, combined with advanced experimental apparatus such as advanced optical microscopes, high-speed cameras, and fast photodiodes, have fueled significant interest in exploring the differences in boiling mechanisms between macroscale and microscale systems. These investigations have revealed critical distinctions in bubble nucleation dynamics and boiling behavior on small heaters.

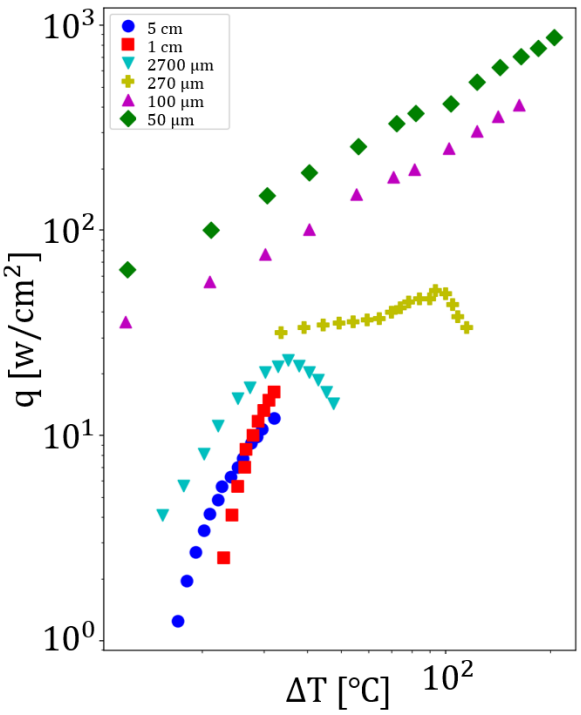

Figure 3.6 The comparison of boiling curves for different heater sizes, as reported by Chen and Chung (2003) in ref [138].

For example, Chen and Chung (2003) studied the boiling of FC-72[7] on small heaters and compared their results with previously reported data for the same fluid on larger heaters. Their findings demonstrated that, as the heater size decreases, the boiling curve shifts toward higher heat fluxes at corresponding higher superheats. Moreover, the relationship between heat flux and wall superheat becomes linear, and the nucleate boiling peak observed in classical boiling curves disappears. The comparison of boiling curves for different heater sizes, as reported by Chen and Chung (2003), is reproduced in Figure 3.6 [138].

Interestingly, Jollans, and Orrit (2019) observed a similar phenomenon when studying boiling around gold nanospheres with diameters of 80 nm. Their results showed that the nucleate boiling peak also disappears at this scale. Figure 3.6 presents the mean scattering signal from the nanospheres as a function of Back Focal Plane (BFP) heating power, as reported by Jollans, and Orrit (2019). The mean scattering signal is analogous to heat flux in classical boiling systems, as it reflects the system's thermal and vapor bubble dynamics. Similarly, BFP heating power correlates to excess temperature, as increasing laser power raises the nanoparticle's

[7] 3M™ Fluorinert™ Liquid FC-72 is a non-conductive, thermally and chemically stable liquid ideal for many direct contact single- and two-phase low temperature heat transfer applications, in testing, power electronics and other electonic applications.

temperature, akin to the heated surface in macroscopic boiling systems [141]. The mean scattering signal correlates with the amount of light scattered by the system, which depends on the size and presence of vapor nanobubbles around the nanoparticles. Larger or more stable vapor bubbles produce higher mean scattering values. Jollans, and Orrit (2019) identified four distinct boiling regimes around nanoparticles, depending on the heating power [141]:

Region I: At sufficiently low powers there is no indication of boiling.

Region II: Near the boiling threshold, sudden sharp spikes in the scattering signal indicate the rapid formation and collapse of vapor nanobubbles. Each spike corresponds to a discrete, short-lived event, after which the nanoparticle returns to its pre-boiling state.
At the single-nanoparticle scale, this region exhibits explosive boiling, characterized by intermittent bubble formation and collapse. However, if many nanoparticles are dispersed across a surface, their individual behaviours average out to resemble continuous nucleate boiling, where bubbles form and collapse across multiple vapor-generating centres.

Region III: At slightly higher heating powers, beyond the threshold for explosive boiling, vapor nanobubbles no longer fully collapse. Instead, they enter a sustainable state of random unstable sizes or stable oscillations. These oscillations occur at relatively stable frequencies (40–60 MHz) and are referred to as the oscillatory boiling regime.

Region IV: At the highest heating powers, the system transitions to a stable vapor nanobubble regime. A vapor film forms around the nanoparticle, insulating it and preventing further explosive or oscillatory boiling. The scattering signal stabilizes, indicating a steady bubble. This regime is analogous to the Leidenfrost effect observed in macroscopic systems, where a stable vapor layer insulates the heated surface.

Considering the earlier question regarding the difference between boiling regimes at the nanoscale, even when the heater is fully covered by a vapor bubble, it can be concluded that the primary distinction lies in the dynamics of the vapor layer. In film boiling, a stable vapor film forms, significantly reducing heat transfer. In contrast, other regimes involve active bubble dynamics and intermittent liquid contact, which enhance heat transfer. These differences play a critical role in governing the thermal and fluid dynamics at these scales [141].

Considering the importance of the explosive boiling, oscillate boiling and Leidenfrost boiling, we will mainly focus on these three boiling regimes in greater details in the following sections.

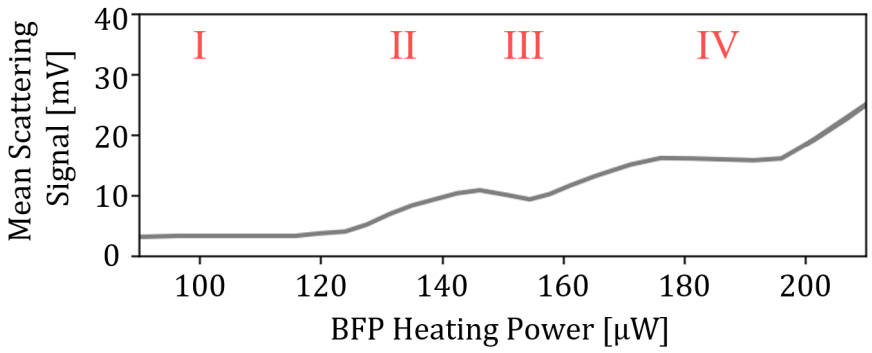

Figure 3.7 The mean scattering signal from gold nanospheres with a diameter of 80 nm as a function of Back Focal Plane (BFP) heating power, as reported by Jollans et al in ref [141].

Furthermore, our literature review and discussions will be around optically induced vapor bubbles in water using CW lasers, which resemble the experiments we did. But before discussing the bubble dynamics, it's better to first study the nucleation methods and conditions of optically induced micro bubbles.

3.3. Life cycle of the optically induced bubbles

As discussed in the previous chapter, nanoparticles can absorb light and heat up to extremely high temperatures. When these particles are immersed in water, the rising temperature can eventually exceed a critical point, leading to the nucleation of a vapor microbubble. Surprisingly, while this phenomenon appears simple, it involves highly complex mechanisms at the microscale, which have been extensively studied.

3.3.1. Bubble nucleation and growth

The normal boiling temperature of water at atmospheric pressure, referred to as the nucleation temperature (T_n) in this context, is approximately 100 ℃ (as shown in Figure 3.1). However, it has been observed that on the microscale, water can remain in a liquid state at temperatures significantly higher than 100 ℃ forming a metastable phase. The occurrence of a liquid heated above its boiling point and being in a metastable state is a phenomenon known as superheating [39, 142, 143].

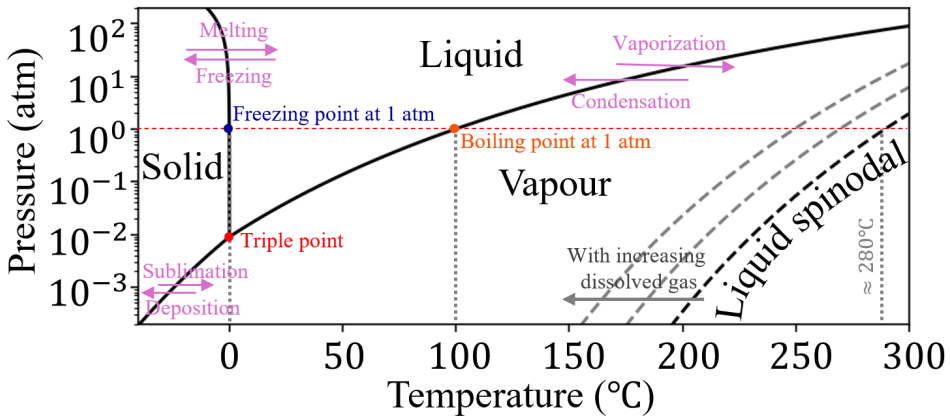

Figure 3.8 Phase diagram for water including the liquid spinodal curves and temperature at atmospheric pressure.

This shift of the nucleation temperature to higher values is primarily attributed to the absence of sufficient nucleation sites. It is well established that the formation of microbubbles occurs predominantly through heterogeneous nucleation [39]. This process typically takes place at sites where air molecules are adsorbed on the substrate surface. On the microscale, however, substrate surfaces are often smoother, reducing the availability of nucleation sites. As a result, the liquid phase can remain stable even at temperatures well above the normal boiling point. Consequently, the nucleation temperature (T_n) lies between the boiling point 100 ℃ and the spinodal temperature 280 ℃ of water at 1 atm. This represents the temperature range where the metastable liquid phase can exist before the onset of spontaneous vaporization [39, 71].

The liquid spinodal line marks the boundary where the liquid phase becomes mechanically unstable with respect to infinitesimal density fluctuations. Beyond this line, the liquid cannot exist as a distinct phase, and it spontaneously transforms into a vapor phase without the need for nucleation. While the adsorbed air molecules in the nucleation sites play a direct role in bubble nucleation and growth, they are not the only contributing factor. Air molecules dissolved in the water also play a crucial role in this process. the presence of dissolved air in the water affects both the nucleation temperature and the later growth of the bubble. It has been explained that the nucleation temperature (T_n) changes with the amount of dissolved gas, because dissolved gas molecules can also act as nucleation sites. Hence, an increase in the amount of dissolved gas reduces T_n. Lohse et al showed that by doubling the number of dissolved gases, the nucleation temperature decreases from 224 ℃ to 148 ℃ around their

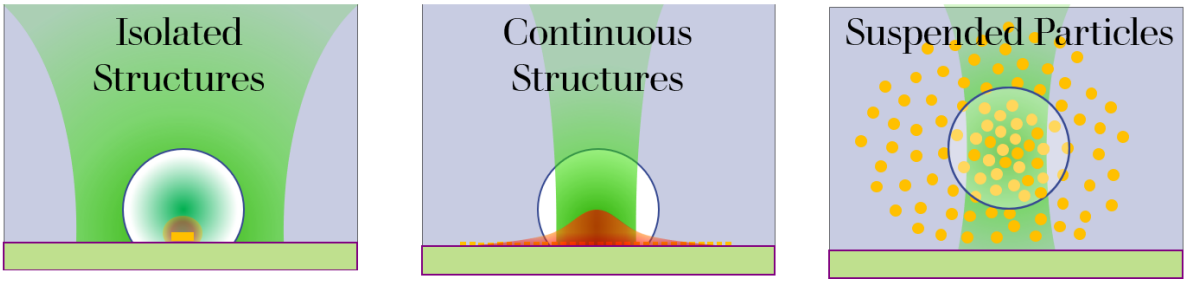

Figure 3.9 Left: Generated bubble on top of an isolated plasmonic structure. In this case, the size of the bubble is controlled by the size of the structure. Middle: Generated bubble on top of a continuous plasmonic structure. In this case, the size of the bubble is controlled with the laser focal spot size. Right: Generated bubble in the bulk of the water around the trapped plasmonic particles.

optically heated gold nano particles. The contribution of dissolved air bubbles to the later stages of the bubble growth is highly dependent on the micro heater structure [71].

A variety of micro- and nanoscale systems have been designed to generate and study microbubbles. These systems can be broadly classified into three categories: (1) continuous structures, such as thin metallic films or distributed metallic structures; (2) isolated structures on substrates, such as arrays of isolated micro/nanoparticles or single particles; and (3) suspended micro/nanoparticles in water.

For suspended particles, heating occurs either in the bulk of the water, where the particles are trapped by the laser, or on the substrate surface, where the particles are deposited due to the radiation pressure force. (The optical forces and mechanisms of optical trapping will be discussed in detail in Chapter VI.) The nucleation and growth of bubbles in the bulk are not relevant to our experiments, and will not be addressed further. On the other hand, the nucleation and growth of bubbles around deposited particles are comparable to those observed around isolated nanostructures on the substrate.

Microbubble nucleation and growth are characterized by transient and steady phases. The transient phase consists of two unstable regimes: explosive boiling and oscillatory boiling. These regimes occur within the first 1 milliseconds of bubble formation, during which the bubble primarily consists of pure water vapor [71, 75].

The steady growth phase can also be divided into two distinct regimes. The first steady regime involves the direct vaporization of superheated water and can last for up to several hundred milliseconds. This phase can be considered as film boiling at the microscale if the size of the

heater becomes smaller than the bubble. The second steady regime is driven by the diffusion of dissolved gas molecules from the superheated water into the bubble. In water, the solubility of dissolved gases decreases with increasing temperature. Consequently, if the region near the bubble is heated without vaporization, the previously air-equilibrated water becomes locally supersaturated with gas. This leads to a flux of air molecules, such as nitrogen and oxygen, into the bubble, resulting in further growth [70].

During this phase, not only does the bubble increase in size, but its internal composition also shifts. Over time, the bubble transitions from being composed primarily of water vapor to a mixture dominated by dissolved air molecules. However, in systems where the surrounding fluid has been degassed (i.e., all gaseous content has been removed), this growth stage is absent [70, 96, 144]. In the presence of continuous heating, this steady growth phase can in theory persist for long time, allowing the bubble to expand to sizes on the order of hundreds of micrometres.

We will first focus on the steady growth phase of the bubble, particularly examining how the microheater structure influences this process.

Steady phase of the bubble growth around isolated microheaters

The growth of bubbles around isolated microheaters is constrained by two primary factors: high Laplace pressure (P_L) and highly localized heating.

A spherical bubble is characterized by a pressure acting inward on its surface, which can be described using the Young–Laplace equation [145]:

$$P_{inward} = P_{amb} + P_L = P_{amb} + \frac{2\gamma}{R} \qquad 3\text{-}1$$

Here, γ is the surface tension at the gas-liquid interface (a concept explored in greater detail in Chapter VI), R is the bubble radius, and P_{amb} represents the ambient pressure, typically 1 atm. The second term in Eq. 3-1 is referred to as the "Laplace pressure."

For an air-water interface at room temperature, where the surface tension γ is approximately 72 [mN/m], the Laplace pressure equals the ambient pressure when the bubble radius R^* is

about 1.5 μm. This implies that for bubbles with radii smaller than R^*, the Laplace pressure increases significantly and becomes the dominant pressure.

The internal pressure acting outward, counteracting the inward surface pressure, can be estimated using the ideal gas law:

$$P_{outward} \propto \frac{T}{R^3} \qquad 3\text{-}2$$

For bubbles with radii smaller than R^*, the ratio of outward to inward pressure, which governs the bubble's tendency to expand, scales as $\frac{1}{R^2}$. Consequently, further growth becomes mechanically restricted as the bubble expands, eventually reaching a steady-state size.

In addition to the Laplace pressure, the localized nature of heating further limits bubble growth. The temperature increase around isolated microheaters is highly confined, with the heated region restricted to the dimensions of the microheater itself. As the bubble grows, the temperature gradient in the surrounding water decreases, making further growth by the diffusion of dissolved air molecules thermodynamically unfavourable. This means that the internal composition of the bubble around micro heaters is dominantly vapor. The combined effects of high Laplace pressure and localized heating constrain the size of these bubbles, causing them to stabilize rapidly into a steady-state configuration [44].

During the steady growth phase of the vapor bubble around a microheater, the system gradually transitions toward the film boiling regime, where the microheater becomes fully enveloped by the vapor bubble. In this regime, the thermal conductivity of vapor, which is significantly lower than that of water, results in a sharp decline in heat transfer efficiency. Consequently, thermal energy becomes trapped within the microheater, leading to a substantial increase of its temperature. This accumulation of thermal energy can drive the system into a boiling crisis, a critical condition during which the microheater may overheat, melt, or undergo structural deformation.

Steady phase of the bubble growth around continuous structures

In continuous structures, such as metal films or closely spaced plasmonic nanostructures where particle coupling occurs, the size of the bubble is initially determined by the laser's focal spot size. The high thermal conductivity of metals ensures rapid and uniform heat distribution, which eliminates localized heating. As a result, larger bubbles nucleate from the vaporization of an extended heated area.

For these larger bubbles, the inward-acting pressure is approximately equal to the ambient pressure, P_{amb}, as the influence of the Laplace pressure becomes negligible. Instead, the outward pressure is predominantly determined by the number of gas molecules transferred into the bubble, and the heater temperature. Consequently, the Laplace pressure is no longer a limiting factor for bubble growth.

Furthermore, large bubbles nucleated around distributed heating structures remain in contact with an extensive region of heated water. This ensures that a significant portion of the liquid near the gas-liquid-solid contact line is consistently exposed to elevated temperatures. In this region, the local water temperature remains sufficiently high to sustain continuous gas influx into the bubble. This process facilitates nearly unrestrained bubble growth, as the combination of distributed heating and continuous gas transfer eliminates key constraints observed in isolated structures [70]. However, by employing highly focused laser beams and substrates with efficient heat-sink properties, it is possible to minimize lateral heat spreading even in continuous structures. This enables localized heating and more controlled bubble nucleation and growth.

Transient phase of the bubble growth

The transient phase of boiling, which lasts around the first millisecond of bubble formation, consists of an explosive giant bubble nucleation followed by oscillatory boiling. The explosive boiling phase is due to the rapid and direct vaporization of water around the heater and typically occurs after a delay. The size of the bubble nucleated during this explosive phase can be up to four times larger than the steady-state bubble, and the bubble size has been shown to correlate with the delay time [71, 75].

The delay time itself is influenced by the nucleation temperature, which varies with dissolved gas concentration and laser power:

1. **Effect of gas concentration:** At a constant laser power, as the gas concentration increases and the nucleation temperature decreases, the delay time decreases. This is because less time is required for the superheated liquid to reach the reduced nucleation temperature [71].
2. **Effect of laser power:** At a constant gas concentration, increasing the laser power decreases the delay time since more energy is transmitted to the system, reducing the time needed to reach the nucleation temperature [71].

In both cases (higher gas concentration at constant laser power or higher laser power at constant gas concentration), a shorter delay time results in a smaller explosive bubble.

The sudden rapid growth of the bubble in this regime is primarily driven by the thermal energy stored in the overheated liquid layer surrounding the initial vapor shell. This layer serves as the primary energy reservoir, providing heat to sustain vaporization and bubble expansion. Three key factors influence bubble growth in this regime:

1. **Surface energy:** The creation of a larger bubble requires overcoming the surface energy, which increases with bubble radius. However, this energy cost is modest compared to the other contributions [71, 74].
2. **Latent heat of vaporization:** The transformation of liquid into vapor requires significant energy, contributing to the total energy demand for bubble expansion. This factor is particularly dominant in larger bubbles and longer time scales [71, 74].
3. **Thermal energy from the overheated liquid layer:** This is the primary energy source for rapid nanobubble expansion. The heat stored in the superheated liquid near the bubble interface is rapidly conducted to the bubble, ensuring continuous vaporization during the expansion phase. For nanoscale bubbles and shorter time scales, the availability of this thermal energy is critical [71, 74].

In water, the high thermal diffusivity ($\mathrm{A} = 1.44 \times 10^{-7}\ \mathrm{m^2/s}$) ensures that the thermal energy stored in the overheated layer is kinetically available during the rapid expansion. As the bubble grows, its internal energy is consumed in vaporization and surface energy formation. Eventually, the bubble reaches its maximum radius when the energy balance shifts. At this stage, rapid cooling of the thinned overheated liquid layer occurs due to efficient heat conduction to the surrounding cold liquid. This cooling not only halts bubble growth but also triggers condensation of the vapor within the bubble [71]. Surface tension and the reduced

thermal energy at the bubble interface cause vapor condensation, leading to bubble shrinkage. It has been reported that for distributed arrays of microheaters, or for isolated microstructures, where the heat source is intermittent or insufficient to reheat the surrounding liquid, the bubble may either collapse entirely or enter a damped oscillatory regime [71, 74]. In contrast, when continuous structures are heated with focused laser beams, a sustained oscillatory behaviour can occur, persisting as long as the heating laser remains active [69]. Under these conditions, the boiling does not transition into the film boiling region, thereby preventing a boiling crisis. Similar to other boiling regimes at the microscale, such as explosive boiling in the transient phase or film and diffuse boiling in the steady phase, the oscillatory boiling regime is also influenced by the structure of the heater and the concentration of dissolved gases in the water. It is well established that an oscillating bubble, even in undersaturated liquids, can accumulate non-condensable gases due to gas diffusion, causing gradual growth [146].

Recent studies have advanced our understanding of oscillatory boiling around optothermal heaters. One of the most detailed investigations was conducted by Li et al. in 2019 [69]. Their work focused on oscillatory boiling induced by heating a continuous gold film with a focused laser beam (15 μm in diameter) in air-equilibrated water. They observed that reducing the laser focal spot size, and thus the heated area, eventually resulted in sustained oscillations of the bubble after an initial vapor explosion. According to their findings, oscillations did not occur for larger bubbles, and the oscillation frequency increased as the bubble size decreased. This suggests that sustained oscillations are primarily associated with bubbles composed mostly of vapor. As non-condensable gases diffuse into the bubble, causing it to grow, the oscillations are gradually damped (this phenomenon is discussed in more detail later in this section). These findings were further validated in a subsequent study by Namura, which investigated the impact of non-condensable gases on the occurrence and oscillation frequency of optically induced bubbles on a β-$FeSi_2$ film [77]. Li and colleagues considered the initial giant explosion to be the first phase of oscillation rather than a separate boiling regime [69]. Additionally, they observed a stream of pinched-off gas bubbles above the oscillating bubble (Figure 3.10). These detached microbubbles, which rose upward without shrinking or condensing back into the liquid, were determined to consist primarily of non-condensable gases. This degassing process helps stabilize the oscillating bubble, as it continuously removes non-condensable gases. Therefore, as long as the streaming of microbubbles persists and the main vapor bubble remains degassed, stable oscillations can be maintained despite gas diffusion [69]. A natural question arises: why and how does the streaming of these microbubbles eventually stop? To address

this, one must consider the forces acting on the bubble, a topic explored in the following section.

Another notable observation was the strong flows around the oscillating bubbles. One possible origin of these flows is Marangoni flow, a thermocapillary-induced flow along the bubble surface, which is discussed in greater detail in Chapter IV. Additionally, bubbles in contact with a surface and undergoing volume oscillations can generate streaming flows [147]. Although oscillation-induced flow profiles can closely resemble thermocapillary flow patterns, Li et al. reported that the violent and rapid inertial collapses observed in their system were too large for the small-amplitude approximation typically used to model oscillation-induced streaming flows. For this reason, they excluded oscillation-induced mechanisms when modelling flow profiles.

Interestingly, their simulations of thermocapillary flow around a stationary bubble (non-oscillating) with a diameter of 17 µm matched their experimental flow profiles reasonably well. However, the experimental flow amplitude was five times greater than the simulated values. This discrepancy may arise from the nonlinear advection term in the Navier-Stokes equation, which could result in streaming flow solutions responsible for mass and energy transport around oscillating bubbles [148].

Finally, Li and colleagues reported enhanced heat transfer around oscillating bubbles, likely due to two factors: the ejection of hot gas microbubbles into the bulk liquid and the contribution of rapid thermocapillary flows. In conventional nucleate boiling, heat transfer relies primarily on buoyancy to move hot liquid from the heated surface to the upper liquid region. In contrast, oscillatory boiling benefits from the additional support of thermocapillary flows, significantly improving heat transfer efficiency. Their study demonstrated that the rate of temperature increase (dT/dt) in the liquid was three times faster in the presence of oscillatory boiling bubbles compared to non-oscillating but growing bubbles [69]. The damping oscillatory phase of boiling has been observed around metallic films or arrays of microstructures, with lifetimes on the order of tens of milliseconds [71, 75, 76].

In summary, the nucleation and growth of optically induced bubbles follow a series of distinct yet interconnected stages, each governed by specific heat transfer mechanisms. The process begins with a delay phase during which thermal energy is gradually stored in the system. In

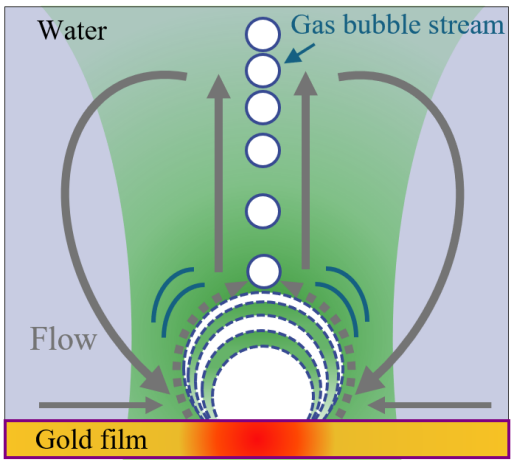

Figure 3.10 The flow profile, and the gas bubble stream around an oscillating bubble.

this stage, heat is transferred primarily through conduction and, a weak natural convection with the energy accumulating in the liquid and the heater until the nucleation temperature is reached.

Once the nucleation temperature is achieved, an explosive nucleation event occurs, marked by the rapid and violent formation of a giant, short-lived bubble. During this phase, heat transfer is dominated by direct thermal conduction from the overheated liquid layer into the surrounding cooler liquid. Simultaneously, vapor condensation at the bubble interface plays a critical role in dissipating energy.

Following nucleation, the system transitions into an oscillatory boiling regime. In this phase, the bubble undergoes sustained oscillations, driven by periodic expansions and contractions. Enhanced thermocapillary convection, arising from surface tension gradients induced by temperature differences along the bubble interface, becomes the dominant heat transfer mechanism. This convective flow efficiently transports heat from the bubble interface to the surrounding liquid, supporting the oscillatory behaviour.

As the bubble continues to grow and stabilize, the system moves into a phase resembling film boiling (or Leidenfrost boiling), where a thin vapor layer forms between the heater and the surrounding liquid. Heat transfer during this stage occurs primarily through conduction across the vapor layer, which acts as a thermal barrier, slowing down the heat transfer process.

In the final stage of bubble growth, the bubble transitions to a gas diffusion-dominated regime. Here, the gradual diffusion of non-condensable gases, such as dissolved air, into the bubble governs its growth. As more gas diffuses into the bubble, both conductive heat transfer and thermocapillary convection diminish. As mentioned before, it has been shown that this stage is eliminated in isolated structures [44].

This progression highlights the intricate and dynamic nature of bubble nucleation and growth around optothermal heaters. More importantly, it underscores the time-dependent behaviour of flow and heat transfer mechanisms around optically induced bubbles. Consequently, modulating the heating laser and adjusting the heating duration within the timescales of these regimes can provide a powerful tool for enhancing flow dynamics or heat transfer efficiency at the microscale. However, achieving such high modulation frequencies requires the bubble to shrink and collapse rapidly. In the next section, we will examine the mechanisms underlying bubble shrinkage and the parameters that influence its timescale.

3.3.2. Bubble shrinkage and collapse

The shrinkage of bubbles formed during optothermal heating can generally be divided into two distinct phases: the condensation-dominated phase and the diffusion-dominated phase. These phases are governed by different physical mechanisms and timescales, which depend on the size of the bubble, the surrounding medium, and the bubble composition right before turning of the laser.

In the initial stage of bubble shrinkage, the dominant mechanism is condensation of vapor at the bubble interface. This phase occurs immediately after the bubble detaches from the optothermal heater or the heat source is reduced. The condensation process is driven by the temperature difference between the bubble interface and the surrounding liquid. The characteristic time of bubble shrinkage during condensation can be described by [130]:

$$\Delta t_{cond} = \frac{\pi R_0^2}{4 Ja^2 D_l} \qquad 3\text{-}3$$

where $R_0(m)$ is the bubble initial radius, $D_l(m^2/s) = \frac{k_l}{\rho_l c_{pl}}$ is the liquid diffusivity, in which k_l is the liquid thermal conductivity, ρ_l is the liquid density, and c_{pl} is the liquid specific heat at constant pressure, and Ja is the Jakob number which is defined as [130]:

$$Ja = \frac{\rho_l c_{pl} |T_\infty - T_s|}{\rho_v L} \quad 3\text{-}4$$

where ρ_v is the vapour density, $T_\infty(°C)$ is the ambient temperature, $T_s(°C)$ is the saturation temperature, and $L(kJ/kg)$ is the Latent heat of vaporization. The Jakob number is one of the most important parameters for the physics of vapor bubbles as it accounts for the ratio between the available heat stored in the liquid and the latent heat. A higher Jakob number indicates stronger condensation due to a larger temperature gradient or lower latent heat.

The condensation-dominated phase is typically short-lived, lasting on the order of tens of microseconds to a few milliseconds, depending on the initial bubble size and the thermal properties of the liquid. The condensation time is proportional to R_0^2, indicating that larger vapor bubbles require more time to fully condense. However, experimental observations report that larger vapor bubbles shrink faster during this phase. This behaviour can be attributed to the steeper temperature gradients experienced by larger bubbles, which drive rapid condensation [73].

Once the bubble and the surrounding liquid have significantly cooled and most of the vapor has condensed, the shrinkage process transitions to the diffusion-dominated phase. In this stage, the primary mechanism is the diffusion of non-condensable gases (e.g., air) from the bubble interior into the homogenous surrounding liquid. This phase progresses much more slowly than the condensation phase and can be estimated using the following expression [149]:

$$\Delta t_{diff} = \frac{H R_{condensed}^2}{3 N_A k_B T d_{gl} \Upsilon} (1 + \Upsilon) \quad 3\text{-}5$$

where $H = c_g/P_g$ $(Pa \cdot m^3/mol)$ is the Henry law volatility constant in which c_g is the concentration of a gas in the aqueous phase, and P_g is the partial pressure of that gas under equilibrium conditions, $R_{condensed}(m)$ is the radius of the bubble after condensation, N_A is the Avogadro's constant, $k_B(J/K)$ is the Boltzmann constant, $T(°C)$ is the homogenous temperature

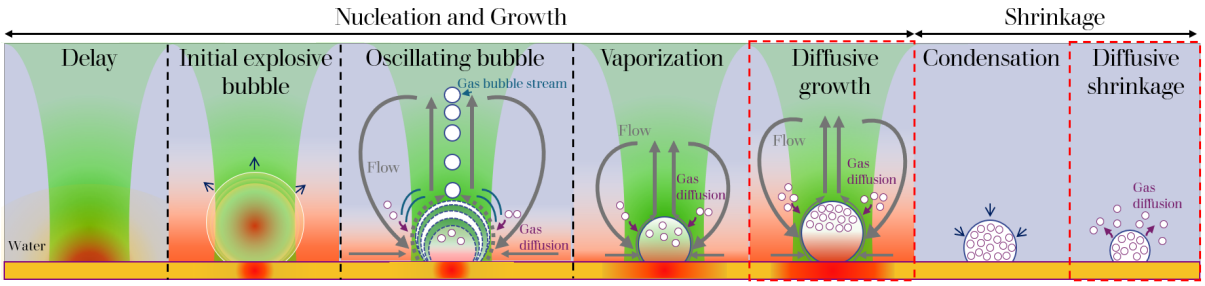

Figure 3.11 Overview of the life cycle of optically induced bubbles. The diffusive stages during both growth and shrinkage (highlighted by red dashed boxes) are suppressed when using isolated heat sources or degassed water.

of the system (bubble and surrounding liquid), $d_{gl}(\mathrm{m}^2/\mathrm{s})$ is the mass diffusivity of gas in the liquid, and Υ is the dimensionless ratio of Laplace pressure to ambient pressure, defined as:

$$\Upsilon = \frac{2\gamma}{\mathrm{R_{condensed}P_{amb}}} \tag{3-6}$$

Depending on the bubble size, two limiting regimes of Eq. 3-5 can be identified:

$$\text{Large bubbles } (\Upsilon \ll 1)\text{: } \Delta \mathrm{t_{diff}} \approx \frac{\mathrm{HP_{amb}}}{6N_A k_B \mathrm{T} d_{gl} \gamma} \mathrm{R_{condensed}^3} \tag{3-7}$$

$$\text{Small bubbles } (\Upsilon \gg 1)\text{: } \Delta \mathrm{t_{diff}} \approx \frac{\mathrm{H}}{3N_A k_B \mathrm{T} d_{gl}} \mathrm{R_{condensed}^2} \tag{3-8}$$

These equations highlight the strong dependence of diffusive shrinkage time on the bubble size. For large bubbles, the shrinkage time scales with $\mathrm{R_{condensed}^3}$, implying that the dissipation process can be extremely slow, often requiring hundreds to thousands of seconds for complete dissipation. Conversely, for small bubbles, the shrinkage time scales with $\mathrm{R_{condensed}^2}$, making the dissipation significantly faster. Small bubbles generated using isolated heat sources have been shown to dissipate within timescales ranging from microseconds to milliseconds, depending on the size of the plasmonic structure. This rapid dissipation enables the use of high modulation frequencies for the heat source, making it possible to achieve precise thermal control around these bubbles.

Figure 3.11 illustrates the general life cycle of optically induced bubbles, highlighting the distinct condensation and diffusion-dominated phases.

In the preceding section, we assumed that the bubble, whether oscillating or stationary, remains attached to the heater surface throughout the heating period. But what determines this behavior? What forces dictate whether a bubble detaches and rises or stays adhered to the surface? Can the bubble respond to and follow the flow induced around it? In the following section, we will analyze the forces acting on a bubble and examine the dynamics of its motion.

Since in our studies we have only done experiments in water, the words water, liquid and fluid have been used interchangeably in meany parts of this thesis. However, most of the discussions are valid in any other liquid as well.

3.4 Forces acting on a bubble and bubble motion

In this section, we examine the key forces that influence the motion of microbubbles, including buoyancy, added-mass force, Stokes' drag, and the Marangoni force [75, 150-152].

Buoyancy force

An arbitrary shaped body immersed in water, either partially or fully, will experience a net positive vertical force in the z direction, as shown in Figure 3.12, originating from the hydrostatic pressure in the water. This vertical force is called buoyancy and is equal in magnitude to the weight of the displaced water. This is known as the Archimedes' Principle. The hydrostatic pressure, P_s is the pressure exerted by water on the body of an immersed object at the depth h, caused due to the force of gravity. It can be expressed as:

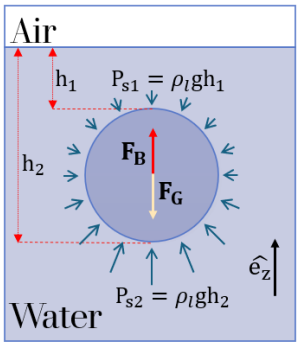

Figure 3.12 Gravity force and Buoyancy force caused by the hydrostatic pressure on a spherical bubble.

$$P_S = \rho_l g h \,. \qquad 3\text{-}9$$

For a spherical bubble immersed in water (as shown in Figure 3.12), the buoyancy force is obtained by integration of hydrostatic pressure over the bubble's surface:

$$\mathbf{F_B} = \int_{surface} P_s \, ds \, \hat{e_z} = \frac{4}{3}\pi R_b^3 \rho_l g \, \hat{e_z} \,, \qquad 3\text{-}10$$

where g is the gravitational acceleration, and R_b is the bubble radius. For the case of water, one need to keep in mind is that the density decreases linearly with an increasing temperature [150]:

$$\rho_l = \rho_{l0} - \beta\rho_{l0}(T - T_0), \qquad 3\text{-}11$$

where β is the thermal expansion coefficient, and ρ_{l0} is the liquid density at a reference temperature T_0. Therefore, in the presence of a temperature field, the density, and consequently the weight of the displaced water, will decrease with increasing water resulting in a reduction of the buoyancy force.

Gravity force

The gravity force can be simply calculated by the density of the bubble ρ_b, which can vary depending on its content and temperature, and its radius:

$$\mathbf{F_G} = -\frac{4}{3}\pi R_b^3 \rho_b g\, \hat{e_z}\,. \qquad 3\text{-}12$$

Stokes drag force

The Stokes' drag force, F_S, arises due to the dynamic viscosity of the water, μ. This force is important for moving bubbles (or any moving object), and it depends on the relative speed of the bubble to the surrounding liquid **v**. For the simple case of a spherical bubble (or any spherical object) with no-slip boundary condition on its surface the drag force can be obtained:

$$\mathbf{F_S} = -6\pi\mu R_b \mathbf{v}. \qquad 3\text{-}13$$

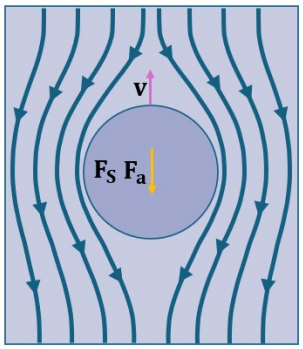

Figure 3.13 Stokes drag and added mass forces on a spherical bubble

Added mass force

If a bubble has a time-dependent velocity in fluid, an added mass force F_a is applied due to the motion of the nearby water. The added mass force was solved by Basset in 1888 and can be calculated as:

$$\mathbf{F_a} = -\frac{2}{3}\pi R_b^3 \rho_l \frac{d\mathbf{v}}{dt}. \qquad 3\text{-}14$$

As it can be observed equations 3-10 and 3-14 are very similar, and just the gravitational acceleration in 3-10 is replaced by the bubble acceleration in 3-14.

Marangoni force

The next force is the thermal Marangoni force, also known as the thermocapillary force. We have earlier mentioned the Marangoni force and flow on bubble surface but so far, we haven't gone through its details. Here we will describe the basics and explain the force that is exerted on the bubble due to the temperature gradient and later in Chapter IV we will discuss the flow. The surface tension of the water/vapor interface, γ (N/m), depends on the temperature, and can be approximated as:

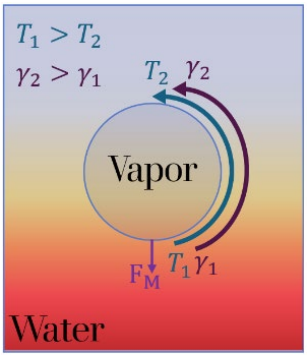

Figure 3.14
Marangoni force on a bubble in an unevenly distributed temperature field.

$$\gamma = \gamma_0 + \gamma_T(T - T_0). \qquad 3\text{-}15$$

Here γ_0 is is the surface tension at a reference temperature T_0, and γ_T $(N/m°C)$ is the surface tension coefficient[8]. The surface tension coefficient is usually negative[9] indicating that the surface tension decreases as temperature increases. This variation induces a tangential stress on the bubble surface, given by:

$$\nabla_t\gamma = \gamma_T \nabla_t T\,. \qquad 3\text{-}16$$

[8] Unfortunately, the terms 'surface tension' and 'surface tension coefficient' are often used interchangeably in the literature. In this thesis, we will strictly differentiate between the two. Surface tension (γ $[N/m]$) refers to the force per unit length at the water/gas interface, caused by cohesive forces between water molecules. Surface tension coefficient (γ_T $[N/m°C]$) refers to the rate at which surface tension changes with temperature at the water/gas interface.

[9] In some references Equ. 3-15 is written in the form of $\gamma = \gamma_0 - \gamma_T(T - T_0)$. In that case γ_T should be considered as a positive number for water and most of the other liquids.

This sheer stress generates a force, F_{sheer}, per unit area on the bubble surface. The total force for a spherical bubble experiencing a temperature gradient in the *z* direction (as indicated in Figure 3.14) can be obtained by integrating the tangential stress over the surface of the bubble, which yields:

$$\mathbf{F_M} = 2\pi R_b^2 \frac{d\gamma}{dT}\frac{dT}{dz}. \qquad 3\text{-}17$$

One can replace the $\frac{d\gamma}{dT}$ with γ_T in Eq. 3-17 if we accept the linear relationship in 3-15. However experimental data showed that this relationship is not always linear, and therefore we will keep the formula as a derivative. Eq. 3-17 shows that the direction of the Marangoni force is in the opposite direction of the temperature gradient, therefore this force drives the bubble toward the location with a higher temperature.

So, the total force F_T acting on the microbubble is:

$$\mathbf{F_T} = \mathbf{F_B} + \mathbf{F_B} + \mathbf{F_S} + \mathbf{F_a} + \mathbf{F_M} \qquad 3\text{-}18$$

In addition to these forces, a bubble that is experiencing a temperature gradient can also induce a flow in the water surrounding it, which can transport the bubble. Moreover, it can experience optical forces in optical setups (we will discuss this in Chapter VI).

The sum of these forces and the interaction of the bubble with the flow indicates if a bubble will detach or remain on the substrate, or if it can experience any lateral movement.

For the case of streaming bubbles shown in Figure 3.10 Namura et al. showed that as the size of the streaming bubbles increase, the Marangoni force become dominant, therefore, streaming bubbles will get attracted to the heat source and merge with the oscillating bubble, and increase the amount of air in the oscillating bubble which will eventually damps the oscillation [75].

Chapter IV: Optofluidics

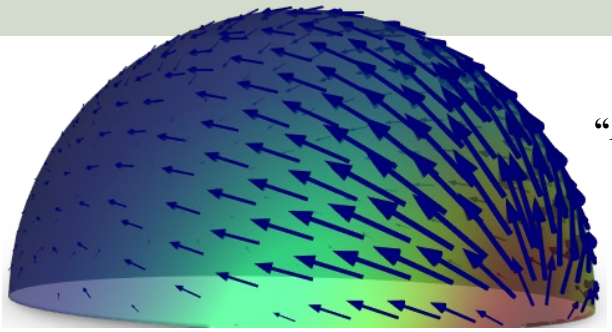

"Nature can produce complex structures even in simple situations, and can obey simple laws even in complex situations. Fluids frequently produce complex behavior, which can be either highly organized or chaotic. What is seen often depends on the size of the observer."

- Nigel Goldenfeld and Leo P. Kadanoff

In recent years, the phenomenon of soap bubbles freezing in cold environments has gained widespread attention on social media, with viral videos showcasing the intricate formation of ice crystals on their surfaces. This effect, known as the snow globe effect, sparked scientific interest in understanding the underlying mechanisms governing the freezing dynamics of thin liquid films.

In 2020, Ahmadi et al. systematically investigated this process in their study "How soap bubbles freeze," demonstrating that the observed swirling patterns and asymmetric freezing fronts are governed by the thermocapillary Marangoni flow [85].

Marangoni flow is an interface liquid flow from the areas of lower to higher values of surface tension. The necessary condition for occurrence of the Marangoni effect is therefore a presence of surface tension gradient at a given liquid–gas or liquid–liquid interface. Generally, these gradients can arise either via change in solute concentration, surfactant concentration at a free liquid surface, or via generation of temperature gradients.

In the snow globe effect, as a soap bubble freezes, the latent heat released during solidification causes localized temperature variations along its surface. Since the lower portion of the bubble

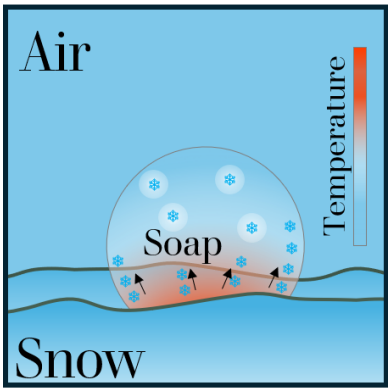

Figure 4.1 The flow profile, and temperature gradient on a soap bubble freezing on snow.

remains slightly warmer due to the latent heat release, a temperature gradient is established between the top and bottom regions of the bubble. Given that surface tension decreases with increasing temperature, this gradient induces a surface tension-driven flow, from warmer region on the bottom to cooler region on the top, redistributing the remaining liquid film and affecting the growth dynamics of ice crystals (Figure 4.1).

Consequently, rather than freezing uniformly, the bubble exhibits complex swirling motions that delay solidification in certain regions, leading to the characteristic patterns observed in experimental and natural settings. It's so fascinating how a simple system such as a freezing soap bubble on snow can produce such complex fluid behavior.

These thermocapillary flows provide an excellent analogy for optofluidic systems, where optical heating can generate controlled temperature and surface tension gradients, thereby inducing precise fluid motion at the microscale and nanoscale.

The goal of this chapter is to delve into the world of thermocapillary Marangoni flows induced by laser irradiation. First, we begin by studying the surface tension, then we will explore the induced flow due to the surface tension gradient and finally we will briefly discuss different methods for controlling the flow direction with light.

4.1. Surface tension

Surface tension is a fundamental property of liquid interfaces, defined in terms of force as the force per unit length in unit [N/m] acting along the surface of a liquid at the interface between two phases (e.g., liquid-gas or liquid-liquid). This force acts tangentially to the liquid surface and tends to minimize the surface area due to cohesive molecular interactions [153].

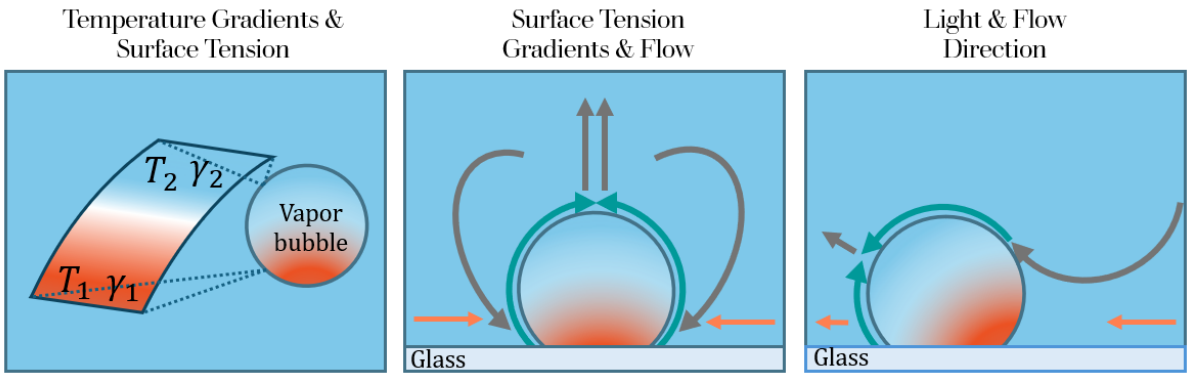

Figure 4.2 Outline of Chapter IV.

Inside the liquid volume, cohesive forces between molecules are nearly equal in all directions, effectively canceling each other out. However, at the liquid-air or liquid-liquid interface, molecules experience an asymmetric force distribution, with stronger cohesive forces from the liquid side and weaker adhesive interactions with the surrounding medium. This imbalance creates a contractile force along the surface, driving the liquid to minimize its surface area.

Since van der Waals forces, which govern the cohesive and adhesive interactions in liquids, weaken with increasing temperature, surface tension also decreases with rising temperature. This temperature dependence is often approximated as a linear relation, as shown in Eq. 3-15. However, in reality, the presence of additional intermolecular interactions—such as Coulomb interactions, dipole-dipole forces, hydrogen bonding, charge transfer (CT), magnetic forces, metallic bonding, or other self-organizing molecular interactions—can lead to deviations from this linear trend. Depending on the specific system, some of these interactions may be negligible, while others may play a dominant role in determining surface tension [154].

To accurately describe surface tension at free surfaces or interfaces between multiple phases, one may instead rely on experimentally measured and fitted expressions. In our simulations, we have used the following quadratic relation, implemented in the commercial FEM solver COMSOL Multiphysics. This expression was obtained from references [153]:

$$\gamma = -2.3 \times 10^{-7} \times T^2 - 1.63 \times 10^{-5} \times T + 9.77 \times 10^{-2}\,. \qquad 4\text{-}1$$

Figure 4.3 shows the value of water/air surface tension obtained from Eq. 4-1 compared to the one experimentally measured from ref [155].

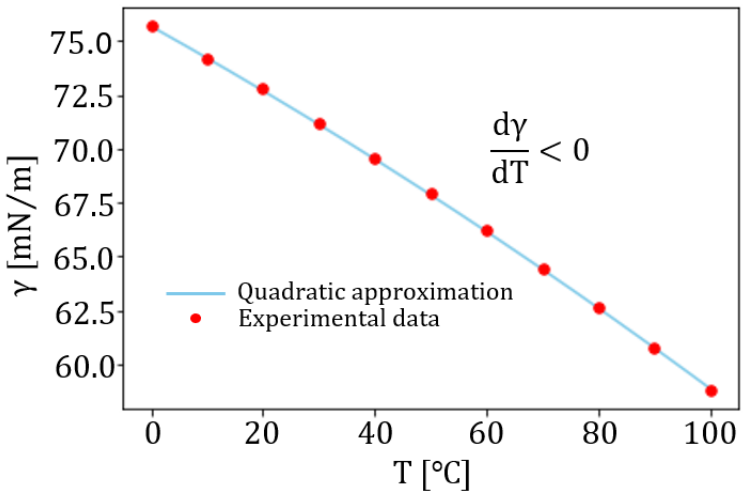

Figure 4.3 Quadratic approximation and experimentally measurement of the surface tension versus temperature for water in contact with air.

4.2. The Navier-Stokes equation and Marangoni Flow

Fluid motion is governed by Navier-Stokes equations that describe conservation of momentum by Newton's second law of motion for fluids. In simpler words, Navier-Stokes equations relate the temporal and spatial change of the fluid velocity field to the sheer and normal stresses and the body forces. The only body force in the absence of electrical and magnetic fields is gravity which results in the buoyancy driven flow or natural convection.

The buoyancy driven flow is generated due to the decreasing of the fluid density with increasing temperature. As mentioned previously in most liquids the density decreases linearly with increasing temperature, and their relationship is given by Eq. 3-11. Thus, the heated fluid will rise into the cooler region and the cooler fluid from the surroundings will flow into the heated region.

The velocity of buoyancy or surface tension driven flows is usually small; therefore, the fluid motion can be described by the Boussinesq approximation[10] of the Navier-Stokes equations. If we assume a homogeneous gravity field in the z direction $\mathbf{g} = -g\hat{e_z}$, we can write the Navier-Stokes equation as [154]:

[10] According to the Boussinesq approximation density differences can be ignored except where they appear in terms multiplied by g, the acceleration due to gravity.

$$\frac{\partial \mathbf{u}}{\partial \mathrm{t}} + (\mathbf{u} \cdot \boldsymbol{\nabla})\mathbf{u} = -\frac{1}{\rho_{l0}}\boldsymbol{\nabla}\mathrm{p} + \boldsymbol{\nabla} \cdot (\nu[(\boldsymbol{\nabla}\mathbf{u}) + (\boldsymbol{\nabla}\mathbf{u})^{\boldsymbol{T}}] - \frac{2}{3}\nu(\boldsymbol{\nabla} \cdot \mathbf{u})\mathbf{I}) + \frac{\rho_l}{\rho_{l0}}\mathrm{g}\hat{\mathrm{e}}_{\mathrm{z}} \,. \qquad 4\text{-}2$$

Here, p is the fluid pressure, ν is the kinematic viscosity and is equal to dynamic viscosity μ, divided by ρ_{l0}, **I** is the unitary tensor, and the superscript $\boldsymbol{T}$ connected to the velocity gradient describes a component tangential to the surface. The term on the left-hand side of Eq. 4-2 corresponds to inertial forces, then the first term on the right-hand side represents pressure forces, second, viscous forces, and the last, external forces applied to the fluid. These equations are solved together with the continuity equation representing conservation of mass:

$$\frac{\partial \rho}{\partial \mathrm{t}} + \boldsymbol{\nabla} \cdot (\rho \mathbf{u}) = 0 \,. \qquad 4\text{-}3$$

Since water is incompressible, the continuity equation simply yields:

$$\boldsymbol{\nabla} \cdot \mathbf{u} = 0 \,. \qquad 4\text{-}4$$

This will further simplify Eq. 4-2 to:

$$\frac{\partial \mathbf{u}}{\partial \mathrm{t}} + (\mathbf{u} \cdot \boldsymbol{\nabla})\mathbf{u} = -\frac{1}{\rho_{l0}}\boldsymbol{\nabla}\mathrm{p} + \nu\boldsymbol{\nabla}^{\boldsymbol{2}}\mathbf{u}\boldsymbol{\nabla} + \frac{\rho_l}{\rho_{l0}}\mathrm{g}\hat{\mathrm{e}}_{\mathrm{z}} \,. \qquad 4\text{-}5$$

Eq. 4-5 can be even more simplified if we are in the laminar flow regime. Laminar flow is characterized by smooth, parallel layers of fluid that move in an orderly fashion without significant mixing or turbulence, and it occurs at low Reynolds numbers, where the viscous forces are dominant, and inertial forces can be neglected. Reynold number can be defined as:

$$\mathrm{Re} = \frac{u\mathrm{L}}{\nu}, \qquad 4\text{-}6$$

where L is a characteristic length. The threshold for "low" vs "high" Reynolds number varies for different situations/geometries. For the case of a sphere moving through a fluid, a threshold of Re ≤ 1 is often valid. This means as long as the fluid velocity is smaller than $\frac{\nu}{L}$. which for water in micrometre scale $\frac{\nu}{L}$ is approximately equal to 1 m/s, we can apply the Laminar flow approximation. In this case the inertial (convective) term can be omitted ($(\mathbf{u}\cdot\boldsymbol{\nabla})\mathbf{u}\approx\mathbf{0}$).

The final simplification in our flow simulations is by considering the steady state flow, in this case the term $\frac{\partial \mathbf{u}}{\partial t}$ also equal to 0 and the Navier-Stokes equation can be written as:

$$-\frac{1}{\rho_{l0}}\boldsymbol{\nabla}p+\nu\boldsymbol{\nabla}^{\mathbf{2}}\mathbf{u}\boldsymbol{\nabla}+\frac{\rho_l}{\rho_{l0}}g\hat{e_z}=0\,. \qquad 4\text{-}7$$

In contrast to body forces, surface tension- on the other hand- only acts on the free surface of the fluid and hence appears only in boundary conditions which aim to balance normal and tangential stresses on the free surface. The stress balance equation at the liquid-gas interface can be written as:

$$\hat{n}\cdot\bar{\bar{\boldsymbol{\tau}}}=\gamma(\boldsymbol{\nabla}_{\mathbf{t}}\cdot\hat{n})\hat{n}-\boldsymbol{\nabla}_{\mathbf{t}}\gamma\,, \qquad 4\text{-}8$$

where $\hat{n}$ is the unit normal vector which is directed out of gas (vapor) and into the ambient fluid (shown in Figure 4.4), and $\bar{\bar{\boldsymbol{\tau}}}$ is the stress tensor and it is equal to:

$$\bar{\bar{\boldsymbol{\tau}}}=[-p\mathbf{I}+\mu(\boldsymbol{\nabla}\mathbf{u}+(\boldsymbol{\nabla}\mathbf{u})^{T})]\,. \qquad 4\text{-}9$$

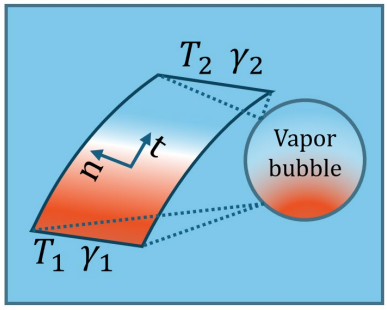

Figure 4.4 Normal and tangential unit vectors on a fluid surface element.

Equation 4-8 equates the fluid stress tensor to the surface tension forces (right-hand side). Now, if we take the dot product of 4.8 with $\hat{n}$ (shown in Figure 4.4), the boundary condition can be written as [156]:

$$\hat{n} \cdot \bar{\bar{\tau}} \cdot \hat{n} = \gamma(\nabla_t \cdot \hat{n}) \,. \tag{4-10}$$

This boundary condition states that the normal component of the fluid stress tensor must balance with the portion of the surface tension due to curvature. This equation is called the Laplace equation in the absence of viscosity.

On the other hand, if we take the dot product of 4.8 with $\hat{t}$ (shown in Figure 4.4), the unit tangential vector (shown in Figure 4.4), the boundary condition can be written as:

$$\hat{n} \cdot \bar{\bar{\tau}} \cdot \hat{t} = -\nabla_t \gamma \cdot \hat{t}. \tag{4-11}$$

This boundary condition states that the tangential component of the fluid stress tensor must balance the tangential portion of the surface tension gradient. This will result in a tangential (surface) flow in the opposite direction of the surface tension gradient which is the Marangoni flow.

In summary, the governing equations for our FEM simulations include the conservation of momentum (Eq. 4-7), conservation of mass (Eq. 4-4), and conservation of energy (Eq. 2-34), along with the stress balance boundary conditions (equations 4-10 and 4-11). Additionally, no-slip and no-penetration boundary conditions are imposed on solid surfaces, while a room

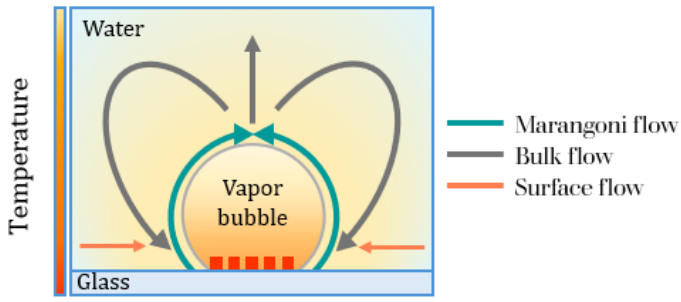

Figure 4.5 Expected Marangoni flow induced by a single bubble with a temperature gradient normal to the substrate surface.

temperature boundary condition is applied at the edge of the simulation domain. These conditions define the framework for our simulations of flow and heat transfer.

The simulation methods are described in greater detail in Chapter V; however, some preliminary results that represent our experiments are presented here for demonstration purposes.

4.3. Controlling flow with light

At this point, we have established that the induced flow pattern created by the Marangoni effect is proportional to the tangential derivative of the temperature along the air/water (bubble) interface. This implies that for a single bubble positioned on a warm substrate, analogous to freezing soap bubbles on snow, as illustrated in Figure 4.1, the flow on the bubble's surface will move from the bottom to the top.

Now, considering a vapor bubble attached to a submerged hot substrate in water, the Marangoni flow along the bubble surface will generate two symmetrical vortices in the bulk, ultimately inducing a flow on the substrate surface directed towards the heat source, as illustrated in Figure 4.5. This induced flow at the water/substrate interface is particularly significant because, due to the no-slip boundary condition, we expect the velocity near the surface to be close to zero.

Based on this understanding, one straightforward approach to controlling the flow near the substrate is to manipulate the temperature gradient on the bubble's surface.

In our system, consisting of a bubble nucleated on an isolated array of nano-heaters, as described in Chapters II and III, this can be achieved by introducing a secondary array adjacent

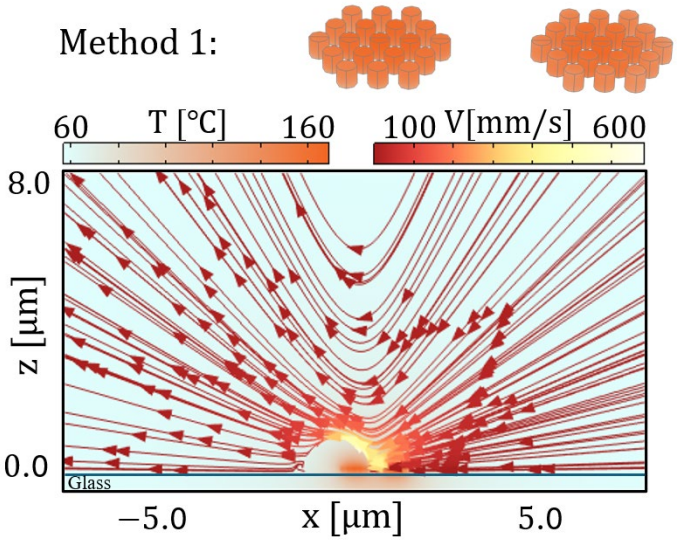

Figure 4.6 Induced directional flow using Method 1. The flow profile is around a pair of symmetric arrays with edge-to-edge distance of 400 nm. Each consists of 19 a-Si nanodisks with a diameter and height of 100 nm. A Gaussian beam with a beam waist radius of 11 μm and a wavelength of 532 nm is considered to be focused on the center of the left array. The effect of the vapor nucleation on the absorption cross section and the consequence of heat generation of the right array is considered. The color of the arrays plotted on top indicates their temperature.

to the primary array. By breaking the lateral symmetry of the temperature profile through adjustments such as shifting the laser focal point, modifying the array size, altering the absorption cross-section of the nanostructures, or a combination of these methods, we can control the flow direction effectively.

Method 1: Controlling flow via laser focal point position

The irradiance of the Gaussian laser beam used for heating the nanostructures at its focal plane can be expressed as:

$$I(r) = \frac{2P_{laser}}{\pi w_0^2} \exp\left(\frac{-2r^2}{w_0^2}\right), \qquad 4\text{-}12$$

where P_{laser} is the total laser power, w_0 is the beam waste radius and r is the radial distance from the center axis of the beam.

As discussed in Chapter 2, the power delivered by the nanostructures into the system, $q(r)$, is approximately linearly dependent on the heating laser irradiance. Consequently, as the nanostructure moves farther from the laser's focal point, their delivered heating power decreases. This allows us to generate an in-plane temperature gradient by positioning two symmetrical arrays at an edge-to-edge distance d and focusing the laser on the center of one of the arrays. Due to the system's geometry, we can dynamically control the flow by altering the laser's focal spot position. This method enables us to achieve three distinct flow patterns:

1. Directional flow to the left: When the laser is focused on the left array.

Figure 4.6 illustrates an FEM simulation of two arrays of a-Si nanodisks with an edge-to-edge distance of 400 nm. Each array consists of 19 nanodisks with a diameter and height of 100 nm. A Gaussian beam with a beam waist radius of 11 μm and a wavelength of 532 nm is focused on the center of the left array. A vapor bubble forms above the left array, while the right array only heats the surrounding medium, creating an in-plane temperature gradient on the bubble that induces a directional flow to the left.

2. Directional flow to the right: when the laser is focused on the right array, the mechanism is the same as the previous one in the opposite direction.

3. Symmetric flow toward the arrays: (similar to the single array flow) When the laser is focused at the midpoint between the two arrays, a bubble nucleates with its center aligned with the center of the gap, restoring symmetry in the system. As a result, the surface flow is directed toward both arrays.

This method, which we utilized in Paper II for flow control, offers significant flexibility in generating different flow profiles. However, adjusting the laser position can be challenging, as it requires either mechanically moving the substrate or using external equipment such as a Spatial Light Modulator (SLM) (which will be explained in the methods section).

Method 2: Controlling flow via asymmetrical arrays

The excess temperature ΔT in a collection of nearby optically heated nanostructures increases rapidly with the number of such structures. This means that introducing asymmetry in the system by designing arrays with different sizes (i.e., different numbers of nanostructures) can

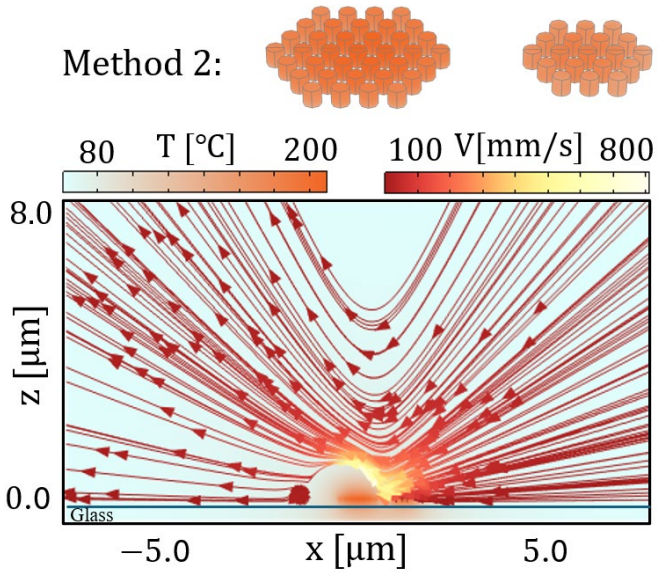

Figure 4.7 Induced directional flow using method 2. The flow profile is around a pair of asymmetric arrays with edge-to-edge distance of 400 nm. The left and right arrays consist of 37, and 19 a-Si nanodisks respectively. A plane wave with a wavelength of 532 nm is considered in the background. The effect of the vapor nucleation on the absorption cross section and the consequence heat generation of the left array is considered. The color of the arrays plotted on top indicates their temperature.

induce an in-plane temperature gradient even with uniform plane-wave illumination (constant irradiance across all positions).

An example of such a method is shown in Figure 4.7, which shows a FEM simulation of two asymmetric arrays of a-Si nanodisks with an edge-edge distance of 400nm. The left and right arrays consist of 37 and 19 nanodisks respectively with the same dimensions as before. In this simulation a plane wave with wavelength of 532 nm is considered, so that the only mechanism responsible for the directionality of the flow is the asymmetry of the arrays. A vapor bubble is considered on top of the left array whereas the right array is just heating the surroundings. This will result in an in-plane temperature gradient on the bubble which will indue a directional flow toward the left.

Although this method can generate strong directional flows due to the pronounced asymmetry, it lacks dynamic control. Nonetheless, its simplicity and independence from modifications in the heating laser make it a desirable approach when real-time flow direction adjustments are not needed. This method, in combination with Method 1, was implemented in both Paper I and Paper II.

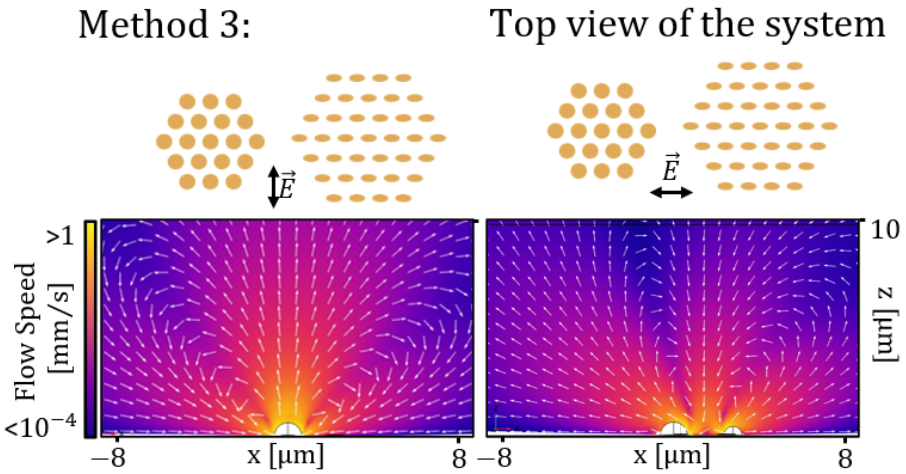

Figure 4.8 FEM simulations of Marangoni flows induced by perpendicular polarization which, results in a single bubble (left panel), and parallel polarization which results in two bubbles with opposing lateral temperature gradients (right panel). The flow profiles are around a pair of asymmetric arrays with edge-to-edge distance of 2 μm. The left and right arrays consist of 19, and 37 circular and ellipsoidal gold nanodisks respectively

Method 3: Controlling flow by modifying the absorption cross section of the structures

In this approach, arrays consist of nanostructures with differing optical properties, enabling dynamic flow control via light polarization. This method is particularly interesting because, as discussed in Chapter 2, elongated plasmonic nanostructures, such as ellipsoidal disks, exhibit polarization-dependent absorption, for a given wavelength, such as that of the heating laser. Thus, polarization can act as a switch to modulate in-plane temperature gradients and control the flow direction dynamically. However, designing nanostructures with a significant polarization-dependent absorption contrast is constrained by material properties and wavelength limitations.

In Paper I, we employed this method by using two arrays of gold nanostructures for polarization-dependent flow control. One array contained 19 circular nanodisks (100 nm diameter, 60 nm height), while the second array consisted of 37 ellipsoidal nanodisks (100 nm long axis, 50 nm short axis, 60 nm height), with an edge-to-edge distance of 2 μm. To maximize the absorption contrast between different polarizations, we used a 660 nm wavelength laser as the heating source.

In all of these three methods the temperature induced by the secondary heat source may be sufficient to vaporize the surrounding water, resulting in an additional bubble on the second

array. However, we have only observed this for our gold nanostructures. Figure 4.8 shows FEM simulations for two cases:

- Perpendicular polarization: Results in a single bubble.
- Parallel polarization: Generates two bubbles, causing a complete reversal of the flow pattern due to the formation of opposite in-plane temperature gradients on the surface of the two bubbles.

In the simulations presented here, the size and position of the bubbles were adjusted to reproduce the experimentally observed flow profiles. Our simulations indicate that to achieve flow profiles compatible with our experimental results, we need to shift the bubble in the direction of the flow. To experimentally demonstrate this effect, we used brightfield microscopy to capture video frames of bubble nucleation on an asymmetric pair of gold arrays consisting of 19 and 7 circular nanodisks respectively. To make sure that the bubble was visible, the power of the heating laser was increased to six times the nucleation threshold. This resulted in the nucleation of a bubble with a diameter exceeding 3 µm, which was observable using our brightfield microscope.

Figure 4.9 shows video frames captured over 0.5 seconds of illumination. As seen in the images, the bubble's center shifts to the left as it grows, aligning with the expected flow direction. This displacement further enhances the effect of the in-plane temperature gradient, as one side of the bubble moves closer to the heat source marked by an orange marker in Figure 4.9, amplifying the temperature difference across its surface. The reason for the bubble movement is not clear to us. The imbalance between any of the lateral components of the forces we discussed in the previous Chapter or the flow transport or even the optical forces can be the reason why the bubbles are shifted. However, in our simulations, we have always considered a shift in the direction of the induced flow to match the flow profiles observing in our experiments.

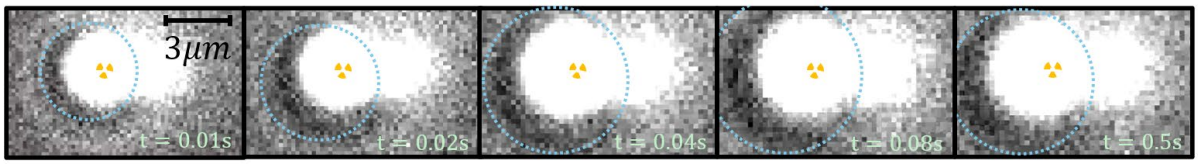

Figure 4.9 Displacement of a bubble in the direction of the flow. The blue circles indicate the change in position andsize of the bubble with time. The orange marker on the left marks the position of the primary array consisting of 19 circular nanodisks. On the right is a secondary array consisting of 7 circular nanodisks.

4.4 Thermophoresis

We have so far discussed two thermally induced flows: Natural convection and Marangoni flow. As the last part of this chapter, we will, for the sake of competence, discuss another thermally induced flow known as thermophoresis.

Thermophoresis (also called the Soret effect) is the drift of colloidal particles or molecules in a solution due to an external temperature gradient. The velocity of this thermodiffusive drift, $\mathbf{v_{td}}$, is proportional to the temperature gradient by the thermodiffusion coefficient, also known as thermophoretic mobility, D_T a [157]:

$$\mathbf{v_{td}} = -D_T \boldsymbol{\nabla} T(\mathbf{r}) \,. \qquad 4\text{-}13$$

Recent studies have revealed that the microscopic mechanisms underlying thermodiffusion are often highly complex and arise from a combination of different contributions [158, 159]. One of the most fundamental mechanisms driving thermophoresis is thermo-osmotic flow at the interface between the particle and the surrounding solvent [160]. This interfacial flow is induced by thermally driven inhomogeneities in the electric double layer surrounding the colloidal particle. The counterion cloud adjacent to the charged surface of the colloidal particle follows a Poisson-Boltzmann concentration distribution, which is temperature-dependent. As a result, a thermal gradient ($\boldsymbol{\nabla}$T), induces a corresponding concentration gradient of counterions across the particle surface, leading to an osmotic pressure imbalance ($\boldsymbol{\nabla} P_{osmotic}$ as illustrated in Figure 4.10 (a). This imbalance generates an interfacial fluid flow along the temperature gradient, directing liquid towards the hotter side of the colloidal particle. Consequently, the particle itself moves with the same velocity but in the opposite direction, against the temperature gradient, toward cooler regions (Figure 4.10(a)).

Another significant factor contributing to thermophoretic motion is the temperature-dependent density variation of most solvents [160]. As previously mentioned, the density of liquids generally decreases with increasing temperature. Also, in many solvents, van der Waals interactions are the dominant forces acting on colloidal particles. As a result, the particle experiences a stronger attraction to regions of higher liquid density, which typically correspond to cooler temperatures (Figure 4.10 (b)), and due to these stronger attractive forces on the colder side, the colloidal particle tends to migrate toward lower-temperature regions.

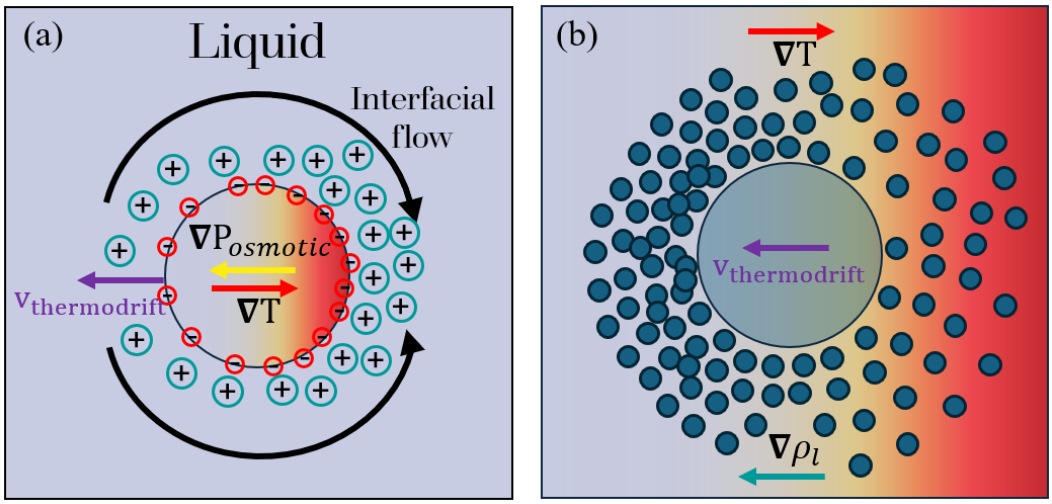

Figure 4.10 (a) Thermo-osmotic flows around a charged colloidal sphere cause the particle to drift in the opposite direction as the temperature gradient. (b) Density driven thermophoresis, where the particle is attracted toward the colder regions with higher densities due to larger van der Waals forces.

Regardless of the underlying mechanism and the microscopic details that are hidden in the thermophoresis, the balance of the thermodiffusive and diffusive current densities yields the steady state probability density distribution, $\varsigma(\mathbf{r})$, for finding an object at a certain position of the temperature field $T(\mathbf{r})$. The thermodiffusive current density, $\mathbf{J_{thermodrift}}$, is defined as $\varsigma(\mathbf{r})\mathbf{v_{thermodrift}}$, and the diffusive current density, $\mathbf{J_{drift}}$, is defined as $-D\boldsymbol{\nabla}\varsigma(\mathbf{r})$, where D is the diffusion coefficient. $\mathbf{J_{drift}}$ is due to the Brownian motion, which we will study further in Chapter V, and acts in the opposite direction of $\boldsymbol{\nabla}\varsigma(\mathbf{r})$. At steady state one can write [161]:

$$\mathbf{J_{thermodrift}} + \mathbf{J_{drift}} = -\varsigma(\mathbf{r})D_T\boldsymbol{\nabla}T(\mathbf{r}) - D\boldsymbol{\nabla}\varsigma(\mathbf{r}) = 0 \qquad 4\text{-}14$$

Thus, the steady state probability of density distribution is given by [162]:

$$\varsigma(\boldsymbol{r}) = \varsigma_0 \exp\left(\frac{D_T}{D}\boldsymbol{\nabla}T(\mathbf{r})\right) \qquad 4\text{-}15$$

The ratio between the thermophoretic mobility and the diffusion coefficient is known as the Soret coefficient ($S_T = \frac{D_T}{D}$). From the thermophoresis mechanisms described above, it seems that colloidal particles always move toward the colder regions, which corresponds to a positive thermophoretic mobility, D_T, and Soret coefficient, S_T. While this is most often the case,

controlling the properties of the solvent can result in the movement of the colloidal particles toward the warmer regions, which corresponds to a negative D_T, and S_T [163]. Therefore, Eq. 4-14 determines the extent of depletion or accumulation of particles that occur based on the sign of the Soret coefficient.

Chapter V: Methods

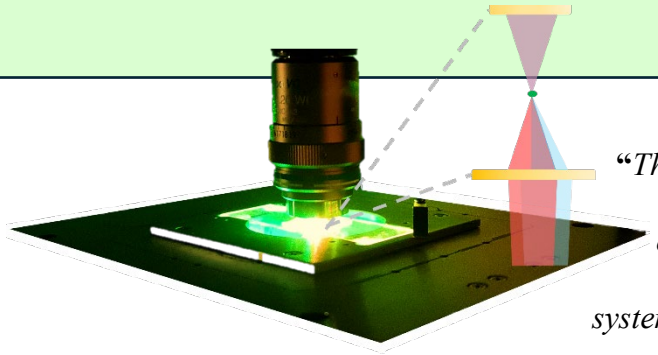

"The object of all science is to coordinate our experiences and bring them into a logical system."

- Albert Einstein

Albert Einstein once emphasized the importance of organizing our experiences into a logical system, an insight that encapsulates the essence of scientific research. At its core, research is the systematic transformation of observations and experiments into a coherent framework that advances our understanding of complex phenomena.

The process of developing a research project, from its initial conception to a finalized scientific article, involves a combination of numerical and experimental methodologies. Typically, an idea first undergoes theoretical exploration and numerical simulations to identify an optimal structure or design. Once an optimal configuration is established, the next step is its experimental realization using appropriate fabrication or synthesis techniques. This is followed by characterization and measurement to validate the underlying hypothesis, often through optical experiments but also potentially supplemented by additional simulations.

This chapter provides an overview of experimental methodologies and numerical simulations employed in this thesis.

5.1. FEM simulations for structure optimization

As mentioned in previous chapters, we have used FEM simulations for determining the structural parameters characterizing the nanoheaters we have used in our studies. Hopefully, by now readers have realized that we are interested in maximizing the absorption of our

nanostructures at the wavelength of the heating laser. To do so we have calculated and optimized our nanostructures using the Electromagnetic Waves, Frequency Domain (emd) interface in COMSOL Multiphysics. We have considered a spherical domain around our nanostructures with a diameter 15 times larger than the characteristic dimension of our nanoparticles. Also, we considered a Perfectly Match Layer with a thickness 4 times larger than the characteristic dimension of our nanoparticles at the outer shell of our spherical domain. The incident wave is considered as a background plane wave propagating in the z direction, and polarization of the incident light is determined based on the simulation. In general cases, x-polarized light is considered. For calculating the absorption cross sections, first, the total absorbed power was obtained by integrating the total power dissipation density, Q_h, over the volume of the nano structure, V:

$$P_{abs} = \int_V Q_h dV , \qquad 5–1$$

And the absorption cross section was calculated by:

$$\sigma_{sca} = \frac{P_{abs}}{I_{inc}} , \qquad 5–2$$

where I_{inc} is the time-averaged intensity of the incident plane wave in the surrounding medium.

For calculating the scattering cross sections, first the total scattered power was obtained by integrating the outward-averaged Poynting vector (time averaged power flow of the relative fields per unit area), P_{oav}, over the surface of an imaginary sphere with a radius 10 times larger than the characteristic dimension of our nanoparticles.

$$P_{sca} = \int_{surf} P_{oav} dS , \qquad 5–3$$

And the scattering cross section was then calculated by:

$$\sigma_{abs} = \frac{P_{sca}}{I_{inc}} , \qquad 5–4$$

By sweeping the dimensions of the nanostructures and calculating the absorption cross sections, optimal sizes were obtained considering the limitations and requirements of our systems. The absorption cross sections of the structures we used in our studies are already plotted in Chapter II. Later, we can use the absorption cross section for calculating the heat source density in our heat transfer and fluid flow calculations. It should be noted that if one couples the Electromagnetic Waves interface to the Heat Transfer and Fluid Flow interfaces,

which will be explained later, then there is no need of calculating the absorption cross section and the Q_h can be directly used as the spatial heat density of the nanostructures. Once the structures are designed and fabricated, we can use them to experimentally obtain the flow profile around them.

5.2. Flow Characterization

One of the methods that we have used for obtaining the flow profiles around an array of nanostructures is optical force microscopy. In this method, we have used a holographic optical tweezer for trapping and moving a probe particle into point of interest in three dimensions where the flow is measured, and then we have used a Quadrant Photo Diode (QPD) to measure the intensity distribution of the transmitted light from the probe particle to estimate the flow velocity. The details and physics behind these measurements are explained in this section.

5.2.1. Holographic optical tweezing

As its name suggests, optical tweezers use optical forces to tweeze an object. So, to realize how optical tweezers work, one must first understand what optical forces are. There are two main types of optical forces: the radiation pressure force and the gradient force [164].

The radiation pressure force simply acts to push particles in the direction of the incident light. On the other hand, the gradient force tends to pull a particle, with higher refractive index than the surroundings medium, into regions of higher light intensity. It is thus the basis for optical tweezers.

Typically, these forces are negligible when viewed from a macroscopic perspective. At the micro/nanoscale, however, these optical forces can be significant. The first demonstration of optical tweezers came in the 1970's when Arthur Ashkin first developed the [165, 166]. In the following we will have a brief overview of the underlying physics behind optical forces.

Radiation pressure force

In previous chapters, we have described light from a classical point of view as an electromagnetic wave, with the angular frequency, ω, and wavenumber k. However, light can

also be described quantum mechanically with the energy, E, and momentum, p, of photons. The energy of each photon is equal to $\hbar\omega$, and the magnitude of the momentum that each photon carries is equal to h/λ, where h is Plank constant.

It was first predicted by Maxwell and Bartoli in the 1870s that radiation pressure exists due to the momentum of light [167]. One specific example to illustrate this radiation pressure is the case of plane-wave light normally incident onto a flat, perfect mirror. The direction of the momentum that each photon carries is in the direction of light propagation. When the light gets reflected (not transmitted), the magnitude of the momentum remains the same, but its direction is reversed (Figure 5.1 (a)). This will result in a $2h/\lambda$ net change of momentum per photon. If the perfect mirror were replaced with a perfectly absorbing material, then the change in momentum would only be h/λ (Figure 5.1 (b)). In either case, to conserve momentum, this change in momentum carried by the light must be accounted for by a change in momentum of the mirror/absorber. If we know the rate of photons striking the surface, we can determine the force acting on the object.This force is called the radiation pressure force and acts to push particles in the direction of incident light [167].

In more general terms, phenomena such as scattering and absorption can stop the transmission of light. The total power not transmitted by the particle due to these phenomena must convey a force on the particle, in the direction of propagation. Its magnitude is calculated by [168, 169]:

$$|\mathbf{F_{radiation}}| = \frac{n_m}{c_0} P_{extinct}, \qquad 5\text{–}5$$

in which, n_m is the refractive index of the medium and $P_{extinct}$ is the total power lost due to the extinction of transmitted light:

$$P_{extinct} = P_{sca} + P_{abs} = (\sigma_{\mathrm{sca}} + \sigma_{\mathrm{abs}})\mathrm{I_{inc}}, \qquad 5\text{–}6$$

where, $\mathrm{I_{inc}}$ is the intensity of incident light, and σ_{sca} and σ_{abs} were defined in Chapter II.

Gradient force

The gradient force is the main force in optical tweezing, and it pulls particles into regions of higher light intensity [170]. Once more we will start our analysis with sub-wavelength particles in the quasi-static (Rayleigh) approximation. Such a particle experiences a Lorentz force in

response to the dipole moment induced by the incident electric field **E**. In terms of the polarizability, using Eq. 2-20, the force can be written as [171, 172]:

$$\mathbf{F_{Lorentz}} = (\boldsymbol{\mathcal{P}} \cdot \nabla)\,\mathbf{E} + \frac{\mathrm{d}\boldsymbol{\mathcal{P}}}{\mathrm{dt}} \times \mathbf{B} = \epsilon_0 \epsilon_\mathrm{m} \alpha \left((\mathbf{E} \cdot \nabla)\mathbf{E} + \frac{\partial \mathbf{E}}{\partial \mathrm{t}} \times \mathbf{B} \right), \qquad 5\text{–}7$$

where **B** is the magnetic field. By using the vector identity $\nabla(\mathbf{A_1} \cdot \mathbf{A_2}) = \mathbf{A_1} \times (\nabla \times \mathbf{A_2}) + \mathbf{A_2} \times (\nabla \times \mathbf{A_1}) + (\mathbf{A_1} \cdot \nabla)\mathbf{A_2} + (\mathbf{A_2} \cdot \nabla)\mathbf{A_1}$ with $\mathbf{A_1} = \mathbf{A_2} = \mathbf{E}$, :

$$(\mathbf{E} \cdot \nabla)\mathbf{E} = \frac{1}{2}\nabla|\mathbf{E}|^2 - \mathbf{E} \times (\nabla \times \mathbf{E})\,. \qquad 5\text{–}8$$

By replacing 3-5 into 3-4 and using the Faraday's law ($\nabla \times \mathbf{E} = -\partial_\mathrm{t}\mathbf{B}$), we will have:

$$\mathbf{F_{Lorentz}} = \frac{1}{2}\epsilon_0 \epsilon_\mathrm{m} \alpha \nabla|\mathbf{E}|^2 + \epsilon_0 \epsilon_\mathrm{m} \alpha \frac{\partial}{\partial \mathrm{t}} (\mathbf{E} \times \mathbf{B})\,. \qquad 5\text{–}9$$

Taking the time average of 3-6, we will have:

$$\mathbf{F_{gradient}} = \langle \mathbf{F_{Lorentz}} \rangle_\mathrm{t} = \frac{1}{4}\epsilon_0 \epsilon_\mathrm{m} \alpha \nabla|\mathbf{E}|^2 + \epsilon_0 \epsilon_\mathrm{m} \alpha \mu_0 \frac{\partial \mathbf{S}}{\partial \mathrm{t}}, \qquad 5\text{–}10$$

where μ_0 is the permeability of free space and **S** is the Poynting vector. Finally, if we assume a time-constant electric field intensity, and by considering $\mathrm{I_{inc}} \propto |\mathbf{E}|^2$, the optical gradient force can be expressed as:

$$\mathbf{F_{gradient}} = \frac{1}{4}\epsilon_0 \epsilon_\mathrm{m} \alpha \nabla|\mathbf{E}|^2 \propto \frac{1}{4}\epsilon_0 \epsilon_\mathrm{m} \alpha \nabla \mathrm{I_{inc}} \qquad 5\text{–}11$$

One can understand from Eq. 5-11 that, for a particle with higher refractive index than the medium (i.e., positive polarizability), such as the polystyrene beads used in our experiments, the gradient force pulls the particle along the electric field intensity gradient, toward the regions with higher electric field intensity. Whereas for a particle with a lower refractive index than the medium (i.e., negative polarizability), such as vapor or air bubbles, the gradient force push the particles in the opposite direction of the electric field intensity gradient, toward the regions with lower intensity.

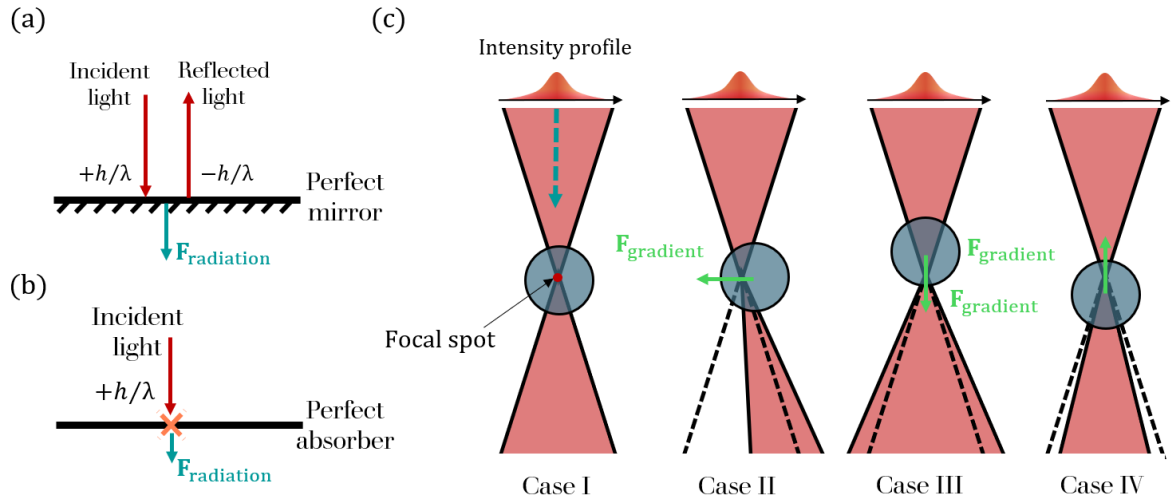

Figure 5.1 Ray optic illustration of (a) Radiation pressure force act on a perfect mirror. (b) Radiation pressure force act on perfect absorber (c) gradient forces act on a dielectric sphere when the particle is at the focal spot (case I: no gradient force), and when the particle is slightly displaced from the focal spot (Case II to case IV).

Although, the dipole (Rayleigh) approximation gives us a great insight into the trapping mechanism and how the gradient force is related to the intensity of incident light and the polarizability of trapped particle, it is insufficient in most common cases where the size of the trapped particle and trapping wavelength are comparable.

Large dielectric particles will redirect photon momentum due to refraction, resulting in a counterforce on the particle. Hence, an attractive potential is created near the intensity maximum of the trapping laser. This is referred to as the ray optics approximation of optical tweezers. Figure 5.1 (c) shows an overview of optical trapping gradient force using the ray optics approximation for a dielectric sphere that is transparent at the wavelength of the trapping laser. In case I, since the particle is positioned at the focal spot, the momentum of the transmitted light will be same as the incident light, therefore no gradient force will act on the particle. However, when the particle is slightly displaced from the focal point (case II to case IV), then the transmitted light momentum will change, and as required by the conservation of momentum, this will result in a force on the particle that pulling it back to the focal spot.

Because of the additional radiation pressure force (not illustrated in Figure 5.1 (c)), the particle tends to be displaced slightly away from the laser focal spot along the optical axis. For this reason, highly focused beams are typically required to ensure that any small perturbation of the trapped particle position will result in a resorting force towards the focal spot. Tightly focused

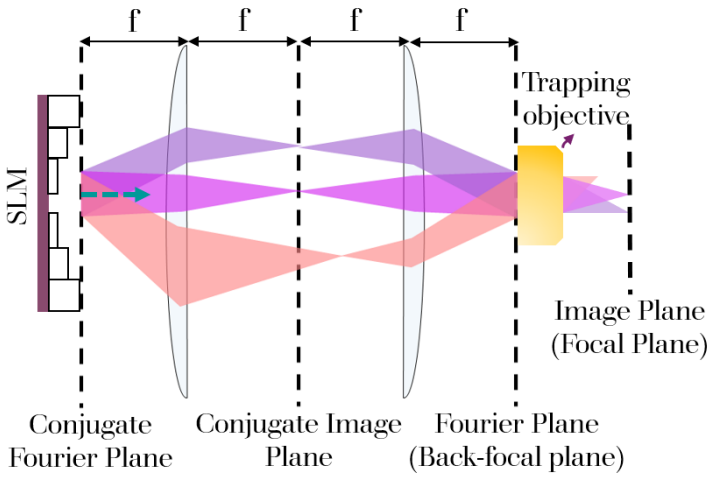

Figure 5.2 An SLM and a 4-f correlator used to control the position of the trapping laser focal spot. Three cases are shown: nominal beam path (bright purple), deflected beam path (dark purple), deflected and convergent beam path (pink).

beam can be achieved by a high numerical aperture microscope objective. Using this methodology, one can stably trap dielectric microspheres in water, being able to overcome other external forces to maintain confinement of the trapped particle.

For small displacements from the equilibrium position, the restoring optical force change linearly with the displacement along each axis, making the restoring force Hookean:

$$\mathbf{F}_{\mathbf{i,\,restoring}} = K_{\mathrm{i}}\Delta\mathbf{r}_{\mathbf{i}}\,, \qquad 5\text{–}12$$

in which, K_{i} and $\Delta\mathbf{r}_{\mathbf{i}}$ are the spring constant and the displacement along the i axis, respectively.

Now, if we are able to move the focal spot of the laser, we can use it to move the trapped particle. One way to do this is to utilize a *4-f correlator*. Figure 5.2 shows how the changes in direction and convergence of light at the conjugate Fourier plane, will change the position of the laser focal spot at the trapping objective image plane.

So, the question now is how we can control the direction and convergence of light at the conjugate Fourier plane?

A Spatial Light Modulator (SLM) can be used to control the light phase profile at a specific plane. In our experiments we have used a “liquid crystal on silicon”-SLM which consists of a 2D array of liquid crystal cells on top of a reflective silicon mirror. Each element in this array

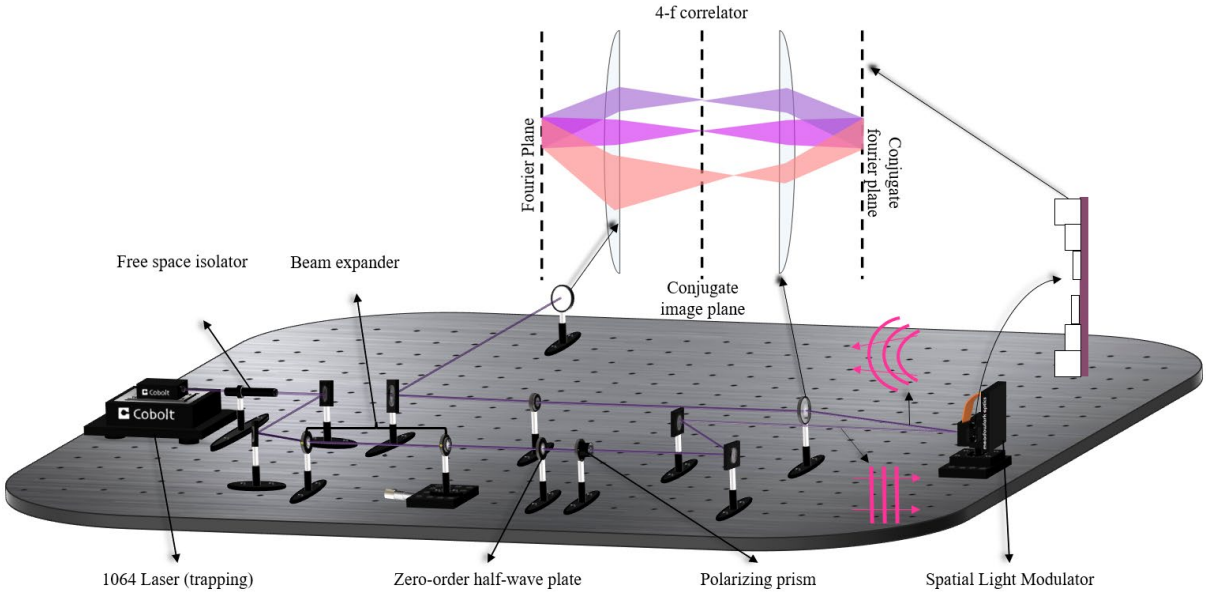

Figure 5.3 Three-dimensional plot of the holographic optical tweezing setup consists of a 1064 nm wavelength trapping laser, and an SLM and a 4-f correlator to control the position of the trapping laser focal spot.

can be controlled by an applied voltage, which changes the orientation of the liquid crystal molecules. As a result, the reflected beam phase profile can be controlled by creating a specific optical path length for each pixel in the 2D array. Therefore, by placing the SLM at a conjugate Fourier plane, it is possible to control the spatial distribution of **k**. Figure 5.3 shows the three-dimensional plot of the holographic optical tweezing setup we used in our experiments.

5.2.2. Force measurements with QPD

As mentioned in the previous section, any perturbation in the position of the trapped particle position will cause a change in the direction of the transmitted light. These small changes can be measured to determine any external forces (Marangoni flow for example) that may have caused this displacement. To do so we can collect the intensity distribution of transmitted light, using a QPD at the conjugate Fourier plane. The QPD consists of four photodiodes arranged in a 2×2 array shown in Figure 5.4. The voltage output signals of the QPD are the difference between the intensity of light detected by the top and bottom rows (ΔBT), left and right columns (ΔLR), and sum of all four quadrants ($\sum$).

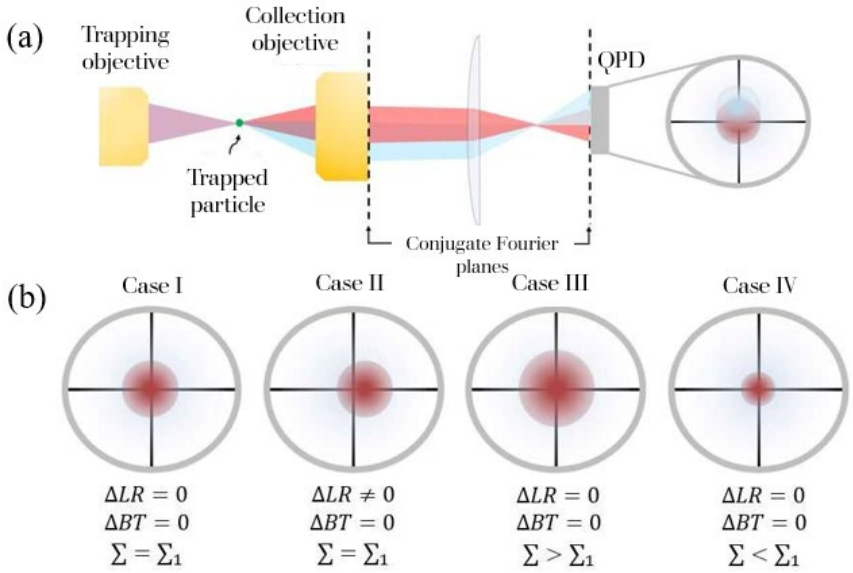

Figure 5.4 (a) Overview of the experimental setup used for measuring trapped particle displacement via transmitted light. The back focal plane (Fourier plane) of the collection objective is imaged onto a QPD. (b) How particle displacement in the cases discussed and plotted in Figure 5.b changes the intensity distribution on the QPD.

Figure 5.4 (b) illustrates how, for the cases discussed and plotted in figure 5.2 (c), the intensity distribution of the transmitted light changes on the QPD plane.

In order to be able to use this method to measure the particle displacement, we have to make sure that a linear change in the voltage signal corresponds to a linear change in the particle position. In another words, a linear change in the particle position must result in a linear change in the transmitted light momentum (a.k.a **k** vector distribution), guaranteeing that the restoring force is Hookean. To check this condition, an adhered bead on the microscope slide was scanned in front of the trapping focal spot by moving a piezo stage with a known velocity along each principal axis. The QPD response to particle displacement is shown in Figure 5.5 (a). Considering the histogram of measured displacements (shown in Figure 5.5 (b)) we can say that we are operating within the linear regime.

Finally, in order to convert the collected data from signals in volt to displacement in meters, we need to calibrate our QPD response. A trapped object, within the linear regime, can be approximated as a Brownian particle in a harmonic potential. To gain a better insight of this approximation, and how we can use it for our calibration, we should first briefly discuss Brownian motion.

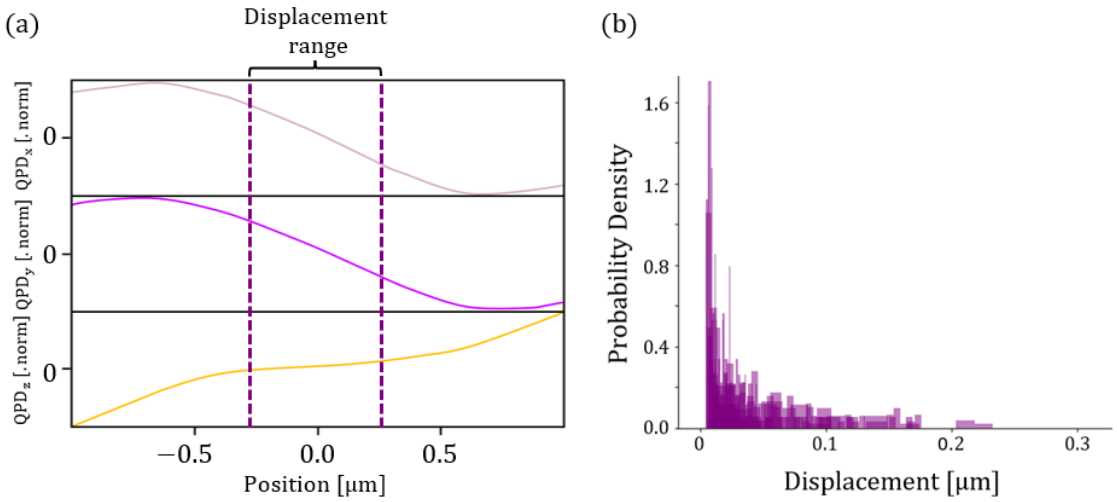

Figure 5.5 (a) The curves show the QPD response vs the bead displacement from its nominal position. (b) Histogram of measured displacements which shows that we are operating within the linear regime.

Brownian motion

Brownian motion arises from the random kinetic impulses exerted by adjacent fluid molecules. The Langevin equation can be used to model how these random kinetic impulses affect the motion of a particle in a fluid.

Given that we used spherical microbeads in our experiments, we modelled the particle in our study as a rigid sphere in a viscous medium. The kinetic impulses exerted by the adjacent fluid molecules were represented by the stochastic force, $F_{thermal}$. Lastly, it is important to note that we are considering a free spherical particle moving in one direction (x), and that the system is in thermal equilibrium.

$$m\ddot{x}(t) + \gamma_0\dot{x} = F_{thermal}. \qquad 5\text{–}13$$

Here, $m\ddot{x}(t)$ is the inertial term and m is the mass of the particle, $\gamma_0\dot{x}$ is the stokes drag force and γ_0 is the Stokes drag coefficient. We have previously shown in Chapter III, for a spherical particle with radius a, the Stokes drag force is equal to $6\pi\mu a\dot{x}$, and therefore $\gamma_0 = 6\pi\mu a$

Let's start with multiplying both side of 3-10 by x, and take the ensemble average:

$$m\langle x\ddot{x}\rangle + \gamma_0\langle x\dot{x}\rangle = \langle xF_{thermal}\rangle. \qquad 5\text{–}14$$

Since there is no correlation between the thermal force and the position and considering the random nature of the force with a mean of zero, the term on the right-hand side of the equation will be zero. Also, by considering $\frac{d}{dt}\langle x\dot{x}\rangle = \langle x\ddot{x}\rangle + \langle \dot{x}^2\rangle$, Eq. 5-14 will turn into:

$$m\left(\frac{d}{dt}\langle x\dot{x}\rangle - \langle \dot{x}^2\rangle\right) + \gamma_0\langle x\dot{x}\rangle = 0\,. \qquad 5\text{–}15$$

We know based on the equipartition theorem, that in thermal equilibrium, the thermal energy is equally shared among all degrees of freedom, so for a spherical particle moving in one dimension, the average kinetic energy is $\frac{1}{2}m\langle \dot{x}^2\rangle = \frac{1}{2}k_B T$. As a result, Eq. 5-15 can be written as:

$$\frac{d}{dt}\langle x\dot{x}\rangle = \frac{k_B T}{m} - \frac{\gamma_0}{m}\langle x\dot{x}\rangle\,. \qquad 5\text{–}16$$

If we take the ansatz $\langle x\dot{x}\rangle = A_0 e^{-\gamma_0 \frac{t}{m}} + A_1$ (where A_0 and A_1 are constants), and insert it into Eq. 5-16, we realize that A_1 must be equal to ${k_B T}/{\gamma_0}$. So, we can write $\langle x\dot{x}\rangle$ as:

$$\langle x\dot{x}\rangle = A_0 e^{-\gamma_0 \frac{t}{m}} + {k_B T}/{\gamma_0}. \qquad 5\text{–}17$$

Now, if we take the limit as $t \to \infty$ for 5-17:

$$\lim_{t\to\infty}\langle x\dot{x}\rangle = {k_B T}/{\gamma_0}. \qquad 5\text{–}18$$

Considering that $\frac{d}{dt}\langle x^2\rangle = 2\langle x\dot{x}\rangle$ and solving for $\langle x^2\rangle|_{t\to\infty}$ gives:

$$\langle x^2\rangle = \frac{2k_B T}{\gamma_0}t = 2Dt\,. \qquad 5\text{–}19$$

The term $\langle x^2\rangle$ is referred to as the Mean Squared Displacement (MSD) and is useful for characterizing the diffusion of Brownian particles. As we can observe, MSD has a linear dependence on time, with a proportionality constant, D, which as we previously mentioned is referred to as the diffusivity.

Now, let's define the thermal force as $F_{thermal} = \varrho\xi(t)$, where ϱ is the amplitude of the Brownian motion, and $\xi(t)$ is a Gaussian random variable that accounts for the stochastic nature of the thermal force. We can discard the inertial term in the Langevin equation in the long-time limit and simplify it to only include the drag force and the thermal force.

$$\dot{x} = \frac{\varrho}{\gamma_0}\xi \;\rightarrow\; x - x_0 = \frac{\varrho}{\gamma_0}\int_0^t \xi(t')dt', \qquad 5\text{–}20$$

where x_0 is the value of x at $t = 0$.

Now, if we consider $x_0 = 0$, by squaring both sides of the equation and take the ensemble average:

$$\langle x^2 \rangle = \frac{\varrho^2}{\gamma_0^2}\int_0^t \langle \xi^2 \rangle dt\,. \qquad 5\text{–}21$$

Since $\langle \xi^2 \rangle = 1$, we will have:

$$\langle x^2 \rangle = \frac{\varrho^2}{\gamma_0^2} t + C_0\,. \qquad 5\text{–}22$$

Since we considered $x_0 = 0$, then C_0 must also be zero. By comparing equations 5-19 and 5-22, we get:

$$\varrho = \sqrt{2k_B T\gamma_0}\,. \qquad 5\text{–}23$$

This equation shows the dependency of Brownian motion to the drag force.

As we mentioned in the previous section, a trapped object, within the linear regime can be approximated as a Brownian particle in a harmonic potential. To add the harmonic potential to our model, we simply should add the restoring Hookean force. In this case, the Langevin equation can be expressed as follows, while still discarding the inertial term:

$$\gamma_0 \dot{x} + Kx = \sqrt{2k_B T\gamma_0}\,\xi(t)\,. \qquad 5\text{–}24$$

Now, if we take the Fourier transform of this equation, we will have:

$$\tilde{x} = \frac{\sqrt{2k_B T\gamma_0}\,\tilde{\xi}}{K - i\omega\gamma_0}\,. \qquad 5\text{–}25$$

Finally, if we obtain the Power Spectral Density (PSD) in the long-time limit, using Eq. 3-22, we will get:

$$\mathrm{PSD} = \frac{2k_B T\gamma_0}{K^2 + \omega^2 {\gamma_0}^2}\,. \qquad 5\text{–}26$$

By defining a characteristic (corner) frequency $f_c = K/2\pi\gamma_0$, we will have:

$$\mathrm{PSD} = \frac{\mathrm{D}}{2\pi^2(\mathrm{f}_c^2 + \mathrm{f}^2)}. \qquad 5\text{–}27$$

QPD calibration

Now, for calibrating the QPD signal, first, we trap a probe particle and collect the time series obtained by the QPD for a limited time, then we convert this time series to PSD, and fit it with equation 5-27, and extract the diffusivity, $\mathrm{D_i}[\mathrm{V}^2/\mathrm{Hz}]$ along i direction ($\mathrm{i} = 1, 2, \text{and } 3$). Then we calculate the conversion factor, $\beta_\mathrm{i}[\mathrm{m/V}]$ by:

$$\beta_\mathrm{i} = \sqrt{\frac{\mathrm{D_i(h)}}{\mathrm{D_i}}}, \qquad 5\text{–}28$$

where, h is the distance from the substrate surface, and $\mathrm{D_i(h)}[\mathrm{m}^2/\mathrm{Hz}]$ is equal to $k_B\mathrm{T}/\gamma_\mathrm{i}(\mathrm{h})$. Here, $\gamma_\mathrm{i}(\mathrm{h})$ is the is Stokes' drag coefficient for the probe particle, corrected for boundary effects using Faxén's law [173-175].

$$\gamma_\parallel(\mathrm{h}) = \gamma_0\left[1 - \frac{9}{8}\frac{\mathrm{a}}{2\mathrm{h}} + \left(\frac{\mathrm{a}}{2\mathrm{h}}\right)^3 + \frac{45}{16}\left(\frac{\mathrm{a}}{2\mathrm{h}}\right)^4 - 2\left(\frac{\mathrm{a}}{2\mathrm{h}}\right)^5\right]^{-1} \qquad 5\text{–}29$$

$$\gamma_\perp(\mathrm{h}) = \gamma_0\left[\frac{4}{3}\sinh(\beta)\sum_{\mathrm{n}=1}^{\infty}\left\{\frac{\mathrm{n(n+1)}}{(2\mathrm{n}-1)(2\mathrm{n}+3)} \times\left(\frac{2\sinh\big(\mathrm{B}(2\mathrm{n}+1)\big) + (2\mathrm{n}+1)\sinh(2\mathrm{B})}{4\sinh^2(\mathrm{B}\left(\mathrm{n}+\frac{1}{2}\right) - (2\mathrm{n}+1)^2\sinh^2(\mathrm{B}))} - 1\right)\right\}\right], \qquad 5\text{–}30$$

where $\gamma_\parallel$ and $\gamma_\perp$ are the drag coefficients for directions parallel and perpendicular to the boundary, respectively, and B is equal to $\cosh^{-1}(\mathrm{h/a})$.

Then, by multiplying the time series by the conversion factor, we will convert our signal to the particle displacement in meter.

In our experiments, we typically perform the calibration step at the beginning of each measurement before inducing any flow in the system. This involves collecting the QPD signal of a trapped particle for one second and following the steps outlined above to extract the conversion factor.

Figure 5.6 shows the three-dimensional plot of the force microscopy setup we used in our experiments.

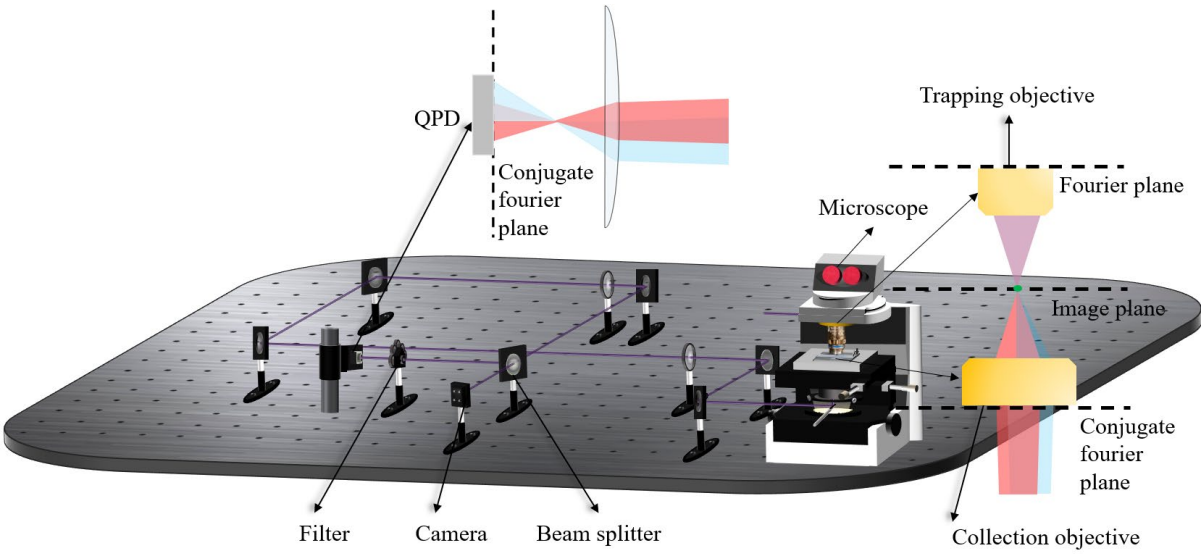

Figure 5.6 Three-dimensional plot of the force microscopy setup consists of a 1064 nm wavelength trapping laser, and a QPD for measuring trapped particle displacement via transmitted light.

Force measurement

To measure the external forces exerted on the trapped particle by the flow, we employed the following equation:

$$F_{ex,i} = K_i x_i + \gamma_i(h)\frac{dx_i}{dt}. \qquad 5\text{–}31$$

In this equation, x_i represents the displacement along each axis after inducing a flow, K_i is equal to $2\pi\gamma_i(z)f_{c,i}$, where $f_{c,i}$ is extracted by fitting the PSD of x_i with Eq. 5-27, and $\gamma_i(h)$ is calculated using 5-29 and 5-30. Finally, to calculate the velocity, we simply divide the equation above by $\gamma_i(h)$.

In paper I, a 1064 nm laser is used for trapping the probe polystyrene beads with the diameter of 2 µm.

After we have obtained the flow profiles around the nanostructures, it's time to validate and compare them by numerical simulations. For that we have used the Stokeslet approximation and FEM simulations.

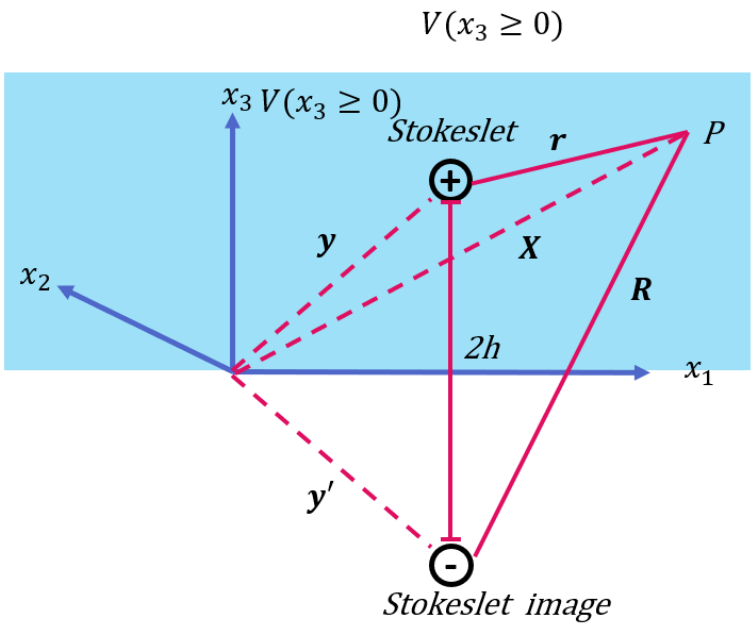

Figure 5.7 The position of stokeslet and its image, and relevant vectors $\boldsymbol{X}$, $\boldsymbol{r}$ and $\boldsymbol{R}$.

5.3. Stokeslet approximation

The solution for the flow velocity around a microscopic bubble nucleated on a no-slip interface can be obtained by embedding a singular point force (*Stokeslet*) at the distance $(+h)$ from a stationary no-slip plane boundary in an infinite viscous fluid (V), and its image (*Stokeslet image*) at the distance $(-h)$ form the boundary [176].

Figure 5.7 shows the image system and its relevant vectors. Here, $\boldsymbol{X} = (X_1, X_2, X_3)$ is the coordinate of the point (P) in which we want to calculate the velocity, $\boldsymbol{y} = (y_1, y_2, h)$ and $\boldsymbol{y}' = (y'_1, y'_2, -h)$ are the coordinates of the Stokeslet and Stokeslet image, and the translated coordinates $\boldsymbol{r} = (r_1, r_2, r_3)$, and $\boldsymbol{R} = (R_1, R_2, R_3)$ are defined as $(\boldsymbol{X} - \boldsymbol{y})$ and $(\boldsymbol{X} - \boldsymbol{y}')$, respectively [176].

The velocity vector can be calculated by:

$$u_i = F_j G_i^j, \qquad 5\text{–}32$$

where F_j is the amplitude of the Stokeslet in the j direction and G_i^j is the Green's function. So, all we have to do is to construct a Green's function.

$$G_i^j = u_i^j + v_i^j, \qquad 5\text{–}33$$

where, u_i^j and v_i^j are the fundamental singular solutions due to the Stokeslet and Stokeslet image, respectively [176].

Let's start with u_i^j. To obtain u_i^j, we need to solve the Navier-Stokes equation we have obtained in Eq. 4.7 for an incompressible fluid in the laminar flow regime with Boussinesq approximation at steady state, considering the point source as a unit vector in the j direction at $\boldsymbol{X} = \boldsymbol{y}$. In addition, we will consider the following conditions:

1- We will consider the image as point force of equal magnitude, but of opposite sign.

2- We consider the plane boundary to be $x_3 = 0$ ($u = 0\ on\ x_3 = 0$).

3- And finally, we ignore any other external forces including gravity.

Considering these assumptions, the Navier-Stokes equation can be written as:

$$\nabla \boldsymbol{p^j} = \mu \nabla^2 \boldsymbol{u^j} + \boldsymbol{e^j}\delta(\boldsymbol{X} - \boldsymbol{y}). \qquad 5\text{–}34$$

The solution to this equation can be obtained by implementing a three-dimensional Fourier transform with suitable conditions at infinity. This results in the following velocity components:

$$u_i^j = \frac{1}{8\pi\mu}\left[\frac{\delta_{ij}}{r} + \frac{r_i r_j}{r^3}\right], \qquad 5\text{–}35$$

in which, $r = \sqrt[2]{(r_1^2 + r_2^2 + r_3^2)}$ is the distance between the Stokeslet and the point (P).

Now, we turn to the problem of obtaining complementary solution v_i^j. The Navier-Stokes equation can be written as:

$$\nabla \boldsymbol{q^j} = \mu \nabla^2 \boldsymbol{v^j} - \boldsymbol{e^j}\delta(\boldsymbol{X} - \boldsymbol{y'}), \qquad 5\text{–}36$$

where $\boldsymbol{q^j}$, and $\boldsymbol{v^j}$ are the complementary pressure and velocity singularities. To solve this equation, we have to consider the following boundary condition:

$$\boldsymbol{v^j}(S) = -\boldsymbol{u^j}(S), \qquad 5\text{–}37$$

where S defines the set of points on the plane boundary. This will guarantee the no-slip condition on the boundary.

Considering this condition and by implementing a two-dimensional Fourier transform the solution for v_i^j is:

$$v_i^j = \frac{1}{8\pi\mu}\left[-\left[\frac{\delta_{ij}}{R}+\frac{R_iR_j}{R^3}\right]+2h\left(\delta_{j\alpha}\delta_{\alpha k}-\delta_{j3}\delta_{3k}\right)\frac{\partial}{\partial R_k}\left\{\frac{hR_i}{R^3}-\left[\frac{\delta_{i3}}{R}+\frac{R_iR_3}{R^3}\right]\right\}\right]. \quad 5\text{–}38$$

Where $\alpha = 1,2$, and δ_{ij} signifies the Kronecker delta while the tensor $\left(\delta_{j\alpha}\delta_{\alpha k}-\delta_{j3}\delta_{3k}\right)$ is non-zero only when $j = k$ and equal to +1 for $j = 1$ or 2, and -1 for $j = 3$, and $R = \sqrt[2]{(R_1^2+R_2^2+R_3^2)}$ is the distance between the Stokeslet image and the point (P) [177].

Finally, by substituting 5-37 and 5-38 in 5-33, and 5-32, u_i will be defined as:

$$u_i = \frac{F_j}{8\pi\mu}\left[\left[\frac{\delta_{ij}}{r}+\frac{r_ir_j}{r^3}\right]-\left[\frac{\delta_{ij}}{R}+\frac{R_iR_j}{R^3}\right]+2h\left(\delta_{j\alpha}\delta_{\alpha k}-\delta_{j3}\delta_{3k}\right)\frac{\partial}{\partial R_k}\left\{\frac{hR_i}{R^3}-\left[\frac{\delta_{i3}}{R}+\frac{R_iR_3}{R^3}\right]\right\}\right]. \quad 5\text{–}39$$

To model the flow around a bubble with only out of plane temperature gradient, it's enough to assume one stokeslet, $S = (0,0,F_3)$, on $(0,0,h)$. However, for a bubble with both in plane and out of plane temperature gradients, one should add a force pointing in the direction of in plane temperature gradient to be able to model the flow. For example, if we have an in plae temperature gradient in the direction of +x, this will result in a tilted stokeslet, $S = (F_1,0,F_3)$, on $(0,0,h)$.

To model the experimental flows, F_1 and F_3 can be estimated by comparing the results of the Stokeslet calculation to experimentally measured flow vectors, and h can be estimated considering the expected bubble sizes.

Figure 5.8 (a) shows the Stokeslet calculation of Marangoni flow induced by two bubbles with opposing temperature gradients. The experimentally measured flow vectors are obtained from the case of a pair of asymmetric arrays with edge-to-edge distance of 2 μm, presented in Paper I [178], where the left and right arrays consist of 19, and 37 circular and ellipsoidal gold nanodisks respectively, and the incident light polarization is parallel to the long-axis of the ellipsoidal structure.

In addition to Stokeslet approximation, we have used FEM simulations for modelling the flow and the temperature field around our nanostructures.

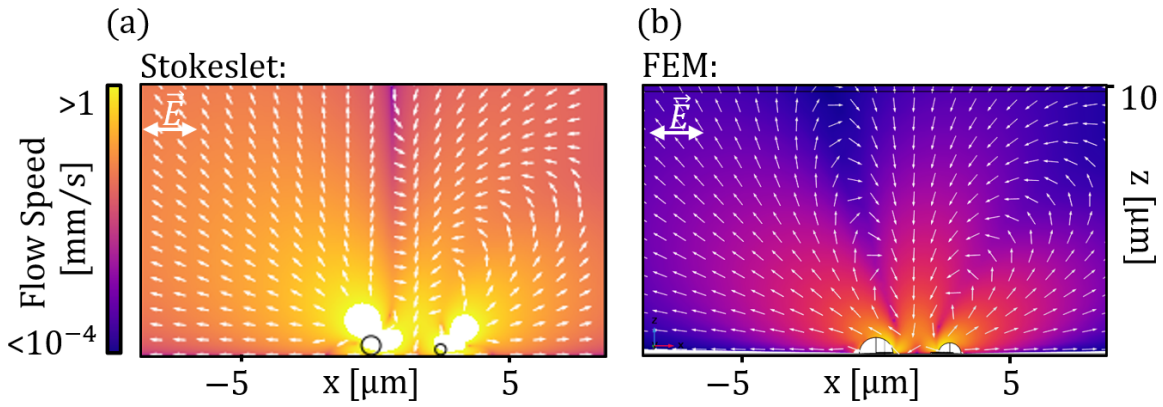

Figure 5.8 (a) Stokeslet and (b) FEM simulation of Marangoni flow induced by two unequal nearby bubbles with an additional temperature gradient parallel to the surface corresponding to the experimentally measured flow vectors around a pair of asymmetric arrays with edge-to-edge distance of 2 µm, where the left and right arrays consist of 19, and 37 circular and ellipsoidal gold nanodisks respectively, and the incident light polarization is parallel to the long-axis of the ellipsoidal structure.

5.4. FEM simulations of flows and thermal distributions

We have already gone through most of the theory and equations we have used in the FEM simulations of flows and thermal distributions using COMSOL. For these simulations we have used the Heat Transfer in Solids and Fluids (ht), and the Laminar Flow (spf) interfaces and they were coupled by a Multiphysics branch in which Nonisothermal Flow multiphysics coupling was used to couple the flow properties to the heat transfer mechanism. Additionally, the Marangoni Effect multiphysics coupling was used to account for Marangoni convection on the surface of the bubbles' domain. In all the domains, the conductive and convective heat transfers were considered. To calculate the temperature distribution, the nanodisks were considered as heat source domains with a heat source density Q based on their absorption cross sections, obtained from the FEM simulations which were explained earlier, and position dependent incident intensities determined by assuming a Gaussian laser beam profile. A no slip boundary condition was considered for all the stationary solid walls in the simulation domain. To be able to model the Marangoni convection on the bubble surface, a slip boundary condition was considered, however, a no-penetration condition was still assumed to prevent fluid from leaving and entering the bubble domain. The side length of the simulation domain was in average 10^3 times larger than the characteristic dimension of our largest heating arrays, and a room temperature boundary condition was considered on the walls of the simulation domain.

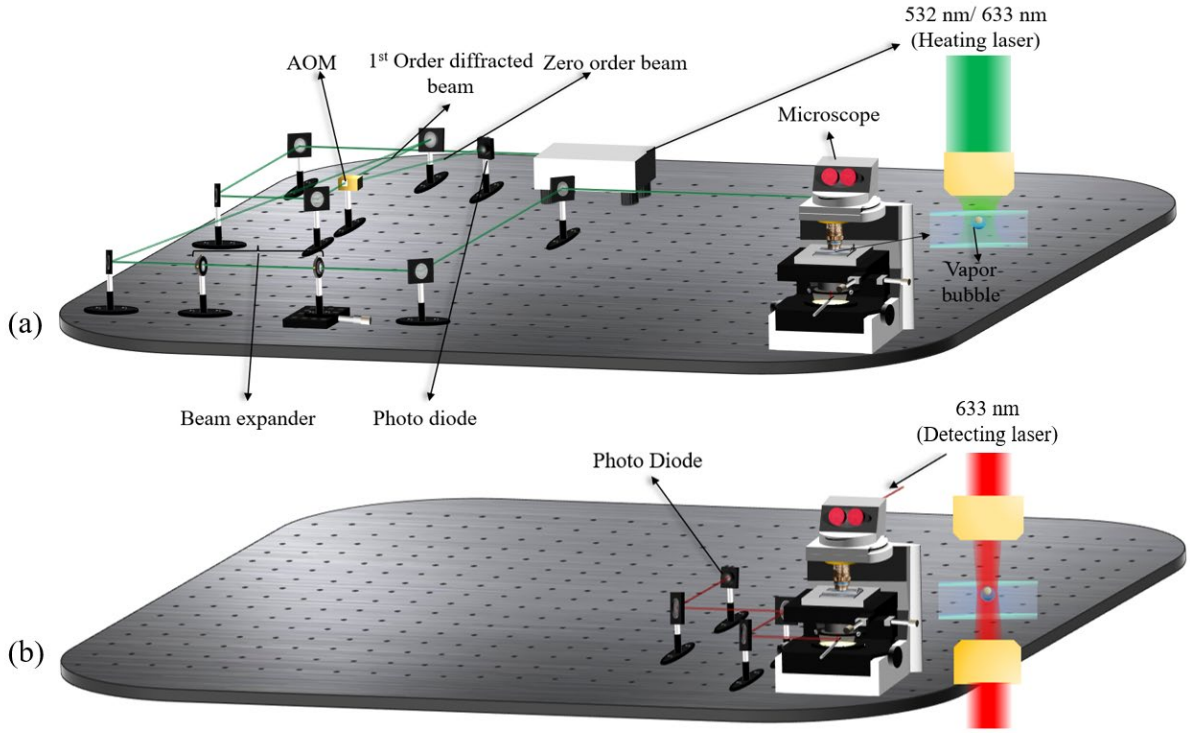

Figure 5.9 Three-dimensional plot of (a) bubble generation setup consists of a 532 nm wavelength heating laser and an AOM for modulation of the heating laser intensity. (b) bubble detection setup consists of 633 nm wavelength detecting laser and a photo diode for collecting the detecting laser transmitted signal.

Figure 5.8 (b) shows the FEM simulation of Marangoni flow induced by the same arrays described in the previous section.

5.5. Vapor bubble generation and detection

The physical mechanism for bubble generation was explained in Chapter III. In both paper I, and II, a 532 nm laser was used for generating bubbles on top of gold or a-Si arrays consist of circular nanodisks. Additionally, in paper I, a 660 nm laser was used for generating bubbles for the case of polarization dependent structures. In both papers, the heating lasers were modulated in a square wave temporal profile with a duty cycle of 50% and frequency f_m. Figure 5.9 (a) shows the three-dimensional plot of the setup we used for bubble generation. bubble generation setup used in all of our experiments.

In paper I, the transmission of a 633 nm wavelength laser which was coaligned with the heating laser, was used for detecting bubbles. A decrease of the transmission then indicates the bubble

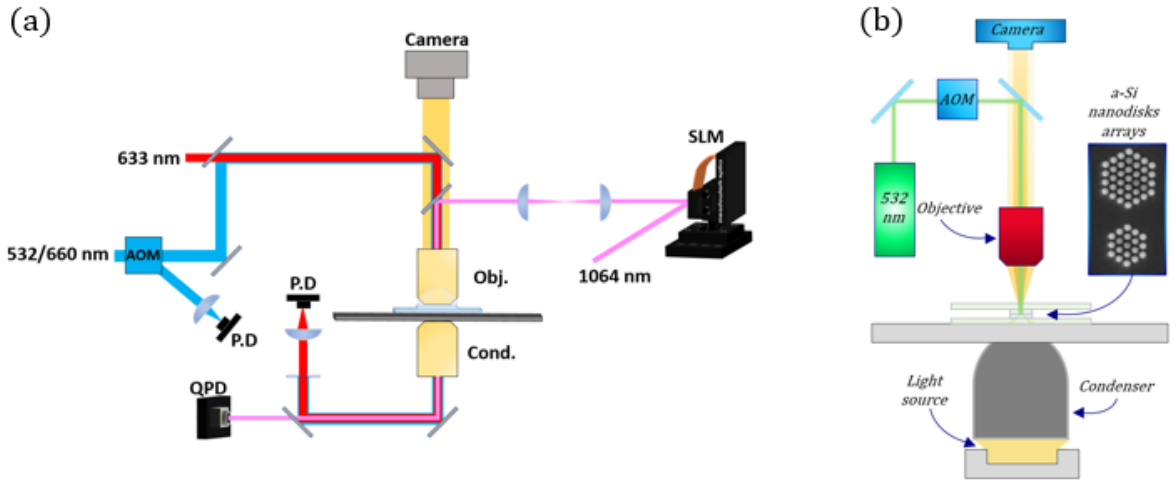

Figure 5.10 Schematic drawing of the experimental setup which include (a) a 1064 nm wavelength laser with an SLM and QPD for optical force microscopy, a 532 nm/660 nm wavelength heating laser coupled to an an acousto-optic modulator (AOM) for modulating the heating laser, and a Photo Diode (P.D) for collecting the transmitted light form the 633 nm wavelength bubble detecting laser (b) a 532 nm wavelength laser source coupled to an AOM, a camera for tracking bubble dynamics and probe particle movement, and a white light dark-field condenser for illumination of the sample area. The inset shows a scanning electron microscopy image of a typical a-Si nanodisk array sample.

nucleation. Figure 5.9 (b) shows the three-dimensional plot of the setup we used for bubble detection in Paper I.

In paper II, the intensity of scattered light from the bubble was used for detection and characterization of the life cycle of a bubble.

Figure 5.10 (a) and (b) show the schematic drawings of the experimental setups used in paper I and II respectively.

5.6. Thermometry by Raman Stokes measurement

Finally, in our ongoing project we are using crystalline silicon (c-Si) nanodisks for optically induced bubble generation, and thermometry by Raman Stokes Measurement.

The c-Si nanodisks, with diameter and height of 100 nm, exhibit a magnetic dipole (MD) Mie resonance near 500 nm (Shown in Figure 2.7). Therefore, by using a 488 nm laser as a heating laser we can use this structure for bubble generation. But more interestingly, these nanodisks are suitable for Raman thermometry.

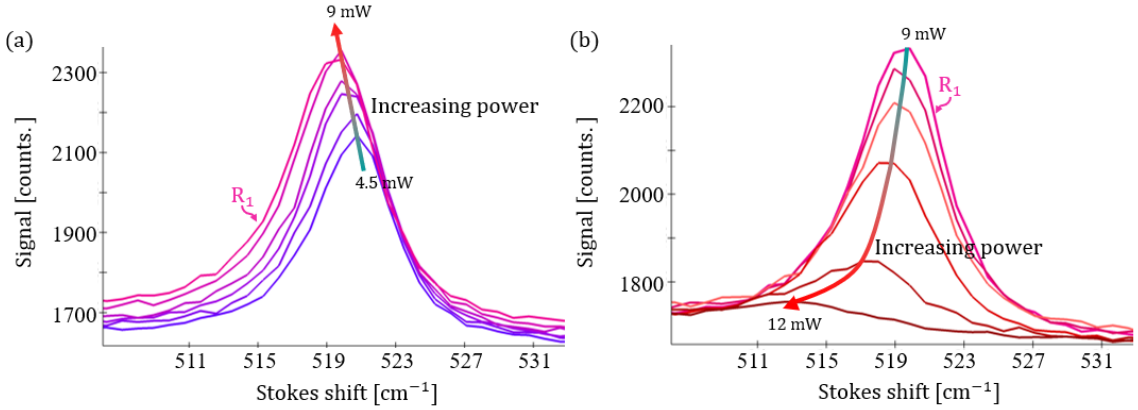

Figure 5.11 Raman spectra obtained from an array consisting of 45 nanodisks c-Si nanodisks on glass immersed in water using a heating/Raman excitation laser with a wavelength of 480 nm, and a beam waist of 500 nm. (a) the low-power regime, showing a linear shift of the phonon peak with increasing power of the heating/Raman laser, and (b) the high-power regime, showing a nonlinear shift with increasing power.

Raman thermometry of Si nanoparticles is here based on the temperature dependent vibrational frequency of the 520 cm^{-1} optical phonon, which softens with increasing temperature due to lattice expansion and anharmonicity effects. Within a broad interval between room temperature and ~550 K, the phonon frequency, Ω(T), varies almost linearly with temperature, Ω(T) = Ω(T0) + A(T – T0), with A = −0.0218 $cm^{-1}K^{-1}$ [55].

Also, the temperature of the nanostructures depends strongly on the surrounding medium. As we have mentioned previously, when a bubble is nucleated on top of a nanodisk, due to the lower heat conductivity of vapor in comparison to water, the nanodisk gets thermally isolated, which will lead to larger temperature increase with increasing power. Therefore, a nonlinear Raman shift, corresponding to a change in A, is expected to be observed due to the nucleation of the bubble. Therefore, Raman thermometry might be used to study the phenomena of boiling and for determining the boiling temperature around the nanostructures. Figure 5.11 shows Raman spectra obtained from an array consisting of 45 c-Si nanodisks on glass immersed in water, obtained using a heating/Raman laser with a wavelength of 488 nm, and a beam waist of 500 nm. Based on our preliminary observations, as the power of the heating laser increases, two distinct regimes are observable. In regime one, for lower powers, shown in Figure 5.11 (a), the phonon shifts almost linearly. On the other hand, above a certain power (~ 9 mW), the Raman peak starts to shift and broaden nonlinearly, with an increasing difference between spectra. We believe that this is due to the formation of a bubble, although additional experiments are needed to confirm and quantify the phenomenon.

5.7. Characterization of the structures

We have also used the transmission spectrum of the structures for characterizing their optical responses. Figure 5.12 shows how the experimental extinction cross section of circular and ellipsoidal gold structures used in Paper I.

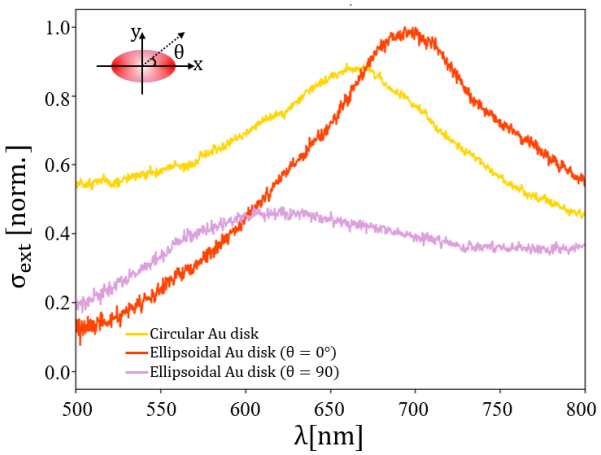

Figure 5.12 Extinction cross section spectra of gold nanodisks (yellow, diameter 100 nm, height 60 nm) and nano ellipsoids (long axis diameter 100 nm, short axis diameter 50 nm, height 60 nm) for incident polarization parallel (red) and perpendicular (purple) to the long axis.

Chapter VI: Summary of Appended Works

"Science is a self-correcting process. To publish a paper is not the end of the story—it's the beginning"

- Sydney Brenner

6.1. Paper I: Directional Control of Transient Flows Generated by Thermoplasmonic Bubble Nucleation

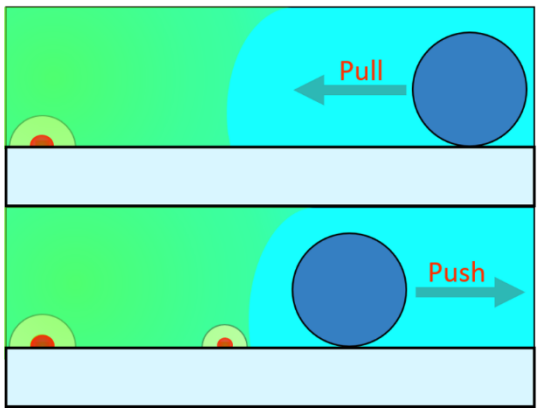

Figure 6.1 Top: Microparticle get pulled toward one plasmonic vapor bubble. Bottom: Microparticle get pushed away from two plasmonic vapor bubbles.

In this study, we utilized isolated arrays of gold nanostructures to generate heat and induce bubble nucleation. The work builds upon the findings of Jones et al., who demonstrated that the formation of a microbubble near a gold nanodisk array generates strong transient flows, followed by a weaker but sustained Marangoni flow. The primary objective of our research was to achieve dynamic and directional control over these transient flows. To accomplish this, we employed methods 2 and 3, as described in Chapter IV.

Harnessing these transient flows is crucial for optimizing mass transport near the substrate surface, where flow speed is significantly reduced due to the no-slip boundary condition. The key findings of this study were as follows:

• Directional, long-range, and rapid masstransport (exceeding 20 μm within one second in the desired direction) was achieved with low power levels around the nanostructures. This was accomplished using pairs of asymmetric arrays with different numbers of nanodisks and by modulating the heating laser.

• We demonstrated that the maximum displacement of particles around the structures is dependent on the modulation frequency of the heating laser. At a modulation frequency of $f_m = 100$ Hz, a maximum in displacement was observed. This behavior was modeled and explained by the contribution of transient flows.

• Our findings revealed that the direction of flow around the microstructures would be dynamically controlled by the polarization of the incident light. To the best of our knowledge, this is the first reported instance of flow direction being controlled via light polarization.

• Finally, we showed that the induced flow profiles would be accurately modeled using Stokeslet and finite element method (FEM) simulations.

6.2. Paper II: Bubble Dynamics and Directional Marangoni Flow Induced by Laser Heating of Silicon Nanodisks.

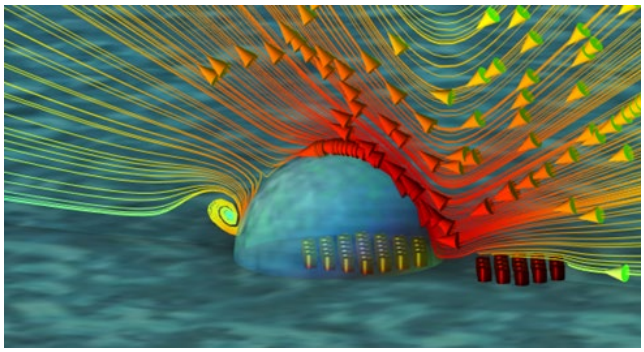

Figure 6.2 Finite Element (FEM) simulation of the flow and temperature fields around a pair of asymmetric a-Si nanodisk arrays with edge-to-edge distance of 400 nm while heated by a 532 nm wavelength Gaussian incident beam with beam waist radius of 13 μm. The left and right arrays consist of 37, and 19 nanodisks respectively, and a bubble with a radius of 0.85 μm is considered on top of the larger array.

In this study, we explored the use of isolated arrays of amorphous silicon (a-Si) nanostructures for heat generation. The primary motivation was to replace gold with a more stable and still biocompatible alternative capable of withstanding high temperatures without melting or reshaping. To achieve dynamic and directional control over the induced flows, we employed methods 1 and 2, as outlined in Chapter IV. Additionally, we investigated the life cycle of vapor bubbles nucleated by these structures. The main outcomes of this study were as follows:

- To the best of our knowledge, we demonstrated for the first time that high-refractive-index nanostructures can be used for optical micro vapor generation.

- We showed that these microbubbles induce a flow in their surroundings due to the thermal Marangoni effect and that the direction of this flow can be dynamically controlled by adjusting the position of the heating laser.

- Furthermore, we achieved directional, long-range, and rapid mass transport (exceeding 40 μm within one second in the desired direction) using low power levels around these nanostructures.

- Additionally, we examined the dynamics of microbubble formation and evolution around these structures. Initially, a large bubble nucleates on top of the nanostructures. This bubble then decays over a characteristic decay time of 35 ms, reaching a smaller, steady-state size. The steady-state bubble remains unchanged as long as the heating laser remains on.

Chapter VII: Conclusion and outlook

"But at the laste, as everything hath ende, she took hir leve, and nedes wolde wende."

- Geoffrey Chaucer

Finally, as all good things must come to an end, too must this thesis, concluding with reflections and an outlook for the future. Throughout my PhD journey, I have strived to understand the theoretical foundations behind the phenomena I observed experimentally. Yet, the deeper I delved, the more I realized how much more there is to learn.

Coming from an electrical engineering background, with little prior experience in fluid dynamics and only a foundational understanding of experimental optics from my coursework, embarking on this PhD felt like opening Pandora's box. However, as the legend goes, hope remained at the bottom of the box, and I, too, have found mine. I believe that as long as we remain curious enough to learn and committed enough to share our knowledge, there will always be hope and growth.

There were so little that I managed to do experimentally and even less that I could explain theoretically, though I hope I was able to share the little knowledge I gained through this thesis.

The purpose of this thesis was to provide a basic understanding of optical heating of subwavelength particles and the induced Marangoni flow around them. In Chapter II, we showed a subwavelength particle can absorb the energy of light and turn it into heat. We introduced and explained the absorption cross section as a measure of the probability of light being absorbed and established how the heat generated by the nanoparticle can be approximated mathematically with absorption cross section. Furthermore, we discussed how this power will increase the temperature of its surrounding environment. With that we established the basis of our Electromagnetic wave and Heat transfer FEM simulations and provide the absorption cross sections of the nanostructures we have used in our experiments.

In Chapter III, we described how these nano particles can be used for nucleating vapor bubbles in water. We did a brief literature review on vapor bubbles nucleation, and growth by CW lasers. In Chapter IV, we explained how in general temperature gradients in fluids like water can induce flow and we specifically focused on the Marangoni effect, which is the driving effect for the flows we observed experimentally. Then we briefly discussed how the flow field can be calculated by the Navier-Stokes equations, and we introduced the boundary conditions and the approximations we used later in our Fluid Flow simulations. Finally, we introduce three methods for **Controlling Flow with Light** which are based on the shifting the laser focal point, modifying the array size, and altering the absorption cross-section of the nanostructures. As we explained in the previous chapter, these were the methods we used in Paper I and Paper II to dynamically control the flow with light. Finally in Chapter V, we discuss different numerical and experimental methods we used for measurement and characterization of nanostructures, bubbles, and induced flows.

Outlook

As we briefly discussed in Chapter V, the most promising outlook is for the near future to use the array of c-Si nanodisks for both heat generation and Raman thermometry to study the boiling phenomena and boiling temperature. As discussed in Chapter III, accurate characterization of the boiling temperature at the micro scale is not an easy task. Therefore, introducing a straightforward method such as Raman thermometry for such research can be very advantageous and brings more clarity about the boiling mechanism and bubble generation around the isolated array of absorbing nanoparticles.

Another possible outlook is to assemble the nanoheaters on movable platforms. We have already fabricated the asymmetric circular gold nanodisks on circular glass disks with the diameter of 8 μm, and the height of the 500 nm (the SEM image is shown in Figure 7.1 (a)), and we have used a 532 nm wavelength laser with the beam waist radius of 4 nm for both trapping and heating. One interesting observation was that the structures always flipped inside the trap. Although the mechanism of the flipping is unknown to us, based on our experiments, the flipping will not occur for the glass disks without the gold nano structures, and the laser optical axis is always perpendicular to the axis connecting the center of the arrays, shown as red dashes line in Figure 7.1 (b). Furthermore, the flipped particles were able to create flow around them. Figure 7.1 (c) shows the trajectory of a polystyrene probe particle with the diameter of 1 μm. The asymmetrical pair consists of two arrays of 19 and 7 nanodisks with the

edge-to-edge distance of 400 nm. The lateral displacement of the trace particle is around 11 µm in 2 seconds. If designed correctly, these structures have the potential of trapping, transporting and releasing of a target material.

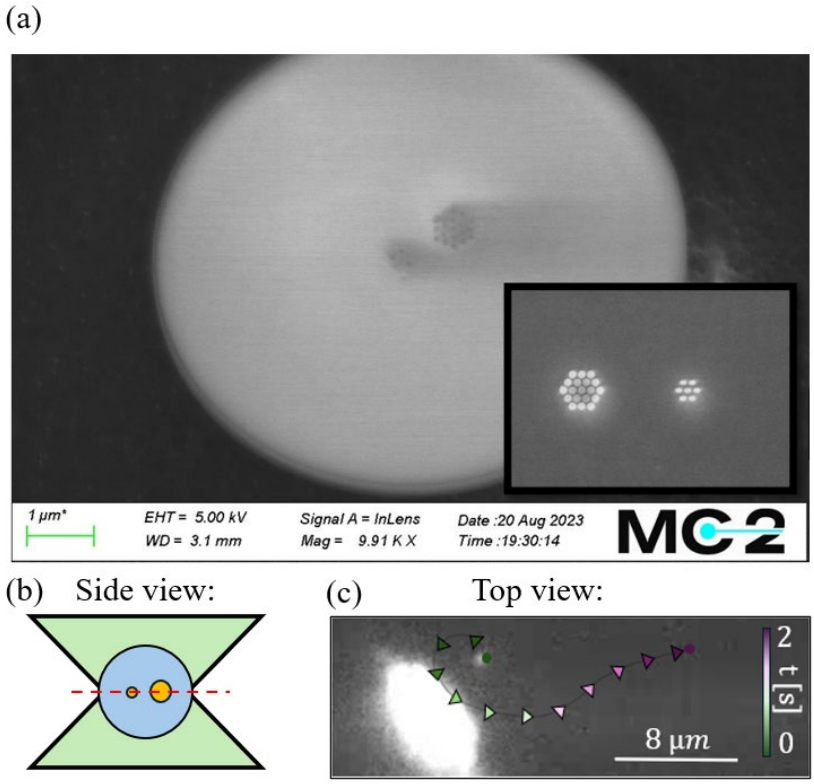

Figure 7.1 (a) SEM image of the fabricated movable nanoheaters (taken by Dr. Mohammad Mahdi Shanei) (b) The side view of the flipped and trapped portable nanoheaters in a tightly focused laser beam. (c) The trajectory of the traced particle close to the portable nanoheters.

The results presented in this thesis and the appended works provide a simple and versatile solution to a central challenge in biotechnology: the rapid transport of small liquid volumes toward a target within confined geometries. The designed structures are straightforward to fabricate and can be seamlessly integrated into various biological platforms, making them highly adaptable for practical applications in microfluidics, bio nanotechnology, particle sorting and mass transport.

Bibliography

1. Unger, M.A., et al., *Monolithic microfabricated valves and pumps by multilayer soft lithography.* science, 2000. **288**(5463): p. 113-116.
2. Erickson, D., D. Sinton, and D. Psaltis, *Optofluidics for energy applications.* Nature Photonics, 2011. **5**(10): p. 583-590.
3. Monat, C., P. Domachuk, and B.J. Eggleton, *Integrated optofluidics: A new river of light.* Nature photonics, 2007. **1**(2): p. 106-114.
4. Fan, X. and I.M. White, *Optofluidic microsystems for chemical and biological analysis.* Nature photonics, 2011. **5**(10): p. 591-597.
5. Yang, S., et al., *Recent advancements in nanophotonics for optofluidics.* Advances in Physics: X, 2024. **9**(1): p. 2416178.
6. Baffou, G. and H. Rigneault, *Femtosecond-pulsed optical heating of gold nanoparticles.* Physical Review B, 2011. **84**(3): p. 035415.
7. Baffou, G. and R. Quidant, *Thermo-plasmonics: using metallic nanostructures as nano-sources of heat.* Laser & Photonics Reviews, 2013. **7**(2): p. 171-187.
8. Baffou, G., et al., *Deterministic temperature shaping using plasmonic nanoparticle assemblies.* Nanoscale, 2014. **6**(15): p. 8984-8989.
9. Baffou, G., *Thermoplasmonics: Heating Metal Nanoparticles Using Light*. 2017, Cambridge: Cambridge University Press.
10. Baffou, G., F. Cichos, and R. Quidant, *Applications and challenges of thermoplasmonics.* Nature Materials, 2020. **19**(9): p. 946-958.
11. Jones, S., et al., *Photothermal Heating of Plasmonic Nanoantennas: Influence on Trapped Particle Dynamics and Colloid Distribution.* ACS Photonics, 2018. **5**(7): p. 2878-2887.
12. Espinosa, A., et al., *Intracellular biodegradation of Ag nanoparticles, storage in ferritin, and protection by a Au shell for enhanced photothermal therapy.* ACS nano, 2018. **12**(7): p. 6523-6535.

13. Zhu, J., et al., *Epitaxial growth of gold on silver nanoplates for imaging-guided photothermal therapy.* Materials Science and Engineering: C, 2019. **105**: p. 110023.
14. Li, X., et al., *Clinical development and potential of photothermal and photodynamic therapies for cancer.* Nature reviews Clinical oncology, 2020. **17**(11): p. 657-674.
15. Fränzl, M. and F. Cichos, *Hydrodynamic manipulation of nano-objects by optically induced thermo-osmotic flows.* Nature communications, 2022. **13**(1): p. 656.
16. Rodrigo, J.A., M. Angulo, and T. Alieva, *Tailored optical propulsion forces for controlled transport of resonant gold nanoparticles and associated thermal convective fluid flows.* Light: Science & Applications, 2020. **9**(1): p. 181.
17. Lin, L., X. Peng, and Y. Zheng, *Reconfigurable opto-thermoelectric printing of colloidal particles.* Chemical Communications, 2017. **53**(53): p. 7357-7360.
18. Tekin, E., P.J. Smith, and U.S. Schubert, *Inkjet printing as a deposition and patterning tool for polymers and inorganic particles.* Soft matter, 2008. **4**(4): p. 703-713.
19. Braun, M. and F. Cichos, *Optically controlled thermophoretic trapping of single nano-objects.* ACS nano, 2013. **7**(12): p. 11200-11208.
20. Ciraulo, B., et al., *Long-range optofluidic control with plasmon heating.* Nature Communications, 2021. **12**(1): p. 2001.
21. Hill, E.H., et al., *Opto-thermophoretic attraction, trapping, and dynamic manipulation of lipid vesicles.* Langmuir, 2018. **34**(44): p. 13252-13262.
22. Hong, N. and Y. Nam, *Thermoplasmonic neural chip platform for in situ manipulation of neuronal connections in vitro.* Nature Communications, 2020. **11**(1): p. 6313.
23. Robert, H.M., et al., *Photothermal control of heat-shock protein expression at the single cell level.* Small, 2018. **14**(32): p. 1801910.
24. Antonova, O.Y., O.Y. Kochetkova, and I.L. Kanev, *Light-to-heat converting ECM-mimetic nanofiber scaffolds for neuronal differentiation and neurite outgrowth guidance.* Nanomaterials, 2022. **12**(13): p. 2166.
25. Svedendahl, M., R. Verre, and M. Käll, *Refractometric biosensing based on optical phase flips in sparse and short-range-ordered nanoplasmonic layers.* Light: Science & Applications, 2014. **3**(11): p. e220-e220.
26. Zhang, X., et al., *Plasmonic photocatalysis.* Reports on Progress in Physics, 2013. **76**(4): p. 046401.
27. Molinaro, C., et al., *Nanochemistry by Thermoplasmonic Effects*, in *Progress in Nanophotonics 7*. 2022, Springer. p. 71-91.

28. Neumann, O., et al., *Compact solar autoclave based on steam generation using broadband light-harvesting nanoparticles.* Proceedings of the National Academy of Sciences, 2013. **110**(29): p. 11677-11681.
29. Neumann, O., et al., *Solar vapor generation enabled by nanoparticles.* ACS nano, 2013. **7**(1): p. 42-49.
30. Chen, H., et al., *Gold nanorods and their plasmonic properties.* Chemical Society Reviews, 2013. **42**(7): p. 2679-2724.
31. Girard, C., et al., *Designing thermoplasmonic properties of metallic metasurfaces.* Journal of Optics, 2018. **20**(7): p. 075004.
32. Kharintsev, S.S., et al., *Designing two-dimensional temperature profiles using tunable thermoplasmonics.* Nanoscale, 2022. **14**(33): p. 12117-12128.
33. Xie, Y. and C. Zhao, *An optothermally generated surface bubble and its applications.* Nanoscale, 2017. **9**(20): p. 6622-6631.
34. Li, J., et al., *Photothermal generation of programmable microbubble array on nanoporous gold disks.* Optics Express, 2018. **26**(13): p. 16893-16902.
35. Lombard, J., T. Biben, and S. Merabia, *Kinetics of nanobubble generation around overheated nanoparticles.* Phys Rev Lett, 2014. **112**(10): p. 105701.
36. Hühn, D., et al., *Photostimulated Au nanoheaters in polymer and biological media: characterization of mechanical destruction and boiling.* Advanced Functional Materials, 2012. **22**(2): p. 294-303.
37. Fang, Z., et al., *Evolution of light-induced vapor generation at a liquid-immersed metallic nanoparticle.* Nano letters, 2013. **13**(4): p. 1736-1742.
38. Carlson, M.T., A.J. Green, and H.H. Richardson, *Superheating water by CW excitation of gold nanodots.* Nano letters, 2012. **12**(3): p. 1534-1537.
39. Baffou, G., et al., *Super-Heating and Micro-Bubble Generation around Plasmonic Nanoparticles under cw Illumination.* The Journal of Physical Chemistry C, 2014. **118**(9): p. 4890-4898.
40. Cooper, J. and R. Dooley, *The international association for the properties of water and steam.* Proceedings of the International Association for the Properties of Water and Steam (IAPWS), 1993.
41. Hao, Y., Y. Zhang, and A. Prosperetti, *Mechanics of gas-vapor bubbles.* Physical review fluids, 2017. **2**(3): p. 034303.

42. Hu, M., H. Petrova, and G.V. Hartland, *Investigation of the properties of gold nanoparticles in aqueous solution at extremely high lattice temperatures.* Chemical physics letters, 2004. **391**(4-6): p. 220-225.

43. Plech, A., et al., *Laser-induced heating and melting of gold nanoparticles studied by time-resolved x-ray scattering.* Physical Review B—Condensed Matter and Materials Physics, 2004. **70**(19): p. 195423.

44. Jones, S., et al., *Ultrafast Modulation of Thermoplasmonic Nanobubbles in Water.* Nano Letters, 2019. **19**(11): p. 8294-8302.

45. Jones, S., et al., *Strong Transient Flows Generated by Thermoplasmonic Bubble Nucleation.* ACS Nano, 2020. **14**(12): p. 17468-17475.

46. Zapka, W., W. Ziemlich, and A.C. Tam, *Efficient pulsed laser removal of 0.2 μm sized particles from a solid surface.* Applied physics letters, 1991. **58**(20): p. 2217-2219.

47. Tam, A.C., et al., *Laser-cleaning techniques for removal of surface particulates.* Journal of Applied Physics, 1992. **71**(7): p. 3515-3523.

48. Ohta, A.T., et al., *Optically actuated thermocapillary movement of gas bubbles on an absorbing substrate.* Applied physics letters, 2007. **91**(7).

49. Zograf, G.P., et al., *Resonant nonplasmonic nanoparticles for efficient temperature-feedback optical heating.* Nano letters, 2017. **17**(5): p. 2945-2952.

50. Frizyuk, K., et al., *Enhancement of Raman scattering in dielectric nanostructures with electric and magnetic Mie resonances.* Physical Review B, 2018. **97**(8): p. 085414.

51. Zograf, G.P., et al., *Stimulated Raman scattering from Mie-resonant subwavelength nanoparticles.* Nano Letters, 2020. **20**(8): p. 5786-5791.

52. Zograf, G.P., et al., *Local crystallization of a resonant amorphous silicon nanoparticle for the implementation of optical nanothermometry.* JETP Letters, 2018. **107**: p. 699-704.

53. Abel, M.R. and S. Graham. *Thermometry of polycrystalline silicon structures using Raman Spectroscopy*. in *International Electronic Packaging Technical Conference and Exhibition*. 2005.

54. Marcins, G., et al. *Crystallization processes of amorphous Si by thermal annealing and pulsed laser processing*. in *IOP Conference Series: Materials Science and Engineering*. 2011. IOP Publishing.

55. Karpinski, P., et al., *Optical rotation and thermometry of laser tweezed silicon nanorods.* Nano Letters, 2020. **20**(9): p. 6494-6501.

56. Danesi, S., et al., *Photo-induced heat generation in non-plasmonic nanoantennas.* Physical Chemistry Chemical Physics, 2018. **20**(22): p. 15307-15315.
57. Tian, J., et al., *Near-infrared super-absorbing all-dielectric metasurface based on single-layer germanium nanostructures.* Laser & Photonics Reviews, 2018. **12**(9): p. 1800076.
58. Li, Y., et al., *Optical nanoheating of resonant silicon nanoparticles.* Optics Express, 2019. **27**(21): p. 30971-30978.
59. Zograf, G.P., et al., *All-dielectric thermonanophotonics.* Advances in Optics and Photonics, 2021. **13**(3): p. 643-702.
60. Milichko, V.A., et al., *Metal-dielectric nanocavity for real-time tracing molecular events with temperature feedback.* Laser & Photonics Reviews, 2018. **12**(1): p. 1700227.
61. Zograf, G.P., et al., *All-optical nanoscale heating and thermometry with resonant dielectric nanoparticles for controllable drug release in living cells.* Laser & Photonics Reviews, 2020. **14**(3): p. 1900082.
62. Archetti, A., et al., *Thermally reconfigurable metalens.* Nanophotonics, 2022. **11**(17): p. 3969-3980.
63. Hong, I., et al., *Hybrid Optical and Diffusiophoretic Nanomanipulation Using All-Dielectric Anapole-Enhanced Thermonanophotonics.* ACS Photonics, 2023. **10**(11): p. 4038-4044.
64. Vismara, R., et al., *Solar harvesting based on perfect absorbing all-dielectric nanoresonators on a mirror.* Optics express, 2019. **27**(16): p. A967-A980.
65. Yang, S. and J.C. Ndukaife, *Optofluidic transport and assembly of nanoparticles using an all-dielectric quasi-BIC metasurface.* Light: Science & Applications, 2023. **12**(1): p. 188.
66. Eyring, G. and M. Fayer, *Laser-induced phenomena at liquid-glass interfaces: Particle deposition and holographic bubble grating formation.* Journal of applied physics, 1984. **55**(11): p. 4072-4080.
67. Yavas, O., et al., *Optical and acoustic study of nucleation and growth of bubbles at a liquid-solid interface induced by nanosecond-pulsed-laser heating.* Applied Physics A, 1994. **58**: p. 407-415.
68. Liu, X., et al., *Formation and dissolution of microbubbles on highly-ordered plasmonic nanopillar arrays.* Sci Rep, 2015. **5**: p. 18515.

69. Li, F., et al., *Oscillate boiling from microheaters.* Physical Review Fluids, 2017. **2**(1): p. 014007.
70. Wang, Y., et al., *Vapor and gas-bubble growth dynamics around laser-irradiated, water-immersed plasmonic nanoparticles.* ACS nano, 2017. **11**(2): p. 2045-2051.
71. Wang, Y., et al., *Giant and explosive plasmonic bubbles by delayed nucleation.* Proceedings of the National Academy of Sciences, 2018. **115**(30): p. 7676-7681.
72. Li, X., et al., *Plasmonic bubble nucleation and growth in water: Effect of dissolved air.* The Journal of Physical Chemistry C, 2019. **123**(38): p. 23586-23593.
73. Zaytsev, M.E., et al., *Gas–vapor interplay in plasmonic bubble shrinkage.* The Journal of Physical Chemistry C, 2020. **124**(10): p. 5861-5869.
74. Hou, L., et al., *Explosive formation and dynamics of vapor nanobubbles around a continuously heated gold nanosphere.* New Journal of Physics, 2015. **17**(1): p. 013050.
75. Namura, K., et al., *Round-trip motion of air-rich bubbles exhaled from a vapor-rich bubble generated at a local heating point.* Journal of Applied Physics, 2024. **135**(21).
76. Namura, K., et al., *Self-Oscillation of Locally Heated Water Vapor Microbubbles in Degassed Water.* Advanced Materials Interfaces, 2020. **7**(18): p. 2000483.
77. Hiroshige, N., et al., *Microbubble oscillation on localized heat source affected by dissolved gases in water.* Journal of Applied Physics, 2024. **135**(9).
78. Hahne, E., *Heat Transfer in Boiling*. 1977, Hemisphere.
79. Marangoni, C., *On the expansion of a drop of liquid floating on the surface of another liquid.* Tipographia dei fratelli Fusi, Pavia, 1865.
80. Marangoni, C., *The principle of the surface viscosity of liquids established by mr. j. plateau.* Il Nuovo Cimento, 1972. **5**: p. 239-273.
81. Thomson, J., *XLII. On certain curious motions observable at the surfaces of wine and other alcoholic liquors.* The London, Edinburgh, and Dublin Philosophical Magazine and Journal of Science, 1855. **10**(67): p. 330-333.
82. Nakata, S. and K. Matsuo, *Characteristic self-motion of a camphor boat sensitive to ester vapor.* Langmuir, 2005. **21**(3): p. 982-984.
83. Dai, Q., et al., *Directional interfacial motion of liquids: Fundamentals, evaluations, and manipulation strategies.* Tribology International, 2021. **154**: p. 106749.
84. Baroud, C.N., *Thermocapillarity*, in *Encyclopedia of Microfluidics and Nanofluidics*, D. Li, Editor. 2013, Springer US: Boston, MA. p. 1-7.
85. Ahmadi, S.F., et al., *How soap bubbles freeze.* Nature communications, 2019. **10**(1): p. 2531.

86. McGrew, J.L., F.L. Bamford, and T.R. Rehm, *Marangoni flow: an additional mechanism in boiling heat transfer.* Science, 1966. **153**(3740): p. 1106-1107.

87. Beer, H., *Beitrag zur Wärmeübertragung beim Sieden*. Vol. 2. 1969: Pergamon Press.

88. Rastopov, S.F. and A.T.e. Sukhodol'skiĭ, *Use of the laser-induced Marangoni effect for recording of diffraction gratings.* Soviet Journal of Quantum Electronics, 1987. **17**(8): p. 1091.

89. Ivanova, N. and B. Bezuglyi, *Thermocapillary vortices induced by a light beam near a bubble surface in a Hele-Shaw cell.* Journal of applied mechanics and technical physics, 2005. **46**: p. 691-696.

90. Muruganathan, R., Y. Zhang, and T.M. Fischer, *Interfacial thermocapillary vortical flow for microfluidic mixing.* Journal of the American Chemical Society, 2006. **128**(11): p. 3474-3475.

91. Berry, D., N. Heckenberg, and H. Rubinszteindunlop, *Effects associated with bubble formation in optical trapping.* Journal of Modern Optics, 2000. **47**(9): p. 1575-1585.

92. Setoura, K., S. Ito, and H. Miyasaka, *Stationary bubble formation and Marangoni convection induced by CW laser heating of a single gold nanoparticle.* Nanoscale, 2017. **9**(2): p. 719-730.

93. Namura, K., et al., *Sheathless particle focusing in a microfluidic chamber by using the thermoplasmonic Marangoni effect.* Applied Physics Letters, 2016. **108**(7).

94. Namura, K., K. Nakajima, and M. Suzuki, *Quasi-stokeslet induced by thermoplasmonic Marangoni effect around a water vapor microbubble.* Scientific Reports, 2017. **7**(1): p. 45776.

95. Namura, K., K. Nakajima, and M. Suzuki, *Investigation of transition from thermal- to solutal-Marangoni flow in dilute alcohol/water mixtures using nano-plasmonic heaters.* Nanotechnology, 2018. **29**(6): p. 065201.

96. Namura, K., et al., *Self-Oscillation of Locally Heated Water Vapor Microbubbles in Degassed Water.* Advanced Materials Interfaces, 2020. **7**(18): p. 2000483.

97. Namura, K., et al., *Effects of Marangoni and drag forces on the transition from vapor-rich to air-rich bubbles.* arXiv preprint arXiv:2401.07501, 2024.

98. Namura, K., et al., *Microfluidic control on nanoplasmonic thin films using Marangoni effect.* Journal of Nanophotonics, 2016. **10**(3): p. 033006-033006.

99. Hu, W., K.S. Ishii, and A.T. Ohta, *Micro-assembly using optically controlled bubble microrobots.* Applied Physics Letters, 2011. **99**(9).

100. Namura, K., et al., *Direction control of quasi-stokeslet induced by thermoplasmonic heating of a water vapor microbubble.* Sci Rep, 2019. **9**(1): p. 4770.
101. Namura, K., et al., *Gold Micropetals Self-Assembled by Shadow-Sphere Lithography for Optofluidic Control.* Advanced Materials Interfaces, 2022. **9**(18): p. 2200200.
102. Faraday, M., *X. The Bakerian Lecture.—Experimental relations of gold (and other metals) to light.* Philosophical transactions of the Royal Society of London, 1857(147): p. 145-181.
103. Maier, S.A., et al., *Plasmonics—a route to nanoscale optical devices.* Advanced materials, 2001. **13**(19): p. 1501-1505.
104. Mie, G., *Beiträge zur Optik trüber Medien, speziell kolloidaler Metallösungen.* Annalen der physik, 1908. **330**(3): p. 377-445.
105. Bohren, C.F. and D.R. Huffman, *Absorption and Scattering of Light by Small Particles*. 2008: Wiley.
106. Saleh, B.E.A. and M.C. Teich, *Fundamentals of Photonics*. 2019: Wiley.
107. Hecht, E., *Optics*. 2002: Addison-Wesley.
108. Lorentz, H.A., *The Theory of Electrons and Its Applications to the Phenomena of Light and Radiant Heat*. 2003: Dover Publications.
109. Fox, A.M., *Optical Properties of Solids*. 2001: Oxford University Press.
110. Rakić, A.D., et al., *Optical properties of metallic films for vertical-cavity optoelectronic devices.* Applied optics, 1998. **37**(22): p. 5271-5283.
111. Johnson, P.B. and R.W. Christy, *Optical Constants of the Noble Metals.* Physical Review B, 1972. **6**(12): p. 4370-4379.
112. Young, A.T., *Rayleigh scattering.* Phys. Today, 1982. **35**(1): p. 42-48.
113. Cox, A., A.J. DeWeerd, and J. Linden, *An experiment to measure Mie and Rayleigh total scattering cross sections.* American Journal of Physics, 2002. **70**(6): p. 620-625.
114. Maier, S.A., *Plasmonics: Fundamentals and Applications*. 2010: Springer US.
115. Yu, R., L.M. Liz-Marzán, and F.J.G. de Abajo, *Universal analytical modeling of plasmonic nanoparticles.* Chemical Society Reviews, 2017. **46**(22): p. 6710-6724.
116. Korotun, A.V. and N.I. Pavlyshche, *Cross Sections for Absorption and Scattering of Electromagnetic Radiation by Ensembles of Metal Nanoparticles of Different Shapes.* Physics of Metals and Metallography, 2021. **122**(10): p. 941-949.
117. Kats, M.A., et al., *Effect of radiation damping on the spectral response of plasmonic components.* Optics express, 2011. **19**(22): p. 21748-21753.

118. Todisco, F., et al., *Magnetic and electric Mie-exciton polaritons in silicon nanodisks.* Nanophotonics, 2020. **9**(4): p. 803-814.
119. Evlyukhin, A.B., et al., *Optical response features of Si-nanoparticle arrays.* Physical Review B—Condensed Matter and Materials Physics, 2010. **82**(4): p. 045404.
120. García-Etxarri, A., et al., *Strong magnetic response of submicron silicon particles in the infrared.* Optics express, 2011. **19**(6): p. 4815-4826.
121. Schinke, C., et al., *Uncertainty analysis for the coefficient of band-to-band absorption of crystalline silicon.* Aip Advances, 2015. **5**(6).
122. Pierce, D.T. and W.E. Spicer, *Electronic structure of amorphous Si from photoemission and optical studies.* Physical Review B, 1972. **5**(8): p. 3017.
123. Aćimović, S.S., et al., *Antibody–antigen interaction dynamics revealed by analysis of single-molecule equilibrium fluctuations on individual plasmonic nanoparticle biosensors.* ACS nano, 2018. **12**(10): p. 9958-9965.
124. Landau, L.D. and E.M. Lifshitz, *CHAPTER V - THERMAL CONDUCTION IN FLUIDS*, in *Fluid Mechanics (Second Edition)*, L.D. Landau and E.M. Lifshitz, Editors. 1987, Pergamon. p. 192-226.
125. Landau, L.D. and E.M. Lifshitz, *CHAPTER VI - DIFFUSION*, in *Fluid Mechanics (Second Edition)*, L.D. Landau and E.M. Lifshitz, Editors. 1987, Pergamon. p. 227-237.
126. Cengel, Y. and T.M. Heat, *A practical approach.* Heat and Mass Transfer, 2003.
127. Herman, C. *Experimental investigation of pool boiling heat transfer enhancement in microgravity in the presence of electric fields*. in *Third Microgravity Fluid Physics Conference*. 1996.
128. Pavlenko, A. and H. Koshlak, *Study of the Dynamics of a Single Bubble.* Energies, 2024. **17**(17): p. 4236.
129. Chaplin, M.F., *Structure and properties of water in its various states.* Encyclopedia of water: science, technology, and society, 2019: p. 1-19.
130. Prosperetti, A., *Vapor bubbles.* Annual review of fluid mechanics, 2017. **49**(1): p. 221-248.
131. Xiao, L., et al., *A review of pool-boiling processes based on bubble-dynamics parameters.* Applied Sciences, 2023. **13**(21): p. 12026.
132. Murshed, S.M.S., et al., *A review of boiling and convective heat transfer with nanofluids.* Renewable and Sustainable Energy Reviews, 2011. **15**(5): p. 2342-2354.
133. Kandlikar, S.G., *Heat transfer mechanisms during flow boiling in microchannels.* J. Heat Transfer, 2004. **126**(1): p. 8-16.

134. Taylor, R.A. and P.E. Phelan, *Pool boiling of nanofluids: Comprehensive review of existing data and limited new data.* International Journal of Heat and Mass Transfer, 2009. **52**(23): p. 5339-5347.

135. Hu, H., et al., *Boiling and quenching heat transfer advancement by nanoscale surface modification.* Scientific reports, 2017. **7**(1): p. 6117.

136. Vakarelski, I.U., et al., *Stabilization of Leidenfrost vapour layer by textured superhydrophobic surfaces.* Nature, 2012. **489**(7415): p. 274-277.

137. Chung, J., T. Chen, and S. Maroo, *A review of recent progress on nano/micro scale nucleate boiling fundamentals.* 2011.

138. Chen, T. and J.N. Chung, *An experimental study of miniature-scale pool boiling.* J. Heat Transfer, 2003. **125**(6): p. 1074-1086.

139. Kim, D.E., et al., *Review of boiling heat transfer enhancement on micro/nanostructured surfaces.* Experimental Thermal and Fluid Science, 2015. **66**: p. 173-196.

140. Mahmoud, M. and T. Karayiannis, *Pool boiling review: Part I–Fundamentals of boiling and relation to surface design.* Thermal Science and Engineering Progress, 2021. **25**: p. 101024.

141. Jollans, T. and M. Orrit, *Explosive, oscillatory, and Leidenfrost boiling at the nanoscale.* Physical Review E, 2019. **99**(6): p. 063110.

142. Wang, Y., et al., *Giant and explosive plasmonic bubbles by delayed nucleation.* Proceedings of the National Academy of Sciences, 2018. **115**(30): p. 7676-7681.

143. Lombard, J., T. Biben, and S. Merabia, *Nanobubbles around plasmonic nanoparticles: Thermodynamic analysis.* Physical Review E, 2015. **91**(4): p. 043007.

144. Deguchi, S., et al., *Direct measurement of force exerted during single microbubble generation.* Applied Physics Letters, 2013. **102**(8).

145. Kuhlmann, H.C. *Thermocapillary Convection*. in *Free Surface Flows*. 1998. Vienna: Springer Vienna.

146. Fyrillas, M.M. and A.J. Szeri, *Dissolution or growth of soluble spherical oscillating bubbles.* Journal of Fluid Mechanics, 1994. **277**: p. 381-407.

147. Marmottant, P. and S. Hilgenfeldt, *Controlled vesicle deformation and lysis by single oscillating bubbles.* Nature, 2003. **423**(6936): p. 153-156.

148. Manasseh, R., *Acoustic bubbles, acoustic streaming, and cavitation microstreaming.* Handbook of ultrasonics and sonochemistry, 2016. **33**.

149. Ljunggren, S. and J.C. Eriksson, *The lifetime of a colloid-sized gas bubble in water and the cause of the hydrophobic attraction.* Colloids and Surfaces A: Physicochemical and Engineering Aspects, 1997. **129**: p. 151-155.

150. Wang, F., et al., *Plasmonic Bubbles: From Fundamentals to Applications.* Advanced Functional Materials, 2024: p. 2403606.

151. Ortega-Mendoza, J., et al., *Marangoni force-driven manipulation of photothermally-induced microbubbles.* Optics Express, 2018. **26**(6): p. 6653-6662.

152. Sarabia-Alonso, J., et al., *3D trapping of microbubbles by the Marangoni force.* Optics Letters, 2021. **46**(23): p. 5786-5789.

153. Jasper, J.J., *The surface tension of pure liquid compounds.* Journal of physical and chemical reference data, 1972. **1**(4): p. 841-1010.

154. Miniewicz, A., et al., *Optothermal Marangoni Effect: Phenomena and Applications*, in *Novel Optical Materials*. 2024, World Scientific. p. 31-70.

155. Vargaftik, N., B. Volkov, and L. Voljak, *International tables of the surface tension of water.* Journal of Physical and Chemical Reference Data, 1983. **12**(3): p. 817-820.

156. Karbalaei, A., R. Kumar, and H.J. Cho, *Thermocapillarity in microfluidics—A review.* Micromachines, 2016. **7**(1): p. 13.

157. Piazza, R., *Thermophoresis: moving particles with thermal gradients.* Soft Matter, 2008. **4**(9): p. 1740-1744.

158. Reichl, M., et al., *Why Charged Molecules Move Across a Temperature Gradient: The Role of Electric Fields.* Physical Review Letters, 2014. **112**(19): p. 198101.

159. Fayolle, S., T. Bickel, and A. Würger, *Thermophoresis of charged colloidal particles.* Physical Review E, 2008. **77**(4): p. 041404.

160. Würger, A., *Thermal non-equilibrium transport in colloids.* Reports on Progress in Physics, 2010. **73**(12): p. 126601.

161. Braun, M., et al., *Single molecules trapped by dynamic inhomogeneous temperature fields.* Nano letters, 2015. **15**(8): p. 5499-5505.

162. Duhr, S. and D. Braun, *Thermophoretic depletion follows Boltzmann distribution.* Physical review letters, 2006. **96**(16): p. 168301.

163. Putnam, S.A. and D.G. Cahill, *Transport of nanoscale latex spheres in a temperature gradient.* Langmuir, 2005. **21**(12): p. 5317-5323.

164. Maragò, O., P. Jones, and G. Volpe, *Optical Tweezers: Principles and Applications*. 2015, Cambridge University Press, New York.

165. Ashkin, A., *Acceleration and trapping of particles by radiation pressure.* Physical review letters, 1970. **24**(4): p. 156.

166. Ashkin, A. and J. Dziedzic, *Optical levitation by radiation pressure.* Applied Physics Letters, 1971. **19**(8): p. 283-285.

167. Požar, T., et al., *Isolated detection of elastic waves driven by the momentum of light.* Nature Communications, 2018. **9**(1): p. 3340.

168. Kerker, M., *The scattering of light and other electromagnetic radiation: physical chemistry: a series of monographs*. Vol. 16. 2013: Academic press.

169. Harada, Y. and T. Asakura, *Radiation forces on a dielectric sphere in the Rayleigh scattering regime.* Optics communications, 1996. **124**(5-6): p. 529-541.

170. Ulanowski, Z. *Optical tweezers-principles and applications*. in *Proc. Roy. Microsc. Soc*. 2001.

171. Gordon, J.P., *Radiation forces and momenta in dielectric media.* Physical Review A, 1973. **8**(1): p. 14.

172. Griffiths, D.J., *Introduction to electrodynamics*. 2023: Cambridge University Press.

173. Sharma, P., S. Ghosh, and S. Bhattacharya, *A high-precision study of hindered diffusion near a wall.* Applied Physics Letters, 2010. **97**(10).

174. Brenner, H., *The slow motion of a sphere through a viscous fluid towards a plane surface.* Chemical engineering science, 1961. **16**(3-4): p. 242-251.

175. Liu, L., et al., *Absolute position total internal reflection microscopy with an optical tweezer.* Proceedings of the National Academy of Sciences, 2014. **111**(52): p. E5609-E5615.

176. Blake, J.R., *A note on the image system for a stokeslet in a no-slip boundary.* Mathematical Proceedings of the Cambridge Philosophical Society, 1971. **70**(2): p. 303-310.

177. Blake, J.R. and A.T. Chwang, *Fundamental singularities of viscous flow.* Journal of Engineering Mathematics, 1974. **8**(1): p. 23-29.

178. Dara, P., et al., *Directional control of transient flows generated by thermoplasmonic bubble nucleation.* The Journal of Physical Chemistry C, 2023. **127**(35): p. 17454-17459.